Universität Rostock

Traditio et Innovatio

Studies on Pulsed Wire Discharges

Experimental and Numerical Investigations on Exploding X5CrNi18-10 Wires

Master Thesis

UNIVERSITY OF ROSTOCK

Faculty of Computer Science and Electrical Engineering
Institute of High Voltage and High Current Technology

Maximilian Felix Bigelmayr
Matrikel-Nr.: 216206098
Rostock, 24 June 2019

Supervised by
Prof. Dr. rer. nat. Dirk Uhrlandt
N. Dipl. B.Tech. Petrus J. Pieterse

Abstract

The objective of this thesis is the analysis of pulsed capacitor discharges through X5CrNi18-10 steel wires with varying geometries. Discharges at high energy density levels produce pressure waves which have numerous application possibilities in industry. Experimental trials are performed using a series RLC configuration (C=150 µF, L=4,36 µH, U=6 kV), with the wire producing the circuit damping. In an effort to predict the optimum wire and circuit dimensioning for maximum energy transfer efficiency, various experiments are performed. Wire lengths ranging from 20 mm–160 mm and wire diameters from 0,6 mm–0,8 mm are used. The pulse current and voltage across the wire is measured for each separate wire configuration. This allows the computation of the absorbed energy within each individual wire resp. wire-plasma as well as the power. An analysis of the electrical resistance behavior of these wire-plasmas are performed to find the time independent Specific Resistance Characteristic for various wires. A time independent fit function is used to relate the specific resistance to the wire energy density.

It was possible to discover a coupled system of ordinary differential equations (ODEs), using a semi-physical model, which in turn allows the computation of the pulse current during discharges. The known circuit parameters as well as the time independent resistance is used to numerically solve the differential equation system through the implementation of an adaptive Runge-Kutta method.

This new model may help to plan, design and construct experimental and industrial pulsed wire discharge systems. By using these methods, one is capable of predicting the current, the wire voltage, the capacitor voltage, as well as the energy distribution and efficiency for pulsed steel wire discharge systems using known circuit parameters.

Table of Contents

List of Symbols

Time, Frequency, Charges and Currents

Symbol	Unit	Description
t	s	time
t_{bend}	s	point in time where E_w shows a bend
T	s	period
δ	1/s	damping coefficient
ω_0	rad/s	angular frequency
Q	C	charge
I	A	current
s	A/s	time derivation of the current
j	A/ m^2	current density
I_{od}	A	current in overdamped RLC circuit
I_{cd}	A	current in critically damped RLC circuit
I_{ud}	A	current in underdamped RLC circuit
$I_{\max(cd)}$	A	max. current in a critically damped RLC circuit

Voltages

Symbol	Unit	Description
U	V	voltage
U_C	V	capacitor voltage
U_{C0}	V	initial capacitor voltage (t=0)
U_L	V	inductance voltage
U_R	V	voltage across resistor
U_{Rcir}	V	voltage across circuit resistor
U_w	V	voltage across the wire
U_{clamp}	V	clamp voltage

Resistors and Resistivity

Symbol	Unit	Description
R	Ω	resistance
R_w	Ω	resistance of wire resp. wire plasma
$\bar{R}_w$	Ω	time averaged resistance of wire resp. wire plasma
R_{cd}	Ω	resistance needed for critical damping behaviour
R_{cir}	Ω	circuit resistance (without wire)
$\bar{R}_{cir}$	Ω	time averaged circuit resistance (without wire)
$\bar{R}_{sg}$	Ω	time averaged spark gap resistance
ρ	Ωm	specific resistance
ρ_w	Ωm	specific resistance of wire resp. wire plasma

Power, Energies and Action

Symbol	Unit	Description
P	W	power
P_w	W	power in wire resp. wire plasma
E	J	energy
E_C	J	energy in capacitor
E_{sum}	J	total energy in circuit
E_{C0}	J	initially stored energy in capacitor (t=0)
E_R	J	energy absorbed in resistor
E_L	J	energy in magnetic field of circuit inductance
E_w	J	energy absorbed in wire resp. wire plasma
$E_{w\infty}$	J	final absorbed energy within the wire
E_{pp}	J	energy plasma pulse
E_{hp}	J	energy heat pulse
E_{Rod}	J	energy absorbed in resistor (overdamped RLC circuit)
E_{Rcd}	J	energy absorbed in resistor (critically damped RLC circuit)
E_{Rud}	J	energy absorbed in in resistor (underdamped RLC circuit)
E_{C0}	J	initially stored energy in capacitor (*t*=0)
$E_{Rud\infty}$	J	final energy absorbed in underdamped RLC circuit
E_{cir}	J	lost energy in circuit
A	A^2s	action integral value of total circuit
A_∞	A^2s	final action integral value of total circuit

Thermodynamics

Symbol	Unit	Description
ΔH	J	thermal enthalpy
C_p	J/(gK)	specific heat capacity at constant pressure
T	K	temperature
T_s	K	solidus temperature
T_l	K	liquidus temperature
ΔH_f	J	enthalpy or latent heat of melting
C_{pL}	J/(gK)	specific heat capacity (liquid phase)
Y_i	1	atomic fractions of the alloy elements
T_b	K	boiling temperature
ΔH_{vap}	J/g	vaporisation enthalpy
ΔH_{sub}	J/g or J/ m^3	sublimation enthalpy
W_{sub}	J	sublimation energy

Wire dimensions

Symbol	Unit	Description
l	m	wire length
d	m	wire diameter
r	m	wire radius
S	m^2	wire cross section
V	m^3	wire volume
V,i	m^3	initial wire volume

Symbols related to wire dimensions

Symbol	Unit	Description
$e_{V,i}$	J/m^3	energy density in wire resp. wire plasma related to initial volume V,i
a_{Ri}	A^{2}s/m^4	specific action of resistive element
a_w	A^{2}s/m^4	specific action of wire

Miscellaneous symbols

Symbol	Unit	Description
L	H	inductance
L_{clamp}	H	clamp inductance (between Ⓑ and Ⓔ in Fig. 3.4, Fig. 3.7)
C	F	capacitance
t_v	s	the time required to vaporize the wire
ψ	s	time constant of instabilities
ζ	s	electrothermal time constant
$\mathcal{E}_w$	V/m	electric field strength in wire reps. wire plasma
k	ΩC/cm	spark constant
F	cm	spark gap distance
B	T	magnetic flux density
e_m	J/m^3	magnetic energy density
p_m	N/m^2	magnetic pressure
η	1	efficiency of experiment

Symbols related to simulations

Symbol	Unit	Description
I_{sim}	A	simulated current
U_{Wsim}	V	simulated wire voltage
E_{total}	J	simulated total system energy
ΔE_{sim}	J	difference of total system energy (E_{total}) and initial energy (E_{C0})
h	s	step rate
ρ_{w0}	Ωm	initial value of specific resistance of wire resp. wire plasma
m	Ωm^4/J	slope factor of linear equation representing the resistivity

Abbreviations

Acronym	Description
ODEs	ordinary differential equations
MHD	magnetohydrodynamics
WKB	mathematical method named after Wentzel, Kramers, Brillouin

In this thesis a comma (,) is used as decimal separator.

1. Introduction and Motivation

Pulsed wire discharge (PWD) experiments, also referred to as the *exploding wire phenomenon* (EWP), have a long tradition in different disciplines since the invention of the Leyden jar in 1745. Edward Nairne first discharged capacitors through metal wires [1], which resulted in a rapid vaporisation of the metal, combined with the creation of a shock wave. Despite the slow heating process which was well known from low voltages that caused wires to glow, a high voltage discharge through a metal wire is characterised by a rise in high current dI/dt, which not only allows the wire to melt but also vaporises the metal [2]. Before the first invention of storage oscilloscopes in 1946 by the US company Tektronix, it was impossible to measure the electrical discharge behavior of capacitors through metal wires. In the 1960's and 1970's many scientists performed pulsed wire discharge experiments in order to do research in plasma physics, high speed forming of sheet metals through *Hydrosparc Forming* as well as other technological processes [3].

In April 1959, the Air Force Cambridge Research Center in Boston organized the first international conference on the exploding wire phenomenon [4]. Researchers from all over the world presented their investigations to get a better understanding of the very complex physical mechanisms. In 1961 a second conference [5] was organized.

In 1965 Frank Früngel published the book "High Speed Pulse Technology" [6] in which he describes the different methods of measurement and diagnosis as for example through X-Ray photography, in order to analyse the interesting phenomena of pulsed wire discharges. Since those days the typical time segments which occur during the phenomena are well known. However even today they are not fully understood.

In the past high expectations were placed on the application of shockwave creation by exploding wires, but in practical use such setups e.g. for *sheet metal forming* appeared to be too large and bulky [7]. Nevertheless, the technology behind high voltage capacitors has improved considerably within the last decades. New foil as well as dielectric materials offer us now the ability to produce high energy density capacitors of up to 3,0 J/cm^3 [8]. This technical advancement, from an economic standpoint, could pave the way in regards to the use of capacitor driven applications in combination with exploding wires, in order to produce shockwaves. Since the efficiency of diverse setups concerning *underwater electrical wire explosions* (*UEWE*s) depends on many different parameters, e.g. the capacitor voltage, circuit inductance, wire material and dimensions, a detailed understanding of the dependencies and mechanisms involved is essential.

The main goal of this thesis is a fundamental analysis of exploding wire experiments with a chromium-nickel alloy (X5CrNi18-10). Instead of using pure metals (e.g. Cu, Ag, Au, Pt, Al, Fe, W), as in nearly all experiments were conducted so far, the use of X5CrNi18-10 offers many advantages in regard to its ideal resistance R_{cd}, which is needed in order to reach a critical damping behaviour (compare 4.1.1). By using modern measurement technology, combined with contemporary data analysis methods, electrodynamic behavior of exploding steel wires in the time range between 0-250 μs was investigated in this thesis. Particular focus was given on analysing the influence of initial capacitor voltage, wire diameter and wire length regarding the energy absorbed in the wire as well as the efficiency.

The knowledge gained about the circuit parameters (C=150 μF, U_{C0}=6,00 kV, L=4,36 μH) should help to improve further investigations to construct experimental and commercial applications which allow to perform *sheet metal forming* and *explosive welding* etc.
Furthermore, special emphasis was given to a detailed analysis of the resistance characteristics of each individual experimental setting. These characteristics may be used for a model setup and simulations of arbitrary exploding wire experiments. Therefore, a special theoretical model was built. The investigated semiphysical model is based on several assumptions. However the derivated system of ordinary differential equations (ODE) could be implemented in a self-written software tool within Labview. By using this software tool, experimenters may analyse their pulsed wire discharge experiments in detail regarding all main quantities (capacitor voltage, wire voltage, absorbed energy in wire etc.).

This is a brief overview of the thesis' structure:

Chapter 2
At first, the reader will be informed about the basic theoretical principles of the exploding wire phenomenon. Different discharge types are discussed, as well as the classification model of exploding wires according to the Chace and Levine scheme. Since the energy transformation during wire explosions is quite similar to the discharge behavior of *RLC* circuits, special emphasis was also given to the theory behind the energy absorption and critical damping of *RLC* circuits. As the description of an *RLC* circuit with variable resistance *R(t)* is introduced just in brief, it will be investigated in detail in chapter 5.

Chapter 3
The main aspects of the experimental setup will be explained in this chapter. A short presentation of the capacitor bank, clamp device and measurement equipment will help the reader to understand the underlying experimental setup, which was used to collect the experimental data. By drawing a detailed circuit diagram of the experimental setup, the discharge behavior with constant load resistance could be analysed by using PSpice. The simulations confirm that it is a profound assumption to use an *RLC* circuit as a suitable circuit diagram to describe the experimental setup.

Chapter 4
In the experimental part of this thesis, the thermodynamical properties of the used wire material is discussed first. By explaining the experimental procedure and data analysis the reader should get an impression of the conduction of the experiments and the data processing. As a first experimental result the accuracy and repeatability will be presented.
In the following sections the results of the experiments are reasoned. The effect of different charging voltage (4,42 kV- 6,00 kV) will be discussed as well as the effect of variations in wire length (20-180 mm) and diameter (600-800 μm).

For all investigated wire parameters special emphasis was given to a detailed analysis of the resistance characteristics. Finally both action integral and absorbed wire energy will be discussed along with the involved averaged wire resistance and circuit efficiency.

Chapter 5
In this chapter the concept of a time independent resistance characteristic in relation to the energy density within the wire will be used to derive a system of *ordinary differential equations* (*ODEs*). By using eligible assumptions, the model could be implemented in a self-built software with graphical user interface in Labview. The functionality of the software tool could be verified by comparing the simulation results with experimental findings. The simulation results of a particular wire experiment (d=700 μm, l=120 mm) will be discussed in detail.

2. The theory behind pulsed wire discharges

2.1 Types of discharge behavior

After charging a capacitor bank up to a predefined high voltage, the capacitor network is discharged through a metal wire via a so-called Switching Spark Gap (SSG), ignitron or thyratron [6]. Depending on the size, the capacitor bank usually contains several high voltage capacitors, which are connected to one another in parallel or series. However, this setup can be simplified to contain a capacitance C, a switch, a circuit inductance L, a fixed circuit resistance R_{cir} and a time dependent wire resistance R_w (Figure 2.1). Depending on the discharge parameters (capacitance, voltage, inductance, wire material and dimensions) one is able to distinguish four different types of current curves $I(t)$, which are shown in Figure 2.2.

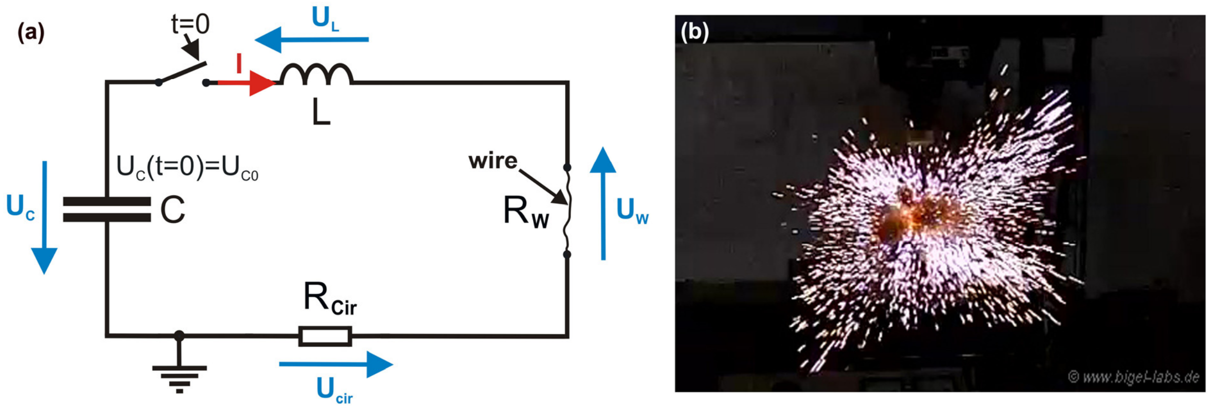

Figure 2.1: (a) schematic setup of pulsed wire discharge experiments: A high voltage capacitor C is charged up to a certain voltage and discharged afterwards through a thin metal wire with a resistance $R_w(t)$. Due to the high current density the metal wire melts and vaporizes violently within a few microseconds. **(b) High speed photograph of an exploding wire** (personally taken photograph)

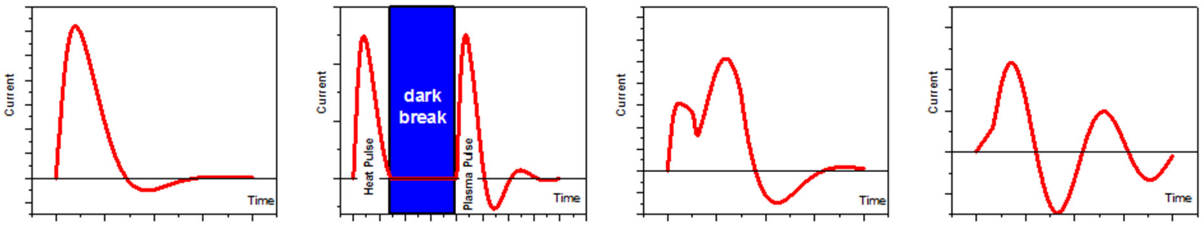

a) Single Heat-Pulse b) Heat-Pulse, Break, Plasma-Pulse c) Heat-Plasma-Pulse d) Direct Plasma-Pulse

Figure 2.2: Different types of discharge current behaviour during pulsed wire discharges (qualitative presentation)

When a High Voltage Capacitor is discharged through a wire with large mass, the capacitors energy may not be adequate to vaporise the metal [5]. In this case the discharge curve is characterised by only a single pulse with one individual peak of current (Figure 2.2 a).
Depending on the capacitors energy and the given wire dimensions a second pulse of current (Figure 2.2 b) is able to occur after a so-called *Dark Break* [9]. Following the first heat pulse the resistance of the wire increases due to its temperature dependency. When the thermodynamic circumstances allow the appearance of boiling nuclei a second plasma pulse occurs, which surrounds the wire in the shape of a cylindric coat. In general, these secondary discharges oscillate due to the low resistance of the gas plasma from the metal vapor [4], [6].
It is common that during experiments with thin wires (especially when the stored energy within the capacitor is larger than the wires enthalpy of vaporisation), the heat pulse and plasma pulse "melt together" with no Dark Break in between the two (Figure 2.2 c) [4].
By using very thin or short wires the heat pulse (Figure 2.2 a) is not visible anymore within the graph (Figure 2.2 d). In this case, solely a direct discharge plasma occurs as a current of damped oscillation [4].

Besides this basic distinction, exploding wires may be further classified according to the “Chace and Levine scheme”, [10] where four classes of “exploding wires” are proposed:

Melting

In this case the available energy is insufficient for complete vaporisation. Thus,

$$\frac{1}{2}CU_{C0}^2 < W_{sub} + \int I^2 R_{cir} dt \ , \tag{1.1}$$

where C is the capacitance of the storage capacitor, U_{C0} is the initial capacitor voltage, W_{sub} is the energy required to sublimate the wire, I is the current through the wire, and R_{cir} is the effective resistance circuit of the discharge circuit.
The wire here never vaporizes, but breaks up into droplets, or simply burns through. This is fuse behavior. Such wire explosions were observed in a more recent publication [11], where the restrike conditions between the droplets were investigated.

Slow explosion

The time required to vaporize the wire is long compared with the time required for instabilities to develop in the melted wire. Thus,

$$t_v >> \Psi \tag{1.2}$$

where t_v is the time required to vaporize the wire, Ψ is the time constant of instabilities, i.e., the time required for instabilities (e.g. unduloids) to double in magnitude. Referred to explosion behavior this means that the explosion occurs slowly enough so that physical distortions have a significant effect on the manner in which the explosion occurs.

Fast Explosion

The time to vaporize is small compared with the time constant of instabilities. Thus,

$$t_v \ll \Psi \ . \tag{1.3}$$

Referred to explosion behavior this means that the explosion occurs so quickly that no significant changes in shape occur.

Explosive Ablation

The time to vaporize is small compared with the electrothermal time constant. Thus,

$$t_v \ll \zeta \tag{1.4}$$

where ζ is the electrothermal time constant, i.e., the time for a temperature equal to the boiling point to penetrate to a depth of r/e, where r is the original wire radius and e is the base of natural logarithms. In terms of explosion behavior the wire vaporizes in a thin surface film before the center has become heated. In other words, the “skin effect” controls the behavior. This type of wire explosion was especially investigated by Ramanova, Ivanenkov et al. in a recent publication [12].

The experiments performed for this thesis can be assigned to the types “Melting” and “Slow explosion”.

2.2 Theory of RLC circuits with constant resistance

2.2.1 Differential equations and solutions to different types of discharge

As aforementioned the curves of current, which occur as a result of capacitors discharging, depend on the dimensions of the used wire. Diverse wire sizes cause different values to emerge concerning the implemented wires initial resistance. In order to better understand pulsed wire discharges and the exploding wire phenomena, it is useful to first of all comprehend the discharge behavior of a capacitor through a constant resistance R as well as a fixed circuit inductance L (*RLC* circuit, Figure 2.3). As the discharge of a charged capacitor through a constant resistance is similar to a circuit with an exploding wire, the examination of *RLC* circuits could help to improve and understand experiments with exploding wires.

The differential equations of a *RLC* circuit can be solved analytically for all three kinds of damp behavior. According to Kirchhoff's second law, the capacitor voltage U_C, inductance voltage U_L and resistor voltage U_R is:

$$U_C(t)+U_L(t)+U_R(t)=0 \tag{2.1}$$

When expressing the occurring voltages through current $I(t)$, capacitance C, circuit inductance L and resistance R one is able to calculate the differential equation for the current:

$$\frac{1}{C}I(t)+L\frac{d^2I(t)}{dI^2}+R\frac{dI(t)}{dt}=0 \tag{2.2}$$

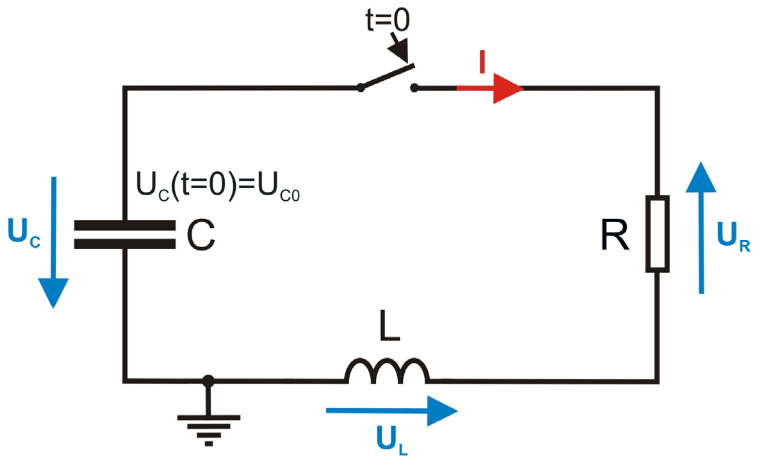

Figure 2.3: Schematic of a RLC circuit

Depending on the implemented resistance R one can distinguish three different types of discharge:

$$I(t)=\begin{cases} I_{od}(t)=\dfrac{U_{C0}}{2L\sqrt{\delta^2-\omega_0^2}}\left(e^{(-\delta+\sqrt{\delta^2-\omega_0^2})t}-e^{(-\delta-\sqrt{\delta^2-\omega_0^2})t}\right) & R>2\sqrt{\dfrac{L}{C}} \quad (a) \\ I_{cd}(t)=\dfrac{U_{C0}}{L}te^{-\delta t} & R=R_{cd}=2\sqrt{\dfrac{L}{C}} \quad (b) \\ I_{ud}(t)=\dfrac{U_{C0}}{L\sqrt{\omega_0^2-\delta^2}}e^{-\delta t}\sin\sqrt{\omega_0^2-\delta^2}\,t & R<2\sqrt{\dfrac{L}{C}} \quad (c) \end{cases} \tag{2.3}$$

The first equation (2.3a) describes an *overdamped circuit*, the second (2.3b) a *critically damped circuit* and the last one an oscillating circuit which is *underdamped* (2.3c). A more detailed deduction of these equations is shown in [13].

The relationship between the *angular frequency* ω_0 and the *damping coefficient* δ can be formulated in the following way:

$$\omega_0^2=\frac{1}{LC} \qquad \Leftrightarrow \qquad \delta=\frac{R}{2L} \tag{2.4}$$

The requirement for *critical damping* (*cd*) is given when

$$\omega_0^2=\delta^2 \qquad \Leftrightarrow \qquad R_{cd}=2\sqrt{\frac{L}{C}} \tag{2.5}$$

counts, which can facilitate the approximation of the ideal average wire resistance. Figure 2.4 shows the discharge behaviour for different resistor values R in a RLC circuit with all other parameters unmodified. Hence, the values for the capacitance (C=150 µF) and inductance (L=4,36 µH) represent exactly the values which describe the experimental setup used within this thesis. When the resistance R is lower than

$$R_{cd}=2\sqrt{\frac{4{,}36\mu H}{150\mu F}}\approx 341m\Omega, \tag{2.6}$$

the current curves show a underdamped oscillation (R=0,25R_{cd}, R=0,5R_{cd} in Figure 2.4 b). The overdamped behaviour takes place when the resistance is larger than R_{cd}. Then the current curves do not show negative peak values (R=2,00R_{cd}, R=3,00R_{cd} in Figure 2.4 b).

2.2.2 The energy absorption within the resistor

Since the amplitude of a shock wave, that is produced by an exploding wire, depends on the speed at which a capacitors energy E_{C0} is converted into heat energy within the given resistor, it is useful to deduce an expression regarding the absorbed energy inside the resistor $E_R(t)$. As the occurring discharge current during an exploding wire experiment is similar to that of an oscillating and a critically damped circuit, the expression $E_R(t)$ of these different situations below, is of particular interest.

Through analytical integration the *energy absorption in the underdamped case* occurs as:

$$E_{Rud}(t)=\int_0^t I_{ud}^2(t)Rdt=$$
$$=RU_{C0}^2e^{-2\delta t}\frac{\delta\sqrt{\omega_0^2-\delta^2}\sin\left(2t\sqrt{\omega_0^2-\delta^2}\right)-\delta^2\cos\left(2t\sqrt{\omega_0^2-\delta^2}\right)+e^{2\delta t}(\delta^2-\omega_0^2)+\omega_0^2}{4\delta L^2\omega_0^2(\delta^2-\omega_0^2)} \tag{2.7}$$

Regarding long periods of time all the stored energy from the capacitor is transformed into heat energy within the resistor:

$$E_{Rud\infty}=\lim_{t\to\infty}\left[E_{Rud}(t)\right]=\frac{RU_{C0}^2(\delta^2-\omega_0^2)}{4\delta L^2\omega^2(\delta^2-\omega_0^2)}=\frac{RU_{C0}^2}{4\delta L^2\omega^2}=\frac{U_{C0}^2C}{2} \tag{2.8}$$

Through curve sketching of the equation (2.3b) one is capable of showing in the critically damped circuit case, that the *maximum discharge current* is as follows:

$$I_{\max(cd)}=\frac{U_{C0}}{L\delta}e^{-1}=\frac{2U_{C0}}{R_{cd}}e^{-1}\approx 0{,}736\frac{U_{C0}}{R_{cd}}=0{,}368U_{C0}\sqrt{\frac{C}{L}} \tag{2.9}$$

The equation below is provided by integration of $I_{cd}^2(t)R$ and represents the *total energy absorbed by the resistor in the case of critical damping*:

$$E_{Rcd}(t)=U_0^2\left\{\frac{1}{2}C-e^{-\frac{2t}{\sqrt{LC}}}\left[\frac{t^2}{L}+\sqrt{\frac{C}{L}}t+\frac{1}{2}C\right]\right\} \tag{2.10}$$

For long durations of time (t→∞) the absorbed energy within the resistor becomes ½CU_{C0}^2, which is the value of the total stored energy inside the capacitor, prior to the discharge pulse.

In general the value $E_{Rcd}(t)$ within a critically damped circuit is s greater compared to $E_R(t)$ in an underdamped or overdamped circuit (Figure 2.4 e). Only for resistance values slightly smaller than R_{cd}, $E_{Rud}(t)$ may become temporary slightly larger than $E_{Rcd}(t)$ (compare E_{Rud} for R=0,5R_{cd}). However, the adaption of R in order to reach a damping behaviour similar to the critical damped circuit should be an important consideration when optimizing exploding wire experiments. Even though the resistance of an exploding wire is not constant, equation (2.10) provides an overview of the velocity of energy stored in a capacitor is capable of being moved into the resistor for any *RLC* circuit.

By utilising the equation (2.3b) in combination with (2.10) the energy transformation process of *RLC* circuits can be calculated in order to receive a rough estimation of how a similar exploding wire discharge could look like. The total energy in an *RLC* circuit contains the energy stored in the capacitor

$$E_C(t)=\frac{1}{2}CU_C^2(t)\ , \qquad (2.11)$$

the inductive energy

$$E_L(t)=\frac{1}{2}LI^2(t) \qquad (2.12)$$

and the energy absorbed in the resistor $E_R(t)$.

Figure 2.4 below shows the discharge current and capacitor voltage for an *RLC* circuit with a capacitance of C=150 µF, capacitor voltage of U_{C0}=6 kV, line inductance of L=4,36 µH and a resistance in the spectrum range of R=[0,25R_{cd}; 3,00R_{cd}]. The energy of the capacitor E_C(t) is shown in Figure 2.4 (c), while the part of the inductive energy is presented in Figure 2.4 (d). On the whole it is convenient to reduce L, this is done in order to attain a faster conversion of the stored capacitor energy into load resistance.

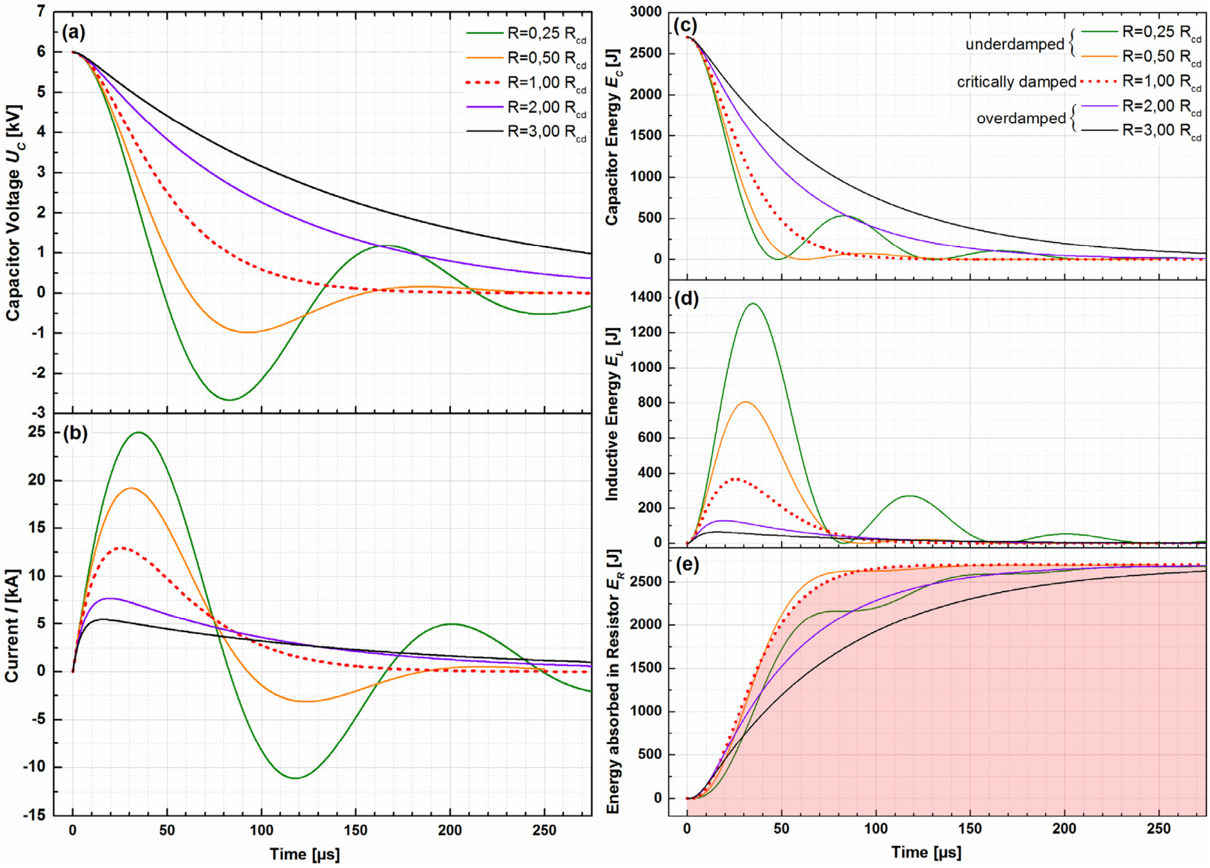

Figure 2.4: Discharge Behavior of a *RLC* circuit (C=150 µF, U_{C0}=6 kV, L=4,36 µH, R=nR_{cd} with n=[0,25; 3,00]). **(a)** capacitor voltage $U_c(t)$, **(b)** discharge current *I(t)* **(c)** capacitor energy $E_c(t)$, **(d)** inductive energy $E_L(t)$, **(e)** energy absorbed in resistor $E_R(t)$. The dotted curves represent the aperiodic damping with R_{cd} ≈341 mΩ.

2.3 Theory of RLC circuits with time dependent resistance

So far the *RLC* circuits viewed above depending on the absorbed energy, had a constant resistor *R* with no alteration of conductance. In practice the wire is vaporised by a capacitor discharge which changes its own resistance R_w during the occurrence of a pulse. Therefore, the variation in regards to the electrical resistivity ρ of a wire, must also be taken into consideration throughout experiments with pulsed wire discharges (Figure 2.5).

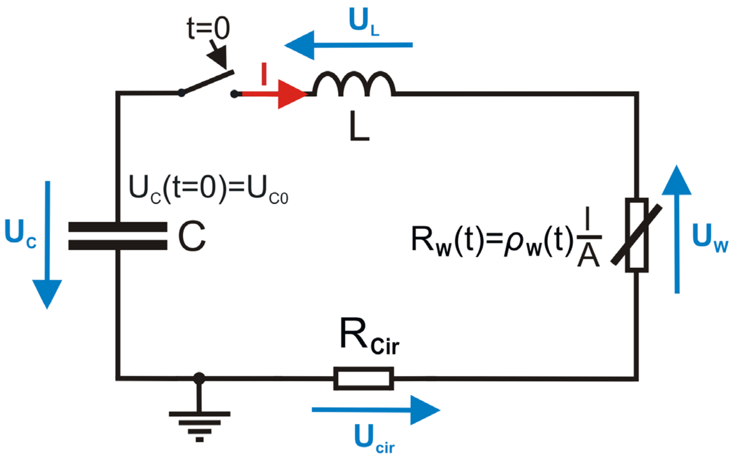

Figure 2.5: Schematic of a *R(t)LC* circuit. The capacitor is discharged through a circuit with a constant inductance *L*, a circuit resistance R_{cir} and a wire with variable resistance $R_w(t)$. The wire resistance $R_w(t)$ is not constant because of dependencies on the wire temperature, plasma instabilities etc.

When assuming a constant circuit resistance R_{cir} and a variable wire resistance $R_w(t)$, Kirchhoff's second law states the following:

$$U_C(t)+U_L(t)+U_{Rcir}(t)+U_W(t)=0 \tag{2.13}$$

Through incorporation of the current and second derivation in respect to time one receives:

$$\frac{1}{C}I(t)+L\frac{d^2I(t)}{dt^2}+\frac{dI(t)}{dt}\left(R_{cir}+R_W(t)\right)+I(t)\frac{dR_W(t)}{dt}=0 \tag{2.14}$$

Subsequent conversion of the equation gives:

$$\frac{d^2I(t)}{dt^2}=-\frac{1}{L}\left(\frac{1}{C}I(t)+\frac{dR_W(t)}{dt}I(t)+\left(R_{cir}+R_W(t)\right)\frac{dI(t)}{dt}\right) \tag{2.15}$$

The time dependent resistance of a wire with the length *l* and cross section *S* can be approximated as follows:

$$R_W(t)=\rho_W(t)\frac{l}{S} \tag{2.16}$$

To solve the differential equation (2.15) together with equation (2.16) the electrical resistivity $\rho_w(t)$ can be expressed as a linearised function, which depends on the absorbed energy density $e_{V,i}(t)$ within the given wire. This approach will be investigated in detail in chapter 5.

3. The experimental setup

3.1 The capacitor bank network and circuit diagram

In order to be able to perform pulsed wire discharge experiments, a capacitor bank network was built (Figure 3.1). The entire setup contains two different types of capacitor bank: a basic capacitor bank (KB1) with a capacitance of C_{KB1}=50 µF and an additional capacitor bank (KB2) with a capacitance of C_{KB2}=100 µF. The networks total capacitance lies at 150 µF and its energy storage is 2700 J, when charged up to 6000 V (Figure 3.2).

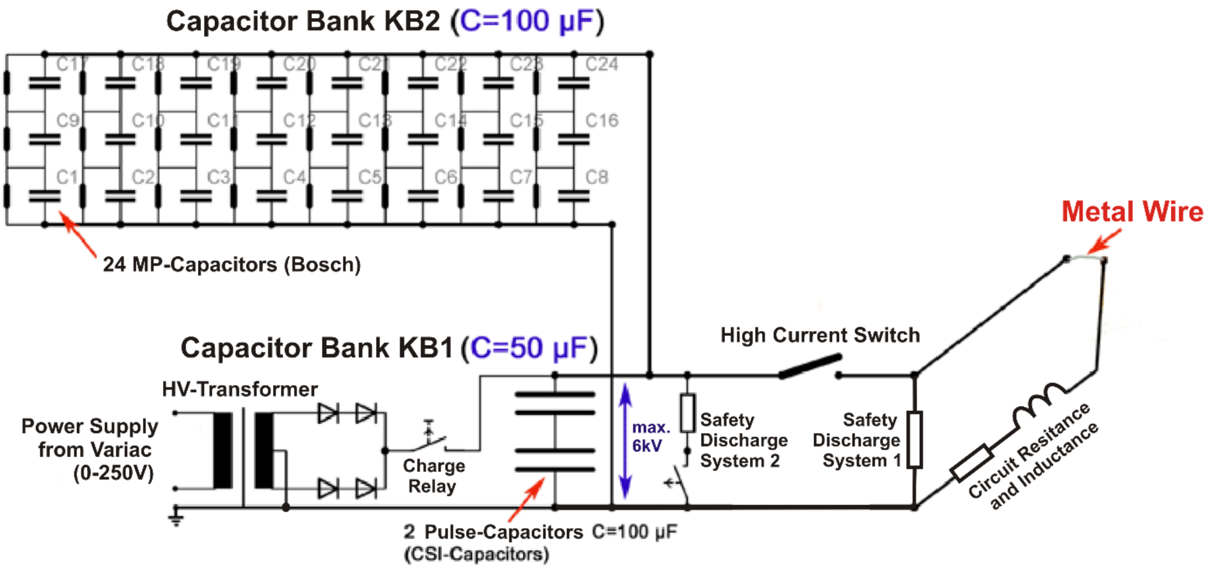

Figure 3.1: Circuit diagram of the capacitor bank setup

The basic capacitor bank system contains a charge circuit with a so-called *Oil Burner Ignition Transformer* (OBIT), which provides a peak output voltage of around 6,2 kV. The two high voltage outputs are rectified and then brought together. Over a high voltage reed relay (charge relay) the two capacitor banks are able to be charged up to a maximum voltage of 6 kV. The input voltage of the transformer is controllable by a variac transformer which supplies the HV-transformer from a safe distance. After reaching a certain voltage, which lies between 1000 V and 6000 V, the charge circuit is switched off by the charge relay.

Then *High Current Switch* is triggered by a pneumatic system, which allows a safe firing of the system. The discharge current is conducted through a high voltage coaxial cable (RG164U) to the plasma chamber (Fig. 3.3 ⑤), which allows a low inductance energy transformation (compare 2.2.2) [14]. Inside the massively constructed chamber, wires of a length of up to 250 mm are able to be attached onto a special clamp device (Figure 3.4). The discharge current returns within the outer shell of the coaxial cable back to the device, where an additional inductance (Fig. 3.3 ⑧) can be mounted if so required.

Over a coaxial shunt resistor (Fig. 3.3 ⑨) the discharge current is measured and stored by a digital oscilloscope. When one activates the *High Current Switch*, the capacitor is also discharged through the *Safety Discharge System 1* (Fig. 3.3 ④). The *Safety Discharge System 1* contains 12 ceramic resistors (Rosenthal *GK19.5x120*, 2,5 kΩ, U_{max}=1600 V), which are connected in series. With a total resistance of 30 kΩ, the time constant τ is: RC=30 kΩ·150 µF=4,5 s.

When one compares this value with the time constant of the circuit containing a metal wire ($T \approx 163\,\mu s$), the loss of energy during the pulse discharge dissipation within the *safety discharge system 1* is negligible. Nevertheless, dangerous charges of high voltage inside the capacitor bank can dissipate after $6\tau = 27\,s$ to safe voltage values ($U_C < 15\,V$), even if no metal wire being placed between the electrodes within the discharge chamber.

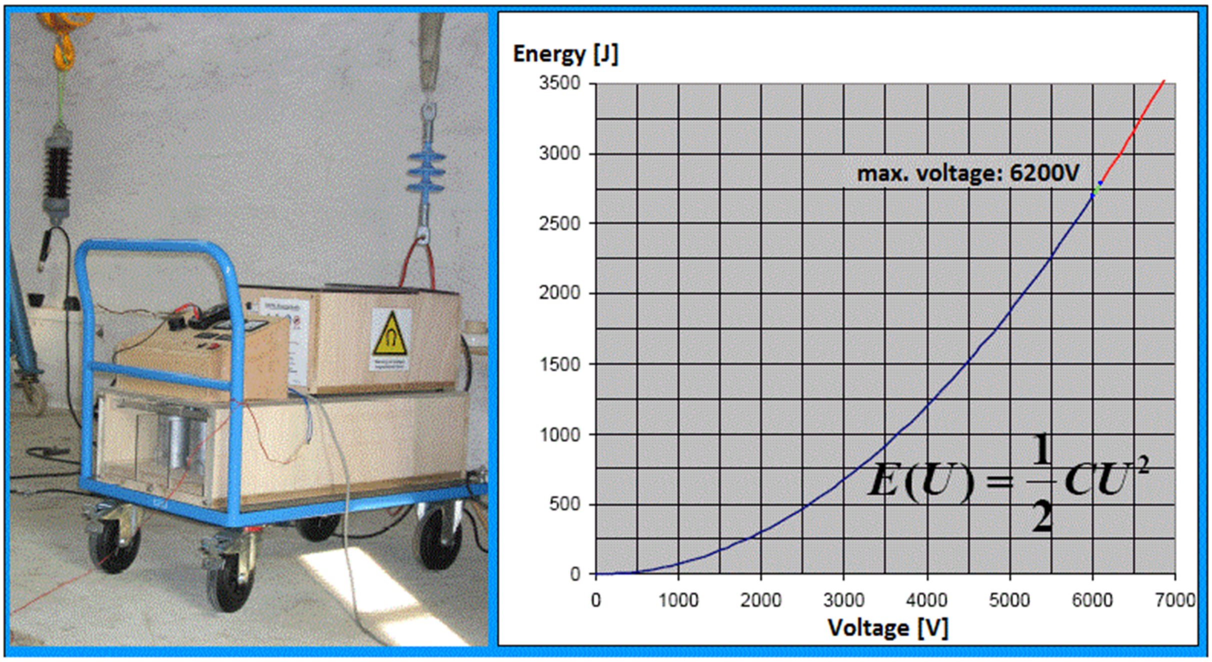

Figure 3.2: An energy diagram from the capacitor bank

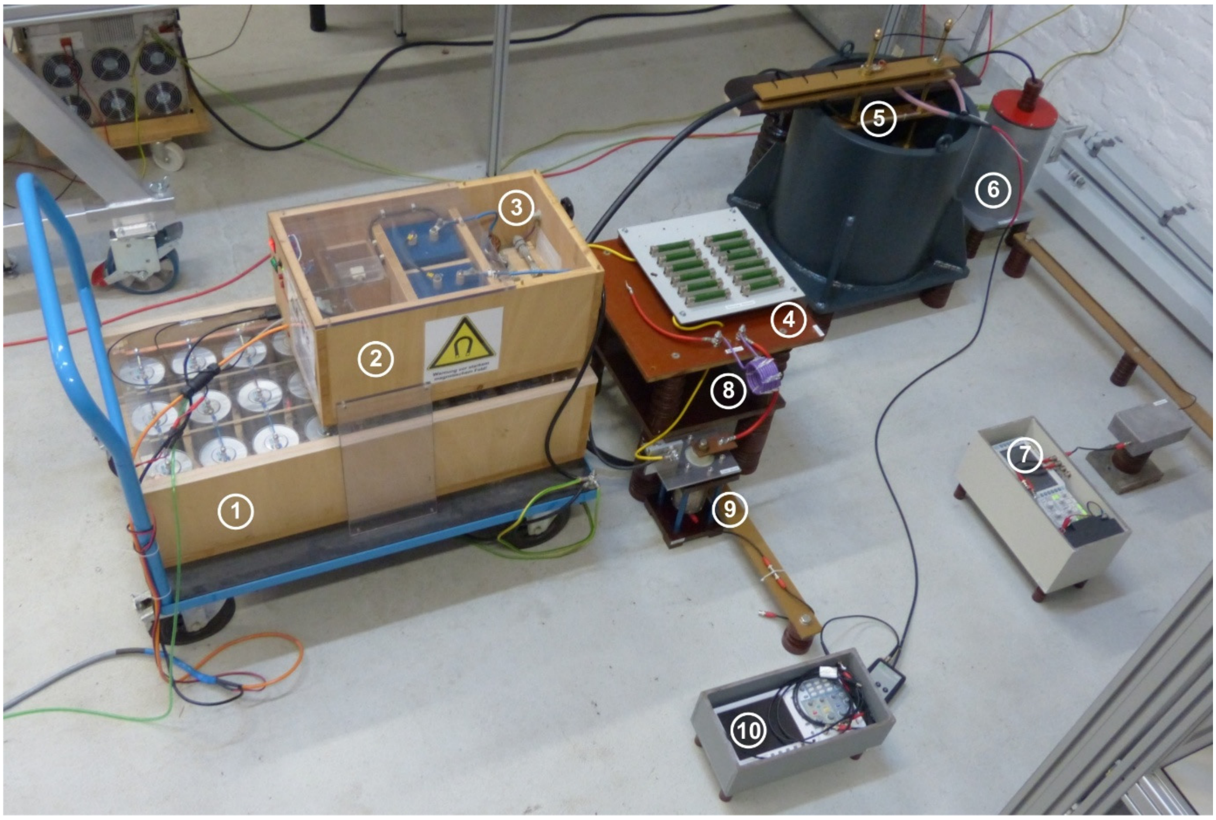

Figure 3.3: Experimental setup: ① capacitor bank KB2, ② capacitor Bank KB1, ③ high current switch, ④ safety discharge system 1, ⑤ discharge chamber with metal wire, ⑥ high voltage divider, ⑦ digital storage oscillosope nr. 2, ⑧ inductance, ⑨ coaxial shunt resistor, ⑩ digital storage oscillosope nr. 1

Because strong shock waves are produced by the exploding wires inside the discharge chamber, a solid construction had to be built in order to be able to clamp down the wire threads. The steel assembly had to be electrically isolated from the discharge chamber and was realised to allow any kind of simple attachment of one or two coaxial cables in parallel (RG164U or RG218U), which supply the experiment from the capacitor bank. Furthermore, it should be possible to clamp down wires of a length of up to 250 mm (diameter 600 µm-800 µm) between two electrodes. The distance of these electrodes should be adjustable within the range of 0-250 mm, without having to change the center line once it is fastened by the clamp device, in regards to the currents path. This guarantees for a nearly constant inductance value regarding the clamp device irrespectively of the used wire length and diameter.

After taking all these requirements into consideration, a CAD model of the clamp device was built (Figure 3.4). The central conductor of the high voltage cable RG164U, which runs from the capacitor bank, is fastened to a threaded rod (M16) at Ⓐ, while the outer conductor is attached to another threaded rod (M16) at Ⓕ. The threaded rods are fixed in place by massive terminals made of brass at Ⓒ and Ⓓ. Through each of these terminals a horizontally hole was drilled, they each allow a single threaded metal rode (M16) to be place through them. These two threaded rods act as electrodes with a variable distance, between which a wire can be attached. Halfway between Ⓐ-Ⓒ and Ⓕ-Ⓓ an RG213U coaxial cable is connected so as to be able to measure the decline in voltage between Ⓑ and Ⓔ.

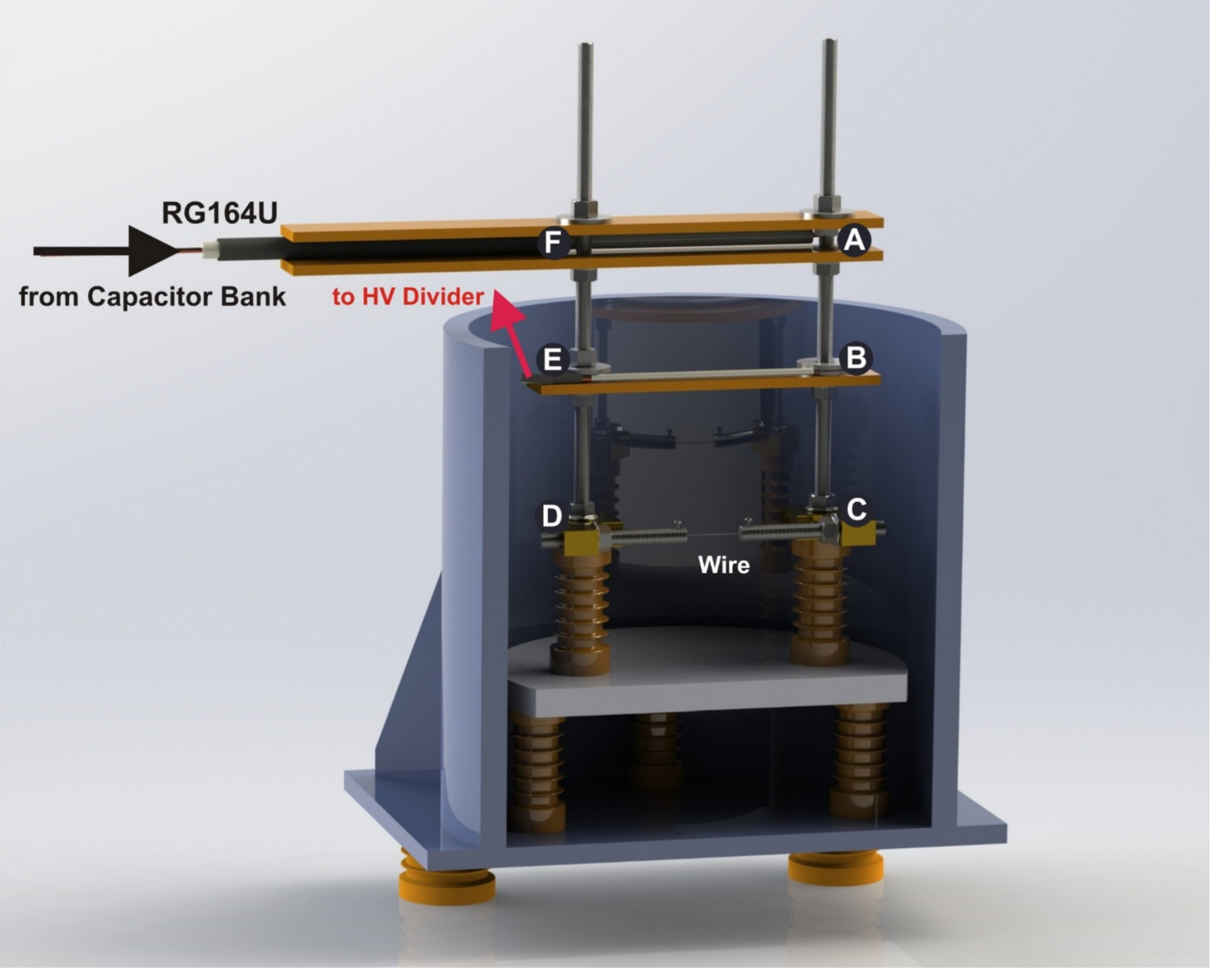

Figure 3.4: CAD model of the clamp device inside the discharge chamber (geometric section)

By analysing the geometric dimensions of the capacitor bank one is capable of designing a circuit diagram which also incorporates the inductance values of the bussbars (Figure 3.5). Within *PSpice* the designed circuit model of the capacitor bank was simulated. Variations regarding the utilised inductances produced a qualitative overlap compared with short circuit measurements (Figure 3.6). Since the circuit diagram in Figure 3.5 would be too complex for the modeling approaches described in chapter 5, a simpler equivalent circuit (*RLC*) had to be found. Therefore equation (2.3c) was used to find a suitable circuit inductance L, so that the gained current curve $I_{ud}(t)$ matches with the measured current I_{total}. The obtained circuit parameters are: C=150 μF, L=4,36 μH, R_{cir}≈44 mΩ

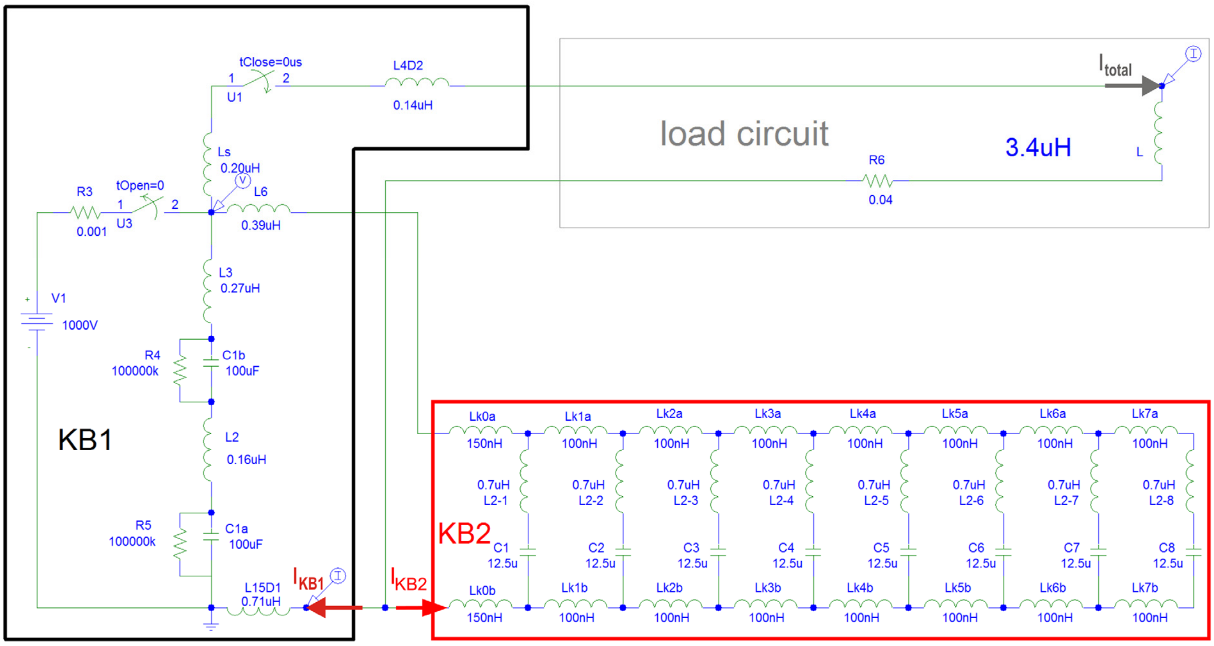

Figure 3.5: Detailed circuit diagram of the experimental setup. The main capacitor bank KB1 (50 μF) is connected in parallel to the additional capacitor bank KB2 (100 μF). The whole capacitor bank has a capacitance of 150 μF at a max. charge voltage of U_{C0}=6 kV.

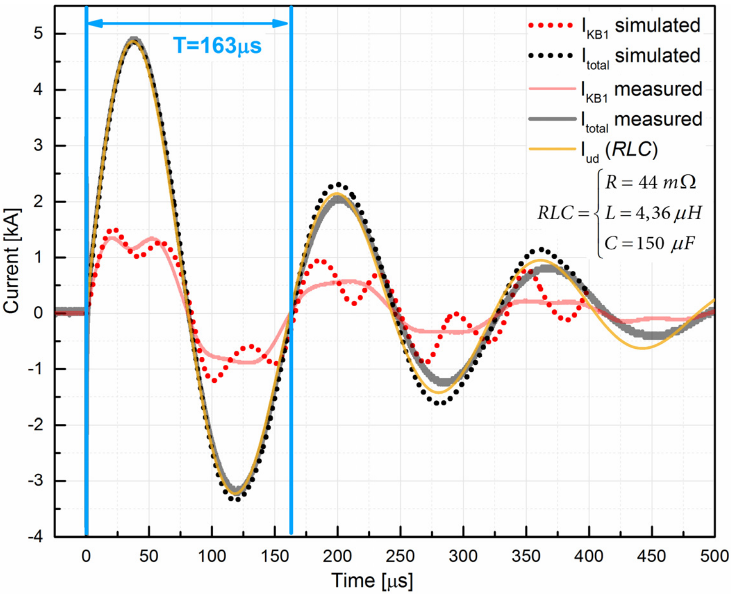

Figure 3.6: Discharge current of the capacitor bank network. Dotted lines represent simulated values. $I_{ud}(RLC)$ represents the computation with equation (2.3c).

3.2 The setup in order to measure discharges

During the procedure of charging up the capacitor bank, the voltage of these capacitors is measured by a high voltage probe (VOLTCRAFT H 40) at a ratio of 1000:1 and with a 10 MΩ multimeter (Figure 3.7). With this configuration the charge voltage is able to be adjusted up to an accuracy of approximately 10 V.

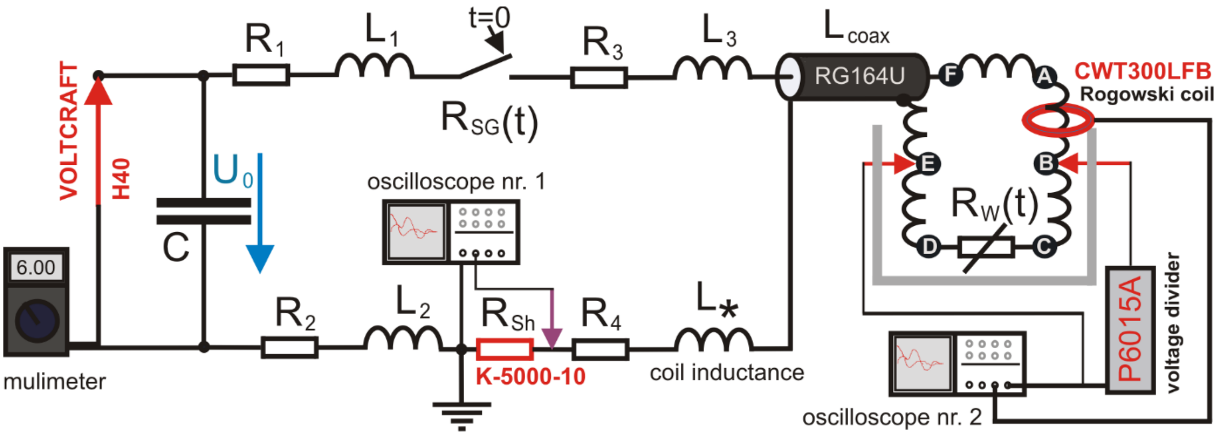

Figure 3.7: Schematic of the setup required for discharge measurements (compare also with Fig. 3.4)

The main interest of this project are the discharge measurements, which display the characteristics of the exploding wires, so to be precise the decline in voltage throughout the wire resp. the wires plasma is measured by a high voltage probe from Tektronix (P6015A). Due to geometric limitations, it is not possible to measure the voltage directly from the relevant wire itself. Since the voltage is taped at the points Ⓑ and Ⓔ by a RG213U coaxial cable (compare also Figure 3.4), the voltage U_{BE} is not exactly the same voltage as is U_{CD}. So as to be able to estimate this voltage difference one has to determine the inductance of the bridge circuit. The clamp voltage U_{clamp} is capable of being found out with the formula

$$U_{clamp}(t) = U_{BE}(t) = (R_{BC} + R_{CD}(t) + R_{DE})I(t) + (L_{BC} + L_{CD} + L_{DE} - 2L_{BC,DE})\frac{dI(t)}{dt} \ , \tag{2.17}$$

where the inductances L_{BC}, L_{CD}, L_{DE} (wires with length l, radius r) may be computed by [15]:

$$L = \frac{\mu_0}{2\pi}\left[\ln\left(\frac{2l}{r}\right) - \frac{3}{4}\right] . \tag{2.18}$$

According to Rosa and Grover [16] the mutual inductance of two parallel wires (as $L_{BC,DE}$) with length l and distance D is

$$M = \frac{\mu_0}{2\pi}\left[l \cdot \ln\frac{l + \sqrt{l^2 + D^2}}{D} - \sqrt{l^2 + D^2} + D\right] . \tag{2.19}$$

If one ignores R_{BC} and R_{DE} the measured voltage may be described by:

$$U_{BE}(t) = R_{CD}(t)I(t) + L_{clamp}\frac{dI(t)}{dt} \tag{2.20}$$

The value for L_{clamp} is calculable with the equations (2.18) and (2.19). By incorporating the geometric values from Figure 3.4 one is able to gauge the existing inductance:

$$L_{clamp} = L_{BC} + L_{CD} + L_{DE} - 2L_{BC,DE} = 97nH + (282 \pm 106)nH + 97nH - 2 \cdot 10nH \approx (456 \pm 106)nH$$

When one assumes a total circuit inductance of 4.36 µH the current rise at t=0 µs is able to be approximated by:

$$\left.\frac{dI(t)}{dt}\right|_{t=0} = \frac{U_{C0}}{L_{circuit}} = \frac{6kV}{4.36\mu H} \approx 1.38kA/\mu s$$

If an inductance of L_{clamp}= 456 nH is given, then the maximum voltage error is determinable:

$$\Delta U_{max} = L_{clamp}\left(\frac{dI}{dt}\right)_{max} = 0.456\mu H \cdot 1.38kA/\mu s \approx 629V$$

In previous tests with the aforementioned high voltage probe (P6015A), significant values of RF-noise were determined, when the probe is in close proximity to high current setups (I>10 kA), which made it quite difficult to attain usable measurements. In order to be able to overcome this challenge, it was necessary to manufacture a shield for the high voltage probe (Figure 3.8). The low voltage output from the voltage divider is attached to a battery-driven oscilloscope from Owon (DS6062). This oscilloscope is also placed inside a shielding steel box (Figure 3.9c), isolators separate it from the floor.

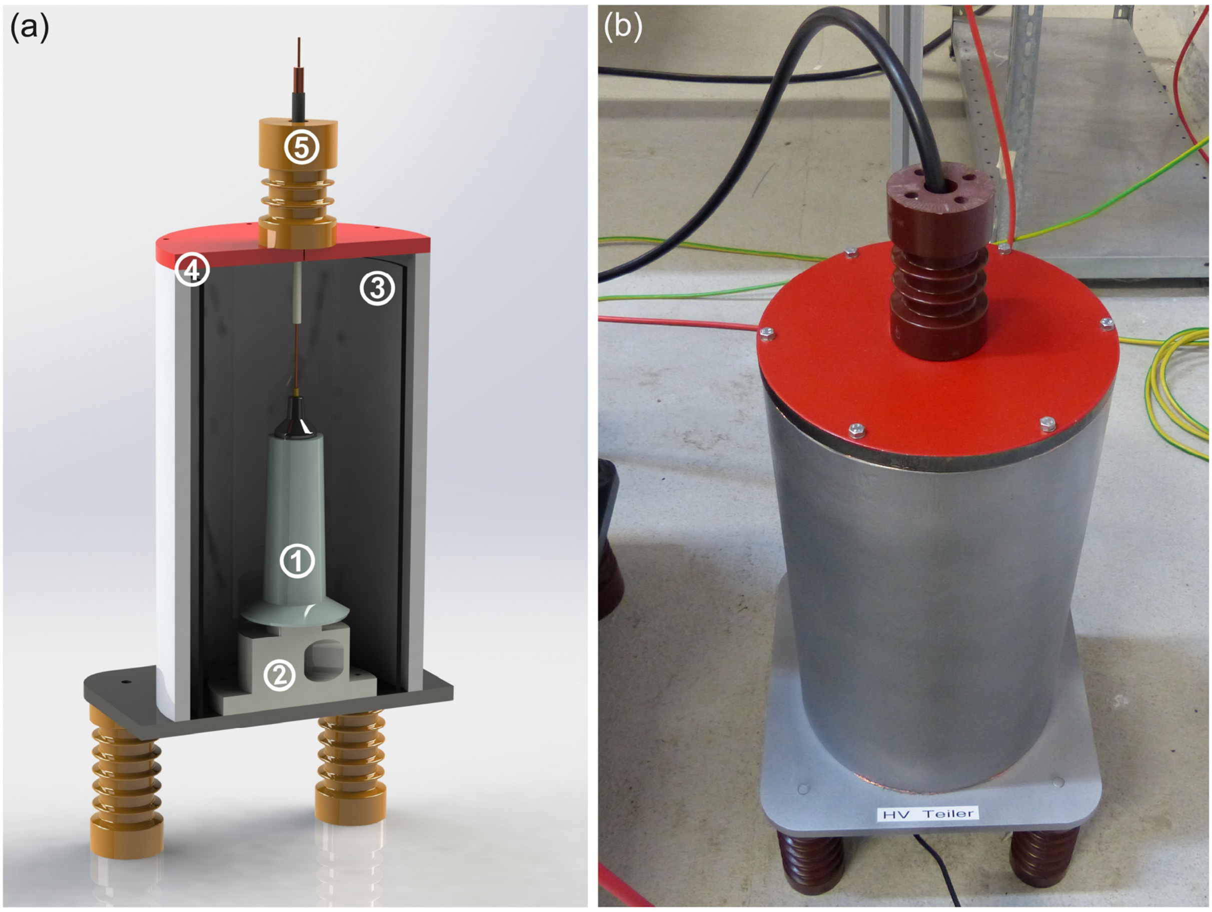

Figure 3.8 (a) CAD-model - a section of the high voltage divider (b) Practical realisation
① HV probe Tektronix P6015A
② turned part made of POM as attachment
③ Isolation made of acrylic glass
④ housing made of S235JR steel
⑤ HV feed through with RG213U coaxial cable

After triggering the discharge of the capacitor bank, the given discharge current is measured by a high current coaxial shunt resistor (Figure 3.9a) from the manufacturer T&M RESEARCH PRODUCTS, Inc. (K-5000-10). As a second option the discharge current can also be measured by a Rogowski coil (CWT 300LFB- 0.1mV/A), which is placed around one of the current-carrying threaded rods within the discharge chamber (Figure 3.9b). Both measurement devices have a BNC output and therefore it is possible to connect them to the digital storage scope (Owon DS6062), which is used in order to be to able capture current curves while pulse discharges take place (Figure 3.9c). A comparison of the two types of measurement resulted in a perfect overlap of the current curves (Figure 3.9d). No matter how one positions the Rogowski coil around the threaded rode (in one instance around the current-carrying threaded rod in the center, in another case touching the current-carrying threaded rod) one is unable to determine significant differences in comparison to measurements made with the coaxial shunt resistor. However the positioning of the Rogowksi coil seems to be even less critical than as it is mentioned within the producers manual [17].

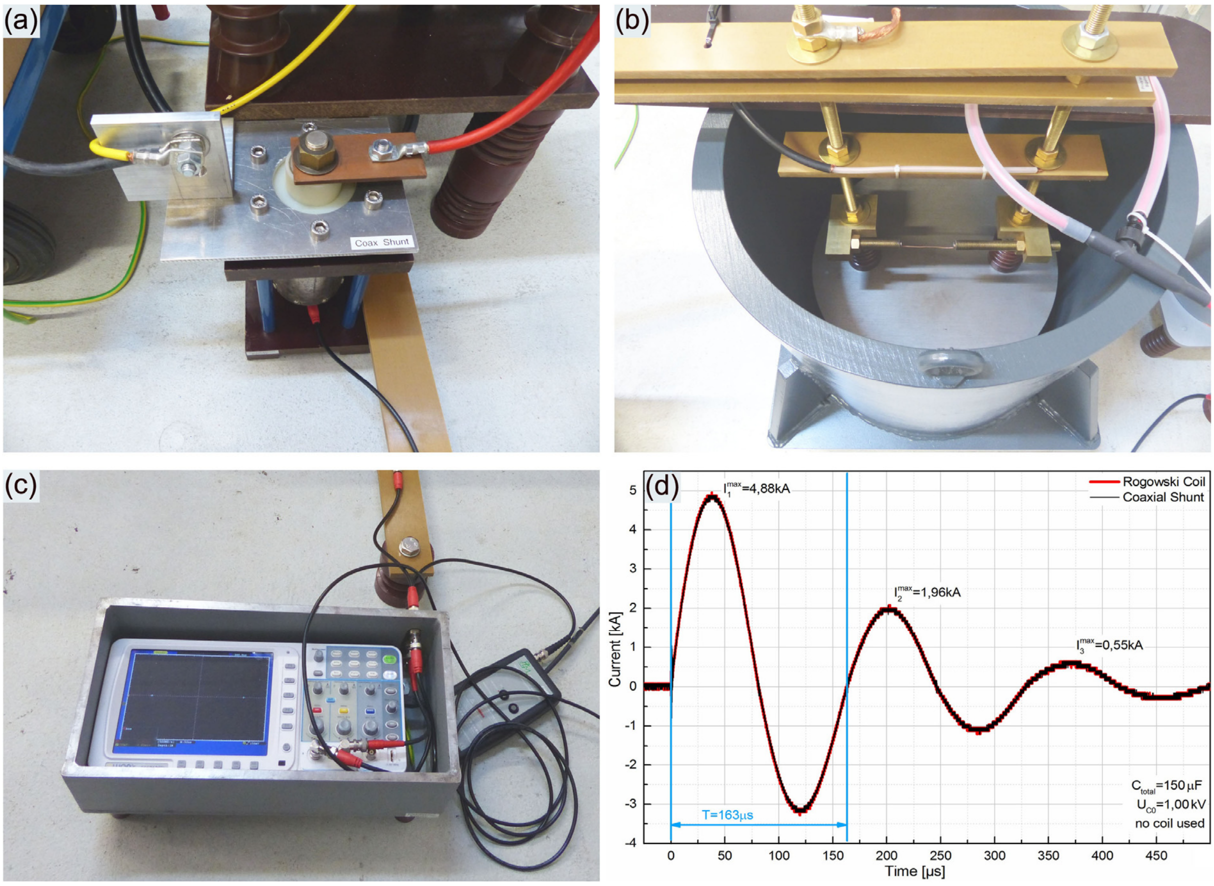

Figure 3.9: Current measurement devices
(a) Coaxial shunt resistor
(b) Rogowski coil (red loop around the threaded rod)
(c) battery powered digital oscilloscope (Owon DS6062) inside a shielded box
(d) comparison of current measurements

4. Experiments

4.1 Fundamentals

4.1.1 Properties of wire material

In the literature from 1959 onwards nearly all experiments with exploding wires were performed with pure metals i.e. Iron, Copper, Aluminium and Tungsten [4], [5]. Only less studies have been written containing alloys [18], [19]. The experiments presented within this thesis are all done with stainless steel wires which are made of the alloy *1.4301* or *X5CrNi18-10.* As an Austenite this alloy is an acid-proof stainless steel, widely used in industry within Europe and well known by the popular name of *V2A*[1]. It contains 17,0-19,0% Cr, 9,0-11,5% Ni, less than 2% Mn and the total amount of Fe inside the alloy is around 72% [20]. The specific resistance of pure iron (ρ≈0,1 Ωmm²/m) is typically much lower than the specific resistance of iron alloys which include nickel and chrome [21]. Steel wires made of *X5CrNi18-10* are better than wires made of pure iron regarding their ideal resistance R_{cd}, which is needed in order to reach a critical damping behaviour. Typically, the steel alloy *X5CrNi18-10* has a specific resistance of ρ≈0,73 Ωmm²/m at 20°C [20], which is around 7 times higher than the specific resistance of iron alloys (0,05% C), which do not contain chrome and nickel [21]. At 1000°C *X5CrNi18-10* reaches a specific resistance of ρ≈1,25 Ωmm²/m [21], [22]. Furthermore, wires made of *X5CrNi18-10* offer some added advantages in experiments dealing with exploding wires. For example this alloy is easily available in many diameters, has a low price and does not corrode.

In order to understand the heating process and it´s own physical states of matter (solid, liquid and gaseous) in more detail, one must compute each phase of the *thermal enthalpy* ΔH. Figure 4.1 shows the computed thermal enthalpy graph, which includes values from literature as well as values which had to be approximated. In general, the total amount of thermal energy or enthalpy, ΔH, associated with the specific heat capacity (C_p) is given by:

$$\Delta H = \int_{T_1}^{T_2} C_p dT \tag{4.1}$$

According to [23] the specific heat capacity [J/gK] of the alloy AISI 304[2], which is equivalent to *X5CrNi18-10*, one is able to describe it with a good approximation by the polynomial

$$C_p = 0{,}443 + 2 \cdot 10^{-4} T - 8 \cdot 10^{-10} T^2 \tag{4.2}$$

within a suitable temperature range of T=[298; 1727] K. Via analytical integration of the equation (4.2) the curve of thermal enthalpy was able to be drawn, which starts from room temperature at 298 K (green curve "solid" in Fig. 4.1). The temperature at which the alloy starts to melt is the so-called *solidus temperature* (T_s), which is reached at 1673 K [23]. At 1727 K the melting process is completed, this is called the *liquidus temperature* (T_l) [23]. According to the same source the heat that is required during solid-to-liquid transformations, is the enthalpy or latent heat of melting (ΔH_f). In regards to the alloy AISI 304 the latent heat of melting is ΔH_f =290 J/g. Since the value for the specific heat capacity of AISI 304 in regards to its liquid phase (C_{pL}) could not be found in any literature, one may use the *Kopp-Neumann role of mixtures*

---

[1] abbreviation for *Versuchschmelze 2 Austenit*

[2] material designation in Anglo-American regions

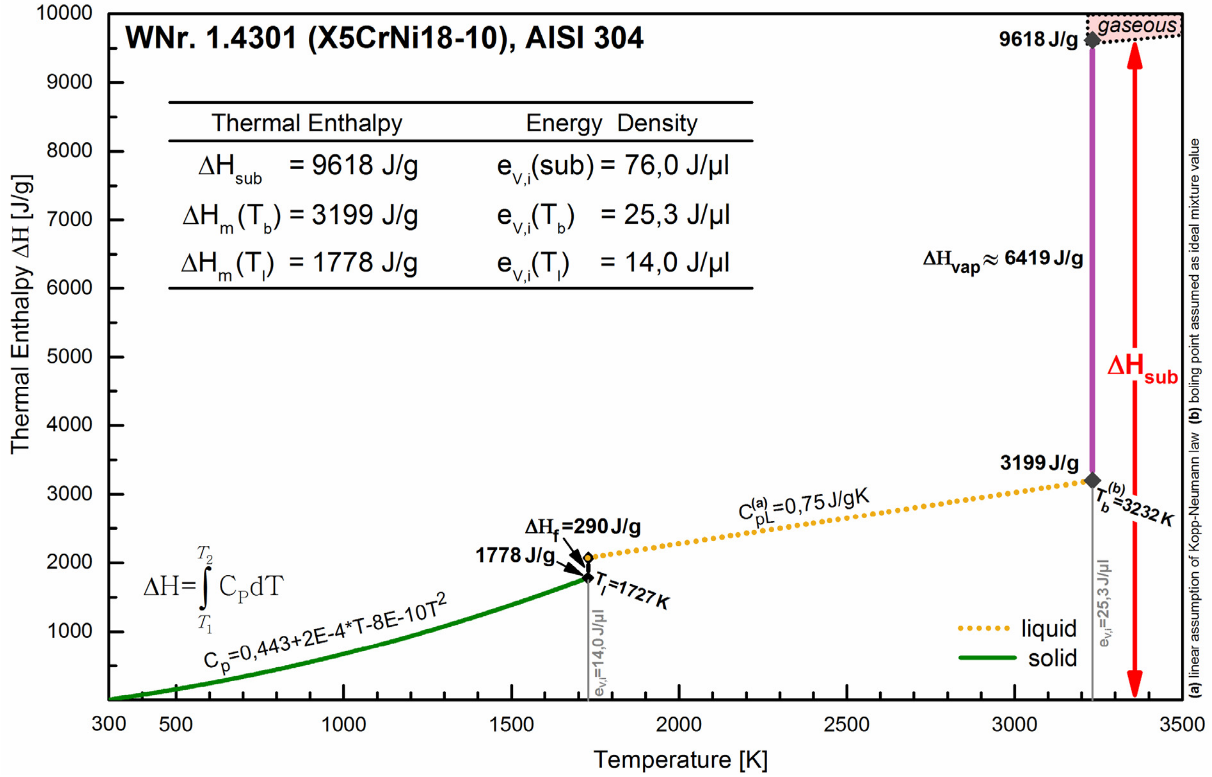

Figure 4.1: Thermal Enthalpy *X5CrNi18-10*. The energy density is related to the initial volume ($\boldsymbol{V}, \boldsymbol{i}$)

in order to estimate C_{pL} [24]:

$$C_{pL} = \sum_{i=1}^{n} Y_i (C_P)_{L_i} \tag{4.3}$$

By using the atomic fractions of the alloy elements (Y_i) together with the heat capacities of the pure elements [23], the specific heat capacity for the liquid alloy then becomes:

$$C_{pL} \approx (0{,}762 \cdot 0{,}72 + 0{,}78 \cdot 0{,}18 + 0{,}63 \cdot 0{,}1) \frac{J}{gK} \approx 0{,}75 \frac{J}{gK} \tag{4.4}$$

Since the boiling temperature (T_b) of AISI 304 was not able to be found in any literature, it´s value had to be estimated from the boiling temperatures from the pure elements within the alloy. When neglecting the component of Manganese (1%) within the alloy, one is able to estimate the boiling temperature of the ternary system Fe-Cr-Ni. Holleman and Wiberg [25] provide the values of T_b=3070°C (Fe), T_b=2640°C (Cr) and T_b=2730°C (Ni). By assuming a *non-azeotropic ideal mixture behaviour* [26], the boiling point of the AISI 304 alloy is roughly:

$$T_b(AISI304) \approx 3070°C \cdot 0{,}72 + 2640°C \cdot 0{,}18 + 2730°C \cdot 0{,}10 \approx 2959°C = 3232\,K \tag{4.5}$$

When assuming C_{pL}≈0,75 J/gK (equation 4.4) as a constant value wright up to the determined boiling temperature, one may reach a thermal enthalpy of 3199 J/g at T_b. By using the *vaporisation enthalpy* of the pure elements (H_{vap}(Fe)=6340 J/g, H_{vap}(Cr)=6700 J/g, H_{vap}(Ni)=6480 J/g) according to the literature [27] also respecting the masses proportions, one receives:

$$\Delta \overline{H}_{vap} \approx (6340 \cdot 0{,}72 + 6700 \cdot 0{,}18 + 6480 \cdot 0{,}1) \frac{J}{g} \approx 6419 \frac{J}{g} \tag{4.6}$$

Together with the enthalpy at the boiling temperature (T_b), the total enthalpy in order to reach the gaseous states of matter, the so-called *sublimation enthalpy* (ΔH_{sub}), then reaches 9618 J/g.

4.1.2 Experimental procedure

Before each experiment the required wire diameter was choosen from the available assortment of *X5CrNi18-10* steel wires. The wires were cut to the needed length and clamped within special copper cylinders (Figure 4.2). These copper cylinders (50 mm long, 4 mm diameter) were produced previously with a hole at one front end (d=1,0 mm, l=12 mm). However, each end of the steel wire is able to be inserted into the hole of one copper cylinder. After crimping the copper cylinders, the steel wires are attached properly to the copper cylinders and must then be cleaned with Isopropanol. This procedure gets rid of existing grease residue, which could affect the formation of the plasma during the pulsed discharge as well as influence the repeatability in a negative way (chapter 4.1.4).
In order to perform an experiment, the copper cylinders are clamped with screws in massive brass supports (Figure 4.3), this guarantees a low resistance connection, which is far less than the typical circuit resistance (R_{cir}≈36 mΩ).

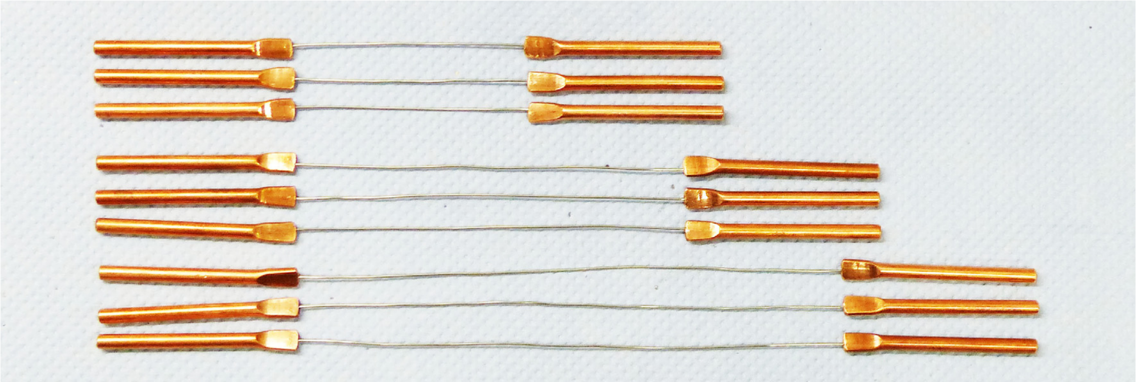

Figure 4.2: Set of steel wires crimped inside copper cylinders

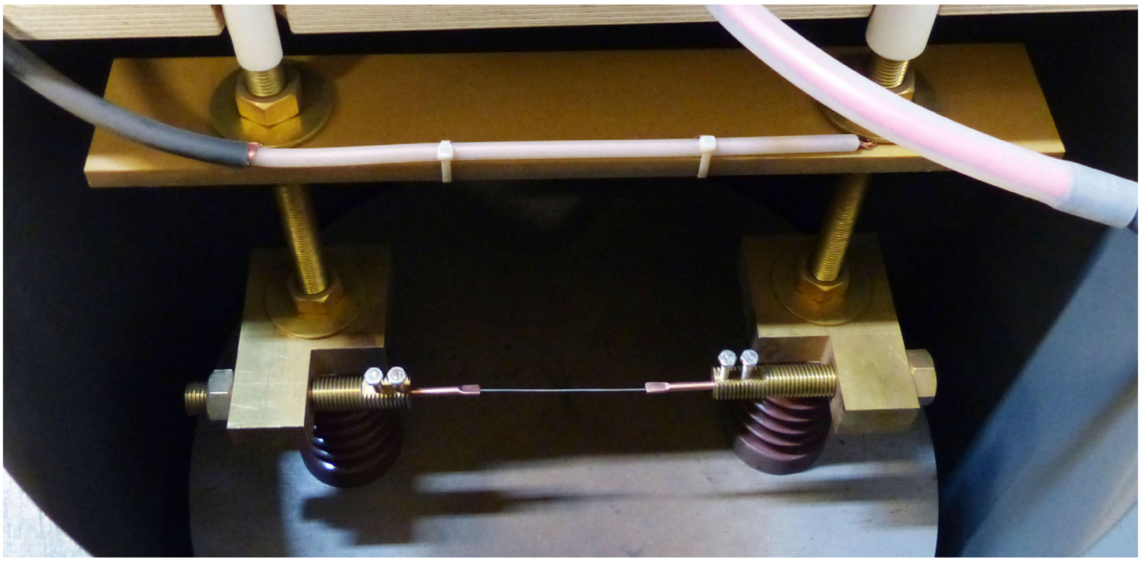

Figure 4.3: Clamped steel wire setup, ready to perform a pulsed discharge

4.1.3 Method of data analysis

After charging up the capacitor bank and triggering the discharge, the measured current and voltage waveform provided by the oscilloscope is able to be stored on the computer. Typically, the memory depth from the oscilloscope is set to 100 kS at a sample rate of 100 MS/s. This then gives a time step of 10 ns. However, the captured data had to be analysed and post processed numerically in many steps (Figure 4.4).

First the measured current and voltage data had to be smoothed out with a *Savitzky-Golay-Filter* [28] in order to avoid strong oscillations. These are mainly caused by the switching spark gap given at the time of zero crossings of the current. In comparison to other filter methods the high frequencies are not just cut out, but also included in the computation, which makes this specific filter method very powerful. Starting with the smoothed out current *I(t)* and clamp voltage $U_{clamp}(t)$ one is able to compute a variety of time dependent quantities, which in turn help to understand the physical phenomena involved.

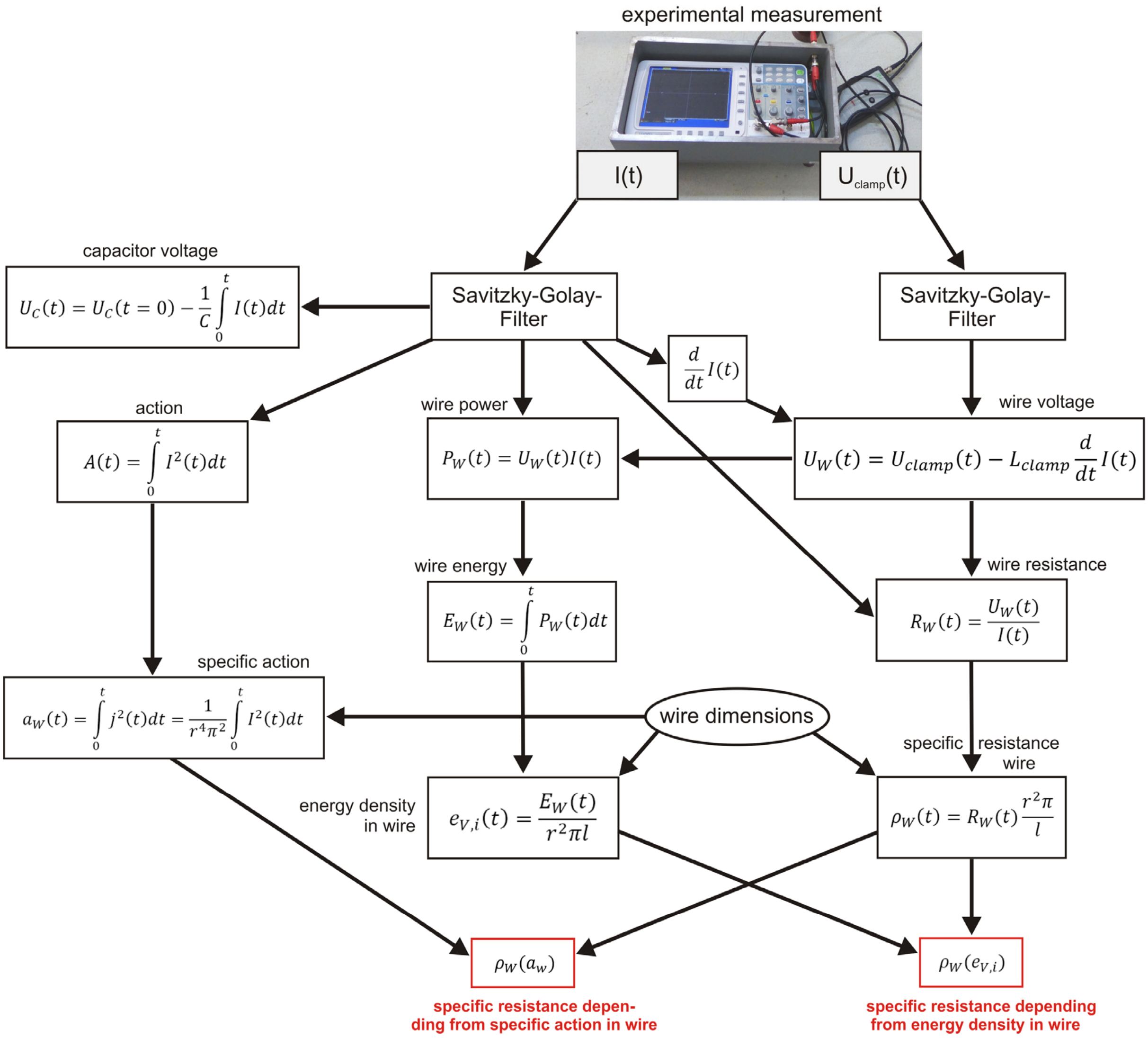

Figure 4.4: Schematic diagram that illustrates the post processing

First of all, the filtered current curve may be used to compute the voltage[3] of the capacitor bank by numerical integration with:

$$U_C(t) = U_C(t=0) - \frac{1}{C}\int_0^t I(t)\,dt \tag{4.7}$$

Within this thesis the potential difference between the wire endings is called *wire voltage* U_W. According to chapter 3.2 the voltage must be corrected in regard to the inductive voltage drop with

$$U_W(t) = U_{clamp}(t) - L_{clamp}\frac{d}{dt}I(t)\ , \tag{4.8}$$

which requires a previous numerical computation of the *current deviation*

$$s(t) = \frac{d}{dt}I(t)\ . \tag{4.9}$$

This allows the computation of the *wire resp. plasma resistance* in dependence of time

$$R_W(t) = \frac{U_W(t)}{I(t)}\ , \tag{4.10}$$

as well as the wire power described by

$$P_W(t) = U_W(t)I(t)\ . \tag{4.11}$$

The *energy absorbed in the wire resp. plasma* is able to be computed via numerical integration of the wire power:

$$E_W(t) = \int_0^t P_W(t)\,dt \tag{4.12}$$

When assuming an isochoric condition (compare chapter 5.2), the cross section of the wire (S) stays constant when the plasma pulse appears. Then one may define an *energy density in the wire resp. wire plasma* $e_{V,i}$ in respect to the wire dimensions (length l, radius r):

$$e_{V,i}(t) = \frac{E_W(t)}{r^2\pi l} \tag{4.13}$$

With the assumption of an isochoric behaviour, it is also possible to define the time dependent *specific resistance of the wire resp. wire plasma* described by:

$$\rho_W(t) = R_W(t)\frac{r^2\pi}{l} \tag{4.14}$$

Finally, the time dependent specific resistance[4] of the wire resp. wire plasma $\rho_W(t)$ may be represented, depending on the energy density within the wire resp. wire plasma ($e_{V,i}$) as a time independent function:

$$\rho_W\left[e_{V,i}(t)\right] = \rho_W\left(e_{V,i}\right) \tag{4.15}$$

---

[3] The capacitor voltage computed by this method gives an excellent value for experimental analysis, because no measuring cables are needed for potential measurements.

[4] Specific resistance is a noun for *electrical resistivity* (also known as *specific electrical resistance* or *volume resistivity*)

This representation offers the opportunity to compute a time independent resistance characteristic curve for any type of wire. The "action integral", or simply the "action" is a quantity which results from a superficial similarity between the quantity it represents and the action in classical mechanics [29]. With the definition

$$A\left(t\right)=\int_{0}^{t}I^{2}\left(t\right)dt \quad , \tag{4.16}$$

the action is a very useful quantity in order to describe the "thermal inertia" of any circuit element in an *RLC* circuit. In a pulsed capacitor discharge circuit, the value for *A(t→∞)* converges towards a fixed value A_∞. When looking at an arbitrary resistor element R_i within the circuit, the absorbed energy in this element is able to be determined by simply computing

$$E_{R_i}(t)=A(t)R_i \quad , \tag{4.17}$$

if one regards the resistance as constant (compare chapter 4.2.2.4). In the case of a non-constant resistance, which the exploding wire within a pulsed discharge circuit represents, the resistance of the wire $R_w(t)$ may be expressed as a function of the involved Action *A(t)*:

$$R_W(t)=R_W\left[A(t)\right] \tag{4.18}$$

Further the specific action of a resistive element R_i may be defined as

$$a_{R_i}\left(t\right)=\frac{\partial A\left(t\right)}{dS^2}=\int_{0}^{t}j^2\left(t\right)dt=\frac{1}{S^2}\int_{0}^{t}I^2\left(t\right)dt \quad , \tag{4.19}$$

where *S* is the cross section of the resistive element and *j* is the *homogenous current density*. In the case of a round wire with radius *r* the specific action is given by:

$$a_W\left(t\right)=\int_{0}^{t}j^2\left(t\right)dt=\frac{1}{r^4\pi^2}\int_{0}^{t}I^2\left(t\right)dt \quad . \tag{4.20}$$

Instead of writing the specific resistance ρ as a function of energy density (equation 4.15) one may also write ρ_w in a dependency with the specific action in the wire:

$$\rho_W\left[a_W(t)\right]=\rho_W\left(a_W\right) \tag{4.21}$$

Both expressions (equation 4.15 and 4.21) offer a time independent description of the resistivity of the wire material and are connected to each other in the following way [30]:

$$\int_{0}^{t}\rho_W\left[a_W(t)\right]da_W(t)=\int_{0}^{t}\rho_W(t)\frac{da_W(t)}{dt}dt=\int_{0}^{t}\rho_W(t)j^2(t)dt=\int_{0}^{t}\frac{de_{V,i}(t)}{dt}dt=e_{V,i}(t) \tag{4.22}$$

Because the energy density within the wire ($e_{V,i}$) is a more understandable quantity compared to the specific action (a_w), most of the analysed data within this thesis was gained by using the representation of the specific resistance in dependence of the energy density in the wire (equation 4.15).

4.1.4 Accuracy and repeatability

Before starting with parameter variations, the validity of the performed experiments should be determined. When repeating a pulsed wire discharge by using the same circuit parameters (U_{C0}, C, L, R_{cir}) and wire dimensions (l, d), the measured current $I(t)$ and voltage $U_w(t)$ differ from one experiment to another. The reason for this behaviour is an inaccuracy of the charge voltage ($U_{C0} \pm \Delta U_{C0}$), a variation of the capacitance ($C \pm \Delta C$) and a geometric variation of the wire dimensions ($l \pm \Delta l$, $d \pm \Delta d$). Furthermore, the moment when the plasma pulse occurs depends on complex physical mechanisms with sensitive boundaries, which are also responsible for a divergence of the current $I(t)$ from one experiment to the next experiment [18].

To figure out the magnitude of the deviations, the current waveform $I(t)$ was measured for five pieces of *X5CrNi18-10* steel wire with a length of 120 mm each and a nominal diameter of 700 µm. Precise preparation of the used wires, within all experiments described in this thesis, made it possible to guarantee a maximum variation of wire length of less than 1 mm concerning all wire lengths. The diameter of the 700 µm wire was measured with a micrometre screw in horizontal (d_h) and vertical direction (d_v) at 13 different wire sample positions, where around one half of the measurements was done in horizontal and the other half in vertical direction. Figure 4.5 shows the wire samples (a), the diameter orientation of measurements (b) and scatter of the wire diameters (c). The mean average diameter was determined as 700,15 µm with a standard deviation of 7,8 µm. Therefore, the diameter deviation is only about 1 % and the corresponding cross section deviation only about 2 %.

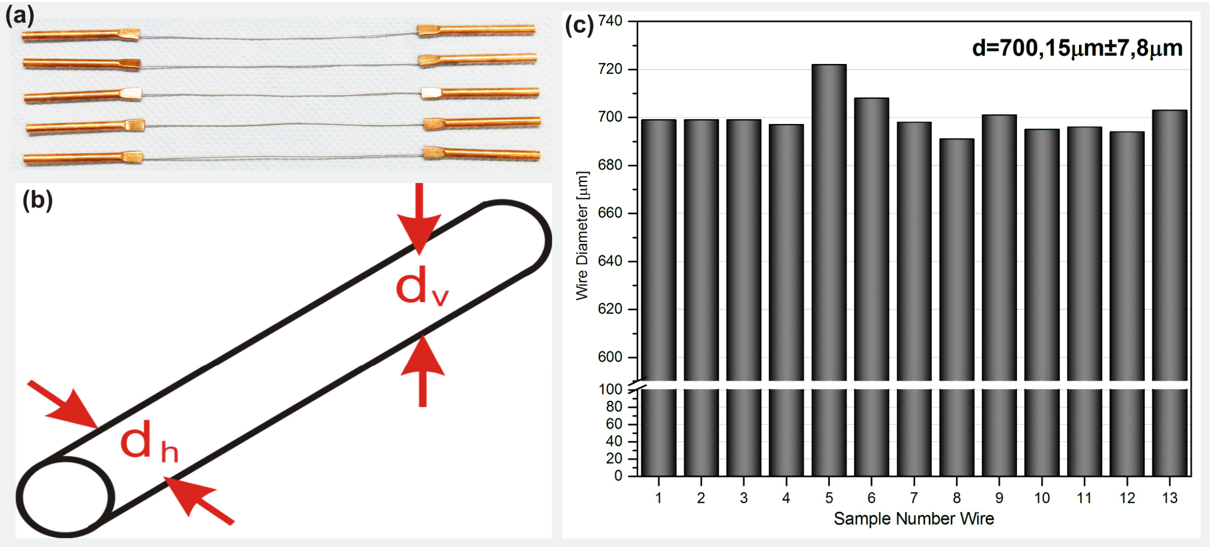

Figure 4.5: (a) wire samples (l=120 mm, d=700 µm) clamped within copper cylinders, (b) diameter measurements in horizontal (d_h) and vertical direction (d_v), (c) deviation of wire diameters

During all the performed experiments described in this thesis, the capacitance of the entire capacitor bank was measured with a *RLC*-meter at random intervals. The typical capacitance measurement was 150,00 µF. Depending on the temperature and previous pulse experiments, the measured values differ by less than ΔC=±3 µF, which results in a deviation of about 2 %. According to chapter 3.2 the initial capacitor bank voltage is able to be adjusted with an accuracy of about 10 V. At a maximum charge voltage of 6,00 kV, this is equivalent to an adjustable voltage accuracy of 0,2 %. Figure 4.6 shows the measured current (a) and voltage (b) waveforms of the repetitive experiments, which represent an excellent repeatability. During the heat pulse the current curves do not show significant deviations amongst each other. However, the main scattering of the measured curves takes place while the plasma pulse. The peak values of the current may be found in a spectrum between 9,03 kA and 9,83 kA.
By using the postprocessing methods described in chapter 4.1.3, the absorbed energy in the wire reps. wire plasma was able to be computed (Figure 4.6c). In this case the deviations are even less significant between the five repetitive experiments (2331,5 J -2374,6 J). The specific resistance diagram shown in Figure 4.6 (d) also represents a profound matching of the five datasets, which in turn confirms a good repeatability of the pulsed wire experiments investigated in this thesis.

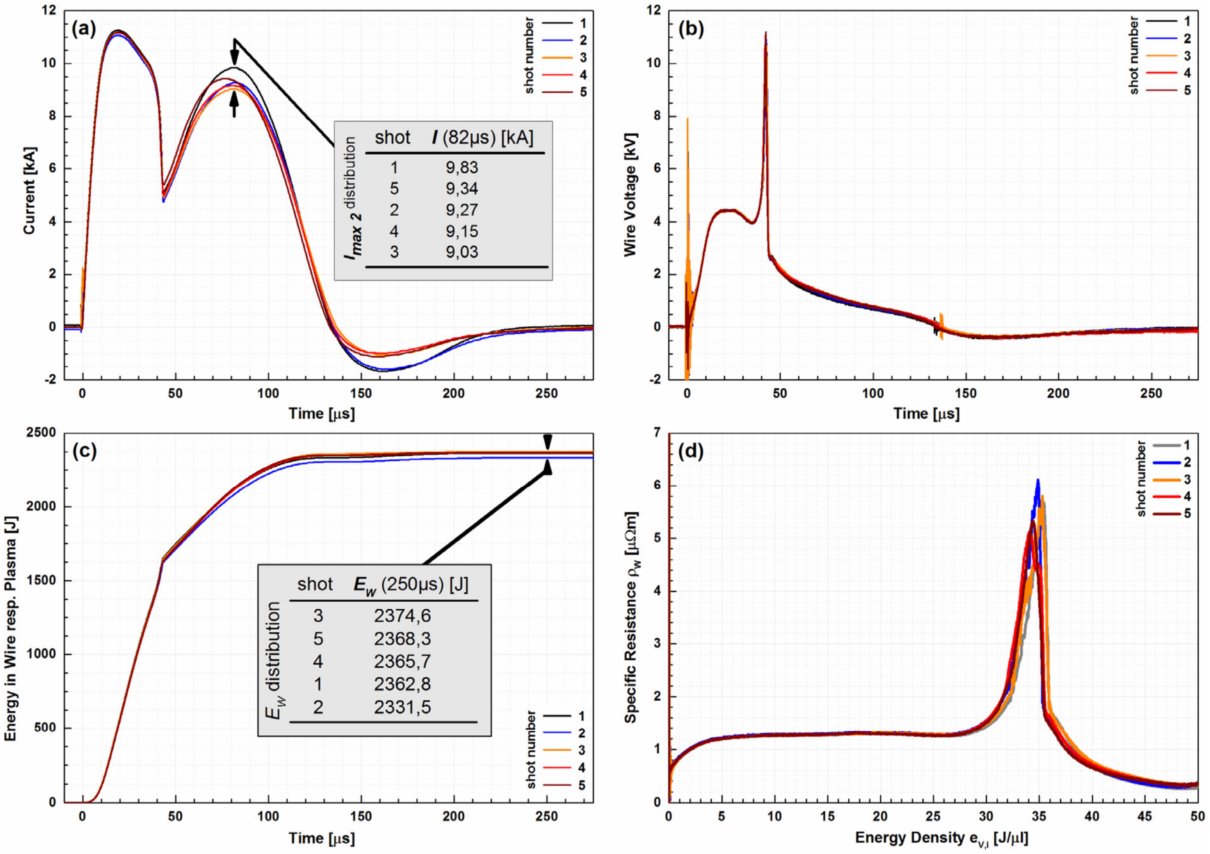

$I_{max\,2}$ distribution

shot	*I* (82µs) [kA]
1	9,83
5	9,34
2	9,27
4	9,15
3	9,03

E_w distribution

shot	E_w (250µs) [J]
3	2374,6
5	2368,3
4	2365,7
1	2362,8
2	2331,5

Figure 4.6: Repetitive experiments with constant parameters (a) Pulse Current, **(b)** Wire Voltage, **(c)** Absorbed Energy in Wire resp. Plasma **(d)** Specific Resistance Diagram; circuit parameters: C=150 µF, U_{C0}=6,00 kV, *L*=4,36 µH, X5CrNi18-10 wire, *l*=120 mm, *d*=700 µm

4.2 Results

4.2.1 Effect of capacitor charging voltage

Since the beginning of research on exploding wires in the 1960s, only a few scientists have analysed the influence of changing the initial capacitor voltage U_{C0}, while keeping all other parameters constant [31], [32]. These reports are focused on the analysis of the current and voltage paths during the discharges, however they do not present a systematic analysis of the absorbed energy within the wire or involved wire resistance. Therefore, the influence of capacitor voltage variations should be investigated in more detail within this thesis. In order to understand the influence of the initial capacitor voltage U_{C0} on the discharge behaviour, the involved capacitor energy E_{C0} was specified in equidistant steps (Table 4.1).

Capacitor voltage U_{C0}[kV]	4,42	4,76	5,10	5,42	5,71	6,00
Capacitor energy E_{C0} [kJ]	1,47	1,70	1,95	2,20	2,45	2,70

Table 4.1: Voltage and capacitor energy values

Hence the step size ΔE_{C0} between the capacitor energy values is 250 J (except for the first step), starting with 1450 J at a given capacitor voltage of U_{C0} =4420 V. The correlating initial capacitor voltages are computed by

$$U_{C0} = \sqrt{\frac{2E_{C0}}{C}} \tag{4.23}$$

with the constant capacitance value of C=150 µF. For all experiments the involved wire dimensions were set to a diameter of 700 µm at a length of 120 mm. The same wire dimensions were also choosen in the previous experiments in order to investigate the accuracy and repeatability of the experiments (chapter 4.1.4). However, this specific wire dimension was selected because of its characteristic double hill shape, where the current maximum of the plasma pulse is approximately 80 % of the current peak from the heat pulse. Figure 4.7 shows the pulse current (a) and wire voltage (b) depending on the specified initial capacitor voltages presented in table 4.1. All curves in Figure 4.7 (a) exhibit a characteristic shape of a double hill. The higher the initial capacitor voltage is set, the higher the peak current of the heat pulse is. For all initial capacitor voltages except 4,42 kV, the plasma pulse follows directly after the heat pulse. At t≈18 µs the current reaches its peak value for all initial capacitor voltages with a slight shift to t≈19 µs for higher initial capacitor voltages (U_{C0} =6,00 kV). In the case of U_{C0}=4,42 kV the plasma pulse does not directly follow after the heat pulse. Here the plasma pulse occurs 579 µs after the heat pulse, which represents a typical dark break [9]. In a more detailed view the peak values of the currents are in the spectrum between 8,86 kA (U_{C0}=4,42 kV) and 11,17 kA (U_{C0} =6,00 kV). The plasma pulse peaks are reached at 80 µs (9,16 kA) for U_{C0}=6,00 kV, at 90µs (7,39 kA) for U_{C0}=5,71 kV, at 93 µs (6,00 kA) for U_{C0}=5,42 kV, at 110 µs for U_{C0}=5,10 kV, at 135 µs for U_{C0}=4,76 kV, at 597 µs for U_{C0}=4,42 kV.

Figure 4.7 (b) shows the computed wire voltage after filtering and correction with equation (4.8). The measured voltages across the wire reach a first maximum after 21-24 µs. The peak values increase with higher initial capacitor voltage values U_{C0}. In the case of a capacitor voltage U_{C0}=4,42 kV, the first voltage peak reaches a value of U_w=3,30 kV.

At a capacitor voltage of U_{C0}=6,00 kV the first voltage peak lies at 4,44 kV. For all other intermediate values of capacitor voltage U_{C0}, the first peak values for the wire voltage $max_1[U_w]$ are nearly evenly distributed. During the pulse discharge, a lot of energy is stored in the magnetic field created by the current flow through the total inductance of the experimental circuit. After a sudden increase of the wire resistance, the inherent current of the circuit may not be stopped immediately. Therefore, the remaining flow of current will create a charge accumulation (negative as well as positive) at the endings of the wire. Since the contacts at the wire endings and the wire itself act as a capacitor with a small stray capacitance, the remaining flow of current will charge up this "wire capacitor". Due to its small capacitance value (some pF) the wire voltage U_w can reach values even far higher than the original capacitor voltage U_{C0} [33]. This effect may be seen within the inset of Figure 4.7b. Here the wire voltage U_w reaches higher values than the original capacitor voltage U_{C0} concerning all capacitor voltages $U_{C0} \geq$ 5,10 kV. Only for the capacitor voltages U_{C0}=4,42 kV and U_{C0}=4,47 kV the wire voltage U_w is lower. However, in the case of U_{C0} =4,42 kV the creation of a second local peak does not reach a voltage high enough to directly induce a plasma pulse event. Therefore, the wire voltage stays constant for U_{C0} =4,42 kV within the time interval of [50; 530] µs. Then after 530 µs the voltage decreases in a more or less linear fashion down to zero (670 µs). During the research activities of the fifties and sixties one investigated the length of the so called dark break in more detail [34]. By using the equation (4.11) the power in the wire resp. wire plasma is able to be computed and plotted in a graph (Figure 4.8a). As mentioned before, the first peak values for the pulse current I and wire voltage U_w are located in an interval $t(I_{max1})$=[18; 19] µs together with $t(U_{wmax1})$=[21; 24] µs. By viewing the power curves in more detail (inset of Figure 4.8a) the first peak values of all curves may be found at 20 µs. The first power peak has the highest value of all curves given at a capacitor voltage of U_C=6,00 kV, where it reaches a value of 49,5 MW. In the case of a capacitor voltage of U_C=4,42 kV, the first power peak reaches 28,5 MW. For the capacitor voltages U_{C0} =[4,76 kV, 5,10 kV, 5,42 kV, 5,71 kV] the values of the first power peaks are: $max_1(P_w)$=[32,6 MW, 37,2 MW, 41,3 MW, 45,6 MW]. After a local minimum, the power curves show a second power maximum in the form of a spike, which is located at totally different moments in time. The earliest power maximum, which also represents the total power maximum for all curves, may be found at 41,8 µs, where it reaches a value of 77,3 MW. All other second power peaks follow at much later points in time [45 µs, 49 µs, 55 µs]. Regarding the experiments with U_{C0}=4,42 kV and U_{C0}=4,76 kV the second power peak reaches values, that are less than 50% of the first power peak. However, these power curves may be numerically integrated by using equation (4.12). Figure 4.8 (b) presents the results of numerical integration concerning the curves from Figure 4.8 (a). In the first 20 µs all curves show a very straight increase regarding the absorbed energy within the wire. In this case, the slope is steeper the higher the initial capacitor voltage U_{C0} is. At a certain point each curve (except the curve for U_{C0}=4,42 kV) shows a significant bend (t_{bend}). When comparing the timing of these bends with Figure 4.7 (a), one notices that these time values fit together with the timing of the local minima from the current curves. This is the exact moment, when the plasma pulse occurs. From then on, the energy is not only absorbed by the wire itself but by the wire and wire plasma combined. After the first power peak, the power in the wire respectively wire plasma decreases rapidly, so that the curves of the absorbed energy increase slower than before.

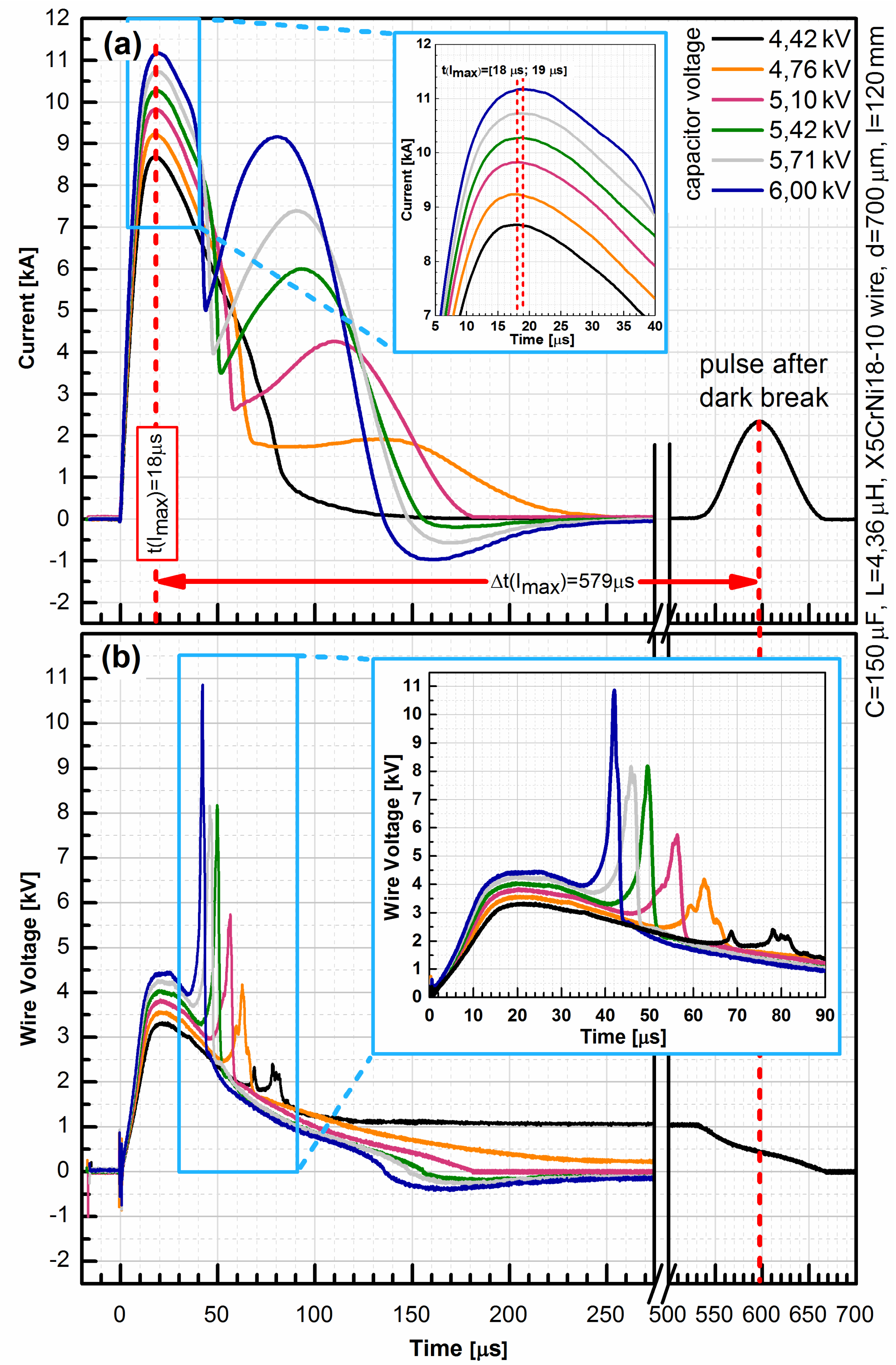

Figure 4.7: Discharge behaviour for different capacitor voltages U_{C0}
(a) Discharge Current **(b)** Wire Voltage

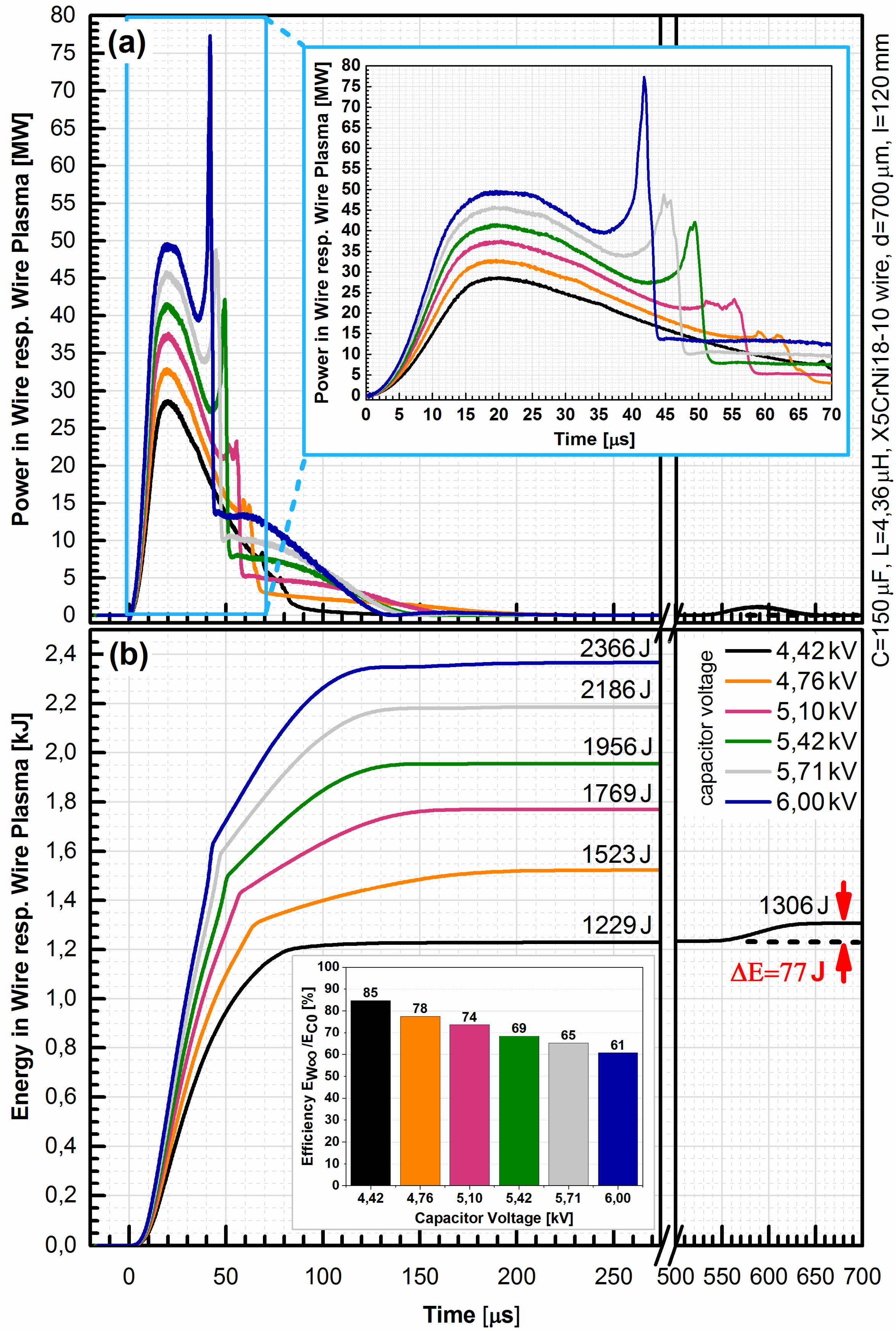

Figure 4.8: Discharge behaviour for different capacitor voltages U_{C0}
(a) Power in Wire resp. Wire Plasma **(b)** Energy in Wire resp. Wire Plasma

Actually, in a first approximation after the bends the curvature of the energy absorption within the wire plasma is negative:

$$\frac{d^2E_W(t)}{dt^2} < 0 \qquad for \quad t > t_{bend} \tag{4.24}$$

Mathematically speaking this means that the values for the absorbed energy converge towards a fixed value $E_{w\infty}$. This also becomes more obvious by expressing the derivatives as:

$$\frac{d^2E_W(t)}{dt^2} = \frac{dP_W(t)}{dt} < 0 \tag{4.25}$$

This means that the power curve which decreases, is responsible for the asymptotic behaviour of the curves from the absorbed energy within the wire plasma. However, the final values in regard to the absorbed energies are distributed between 2366 J (U_{C0}=6,00 kV) and 1306 J (U_{C0}=4,42 kV) (Figure 4.9). When placing these values in relation to the initially stored energy within the capacitors E_{C0} one is able to compute the efficiency η of the absorbed energy within the wire:

$$\eta = \frac{E_{W\infty}}{E_{C0}} \tag{4.26}$$

The attained values concerning the efficiency are shown in the inset within Figure 4.8 (b). By increasing the values of the capacitor voltage U_{C0} the efficiency decreases starting at η=0,85 for U_{C0}=4,42 kV. At an initial capacitor voltage of U_{C0}=6,00 kV the efficiency η lies at only 0,61.

By analysing the location of the bends in Figure 4.8 (b) one finds the amount of absorbed energy within the heat pulses (Figure 4.9). These values are significantly different from one another, and show the tendency of the absorbed energy within the heat pulse (view italic bars). At an initial capacitor voltage of U_{C0}=6,00 kV the heat pulse energy lies at 1639 J, which is about 69% of the total absorbed energy, which is 2366 J. Compared to the heat pulse energy of 1229 J, which occurs at an initial capacitor voltage of U_{C0}=4,42 kV, the heat pulse in this case lies at 94% of the total absorbed energy, which is 1306 J (view the black bars). However, the heat pulse energy seems to increase far less when one increases the initial capacitor voltage U_{C0} in comparison to the total absorbed energy. So, for higher initial capacitor voltages U_{C0} the fraction of $E_{pp}/E_{w\infty}$ increases progressively.

By numerical evaluation one is finally able to compute the specific resistance characteristic for the performed experiments. As shown in Figure 4.10 the energy densities within the interval [0; 23] J/µl overlap quite perfectly. Concerning higher energy densities (23 J/µl<$e_{V,i}$), the given curves differ from one another. The higher the initial capacitor voltage U_{C0} is, the earlier the specific resistance starts to increase. Regarding an initial capacitor voltage of U_{C0}=4,42 kV the specific resistance diverges towards a very high value (*A*) of nearly 500 µΩm. For the same curve the specific resistance decreases rapidly at 26,6 J/µl<$e_{V,i}$, this represents the pulse event starting at 530 µs after the dark break, which itself takes 579 µs (Figure 4.7). For the experiments without a dark break, the maxima in regards to the specific resistance is discoverable at energy densities (points *B*, *C*, *D*, *E* in Figure 4.10), which are able to be fitted by an parabolic equation:

$$\rho_W(e_{V,i}) = 69{,}75 + 4{,}705e_{V,i} - 0{,}0736e_{V,i}^2 \tag{4.27}$$

Here the values for $e_{V,i}$ must be expressed in J/µl, in order to attain the values of the specific resistance in µΩm.

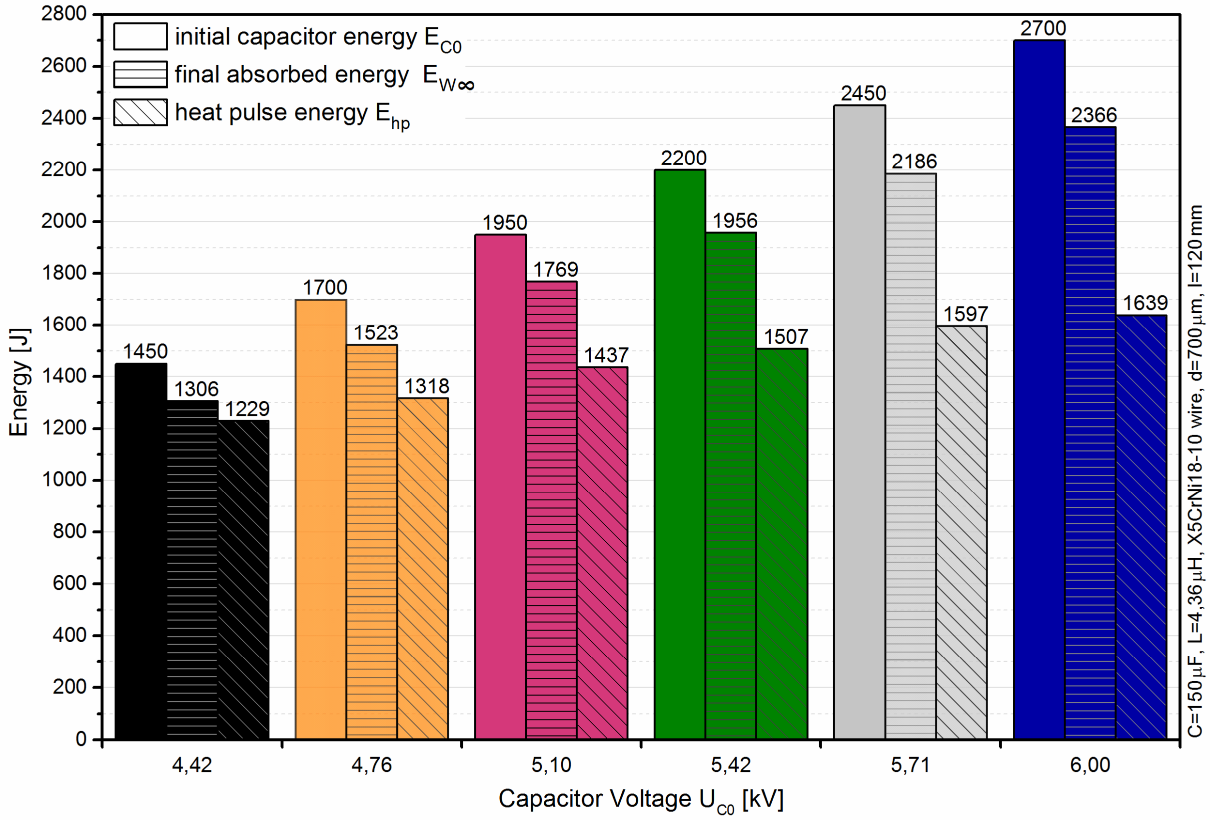

Figure 4.9: Energy diagram for different capacitor voltages U_{C0}

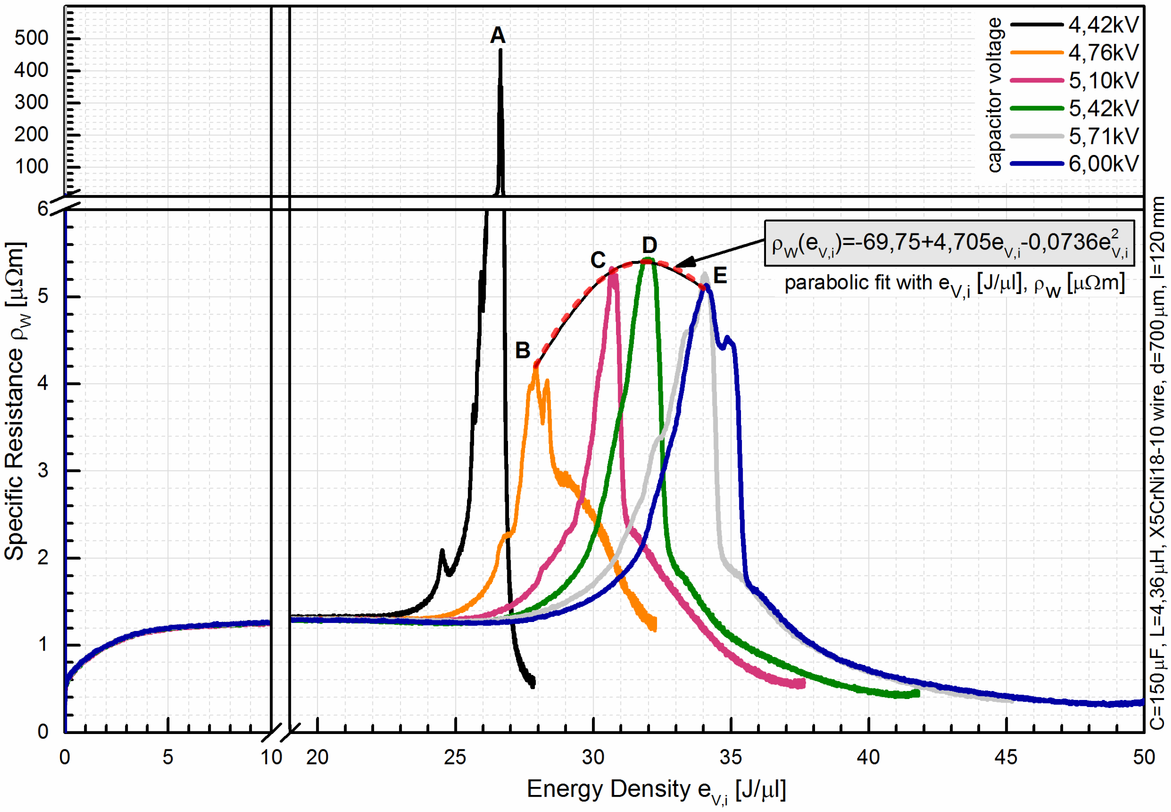

Figure 4.10: Specific resistance depending on energy density for different capacitor voltages U_{C0}

4.2.2 Effect of Wire Length and Diameter

4.2.2.1 Wire Dimensioning and Sublimation Energy

Within this chapter the influence of wire dimensions (length l and diameter d) on discharge behaviour will be investigated. The required *sublimation energy for a total vaporization* W_{sub}, which depends on the given wire length l and radius r, is easily computed by:

$$W_{sub} = \Delta H_{sub} r^2 \pi l \tag{4.28}$$

So, for a given wire volume with equal sublimation enthalpy, one may use long and thin wires on the one hand, or short and thick wires on the other hand. However, the choice of wire dimension will have an influence on the involved field strength $\mathcal{E}_W$ and the surface of the wire. Figure 4.11 shows the wire volume V dependant on the wire length l as well as the wire diameter d=2r. The experiments within this chapter have been performed with the wire diameters d equals 600 µm, 700 µm and 800 µm. The wire length implemented varies within a spectrum between l=[20; 180] mm. All experiments were completed with fixed circuit parameters (C=150 µF, U_{C0}=6,00 kV, L=4,36 µH), apart from the wire dimensions, so that the initial energy within the capacitance was 2700 J. When assuming a sublimation enthalpy of ΔH_{sub}=76 J/µl (chapter 4.1.1), it is possible to vaporize a volume V=2700 J/76 J/µl≈36 µl made of the steel alloy *X5CrNi18-10*. This corresponds to a wire mass of 284 mg (colour scale given in Figure 4.11). The performed experiments are able to be separated into the wire dimensions where E_{C0}>W_{sub} and the wire dimensions where E_{C0}<W_{sub}. In Figure 4.11 the grey dotted line separates both areas. So in this chapter the wire dimensions were specifically choosen in order to make 11 experiments fulfil the condition E_{C0}>W_{sub} as well as another 12 experiments fulfil the condition E_{C0}<W_{sub}. However, all the experiments drawn as a blue circle in Figure 4.11 were successfully performed.

4.2.2.2 Analysis of Discharge, Wire Energy and Resistance

Figure 4.12 shows the discharge current of wires with d=600 µm (a), d=700 µm (c), d=800 µm (e) together with the measured wire voltages $U_w(t)$ for d=600 µm (b), d=700 µm (d), d=800 µm (f). The measured curves represent experiments performed with the wire lengths of 40 mm, 80 mm, 120 mm and 160 mm. By comparing the measured current curves with each other, one is able to determine the current values reached at the peak, which increase by decreasing the wire lengths. These peak values may either be part of the heat pulses (l=120 mm&700 µm (c), l=160 mm&700 µm (c), l=80 mm&800 µm (e), l=120 mm&800 µm (e), l=160 mm&800 µm (e)) or part of the second pulses resp. plasma pulses (d=600 µm (a), l=40 mm&700 µm (c), l=80 mm&700 µm (c), l=40mm&800µm (e)). In general, when one increases the wire diameter, then the local peak maxima of the heat pulses increases, while at the same time the local peak maxima of the plasma pulses decreases (Figure 4.12 a, c, e). The voltages measured across the wires $U_w(t)$ have the shape of a local peak maxima, followed by a local minima and a voltage spike (Figure 4.12 b, d, f), which is caused by the effects of induction (compare chapter 4.2.1). By increasing the wire lengths, the peak values of the first local wire voltage maxima increases as well. Furthermore, an increase of the wire diameter decreases the peak values of the first local minima from U_w. However, the highest voltage peaks are spikes which are reached with wire lengths of l=80 mm independent of their diameter.

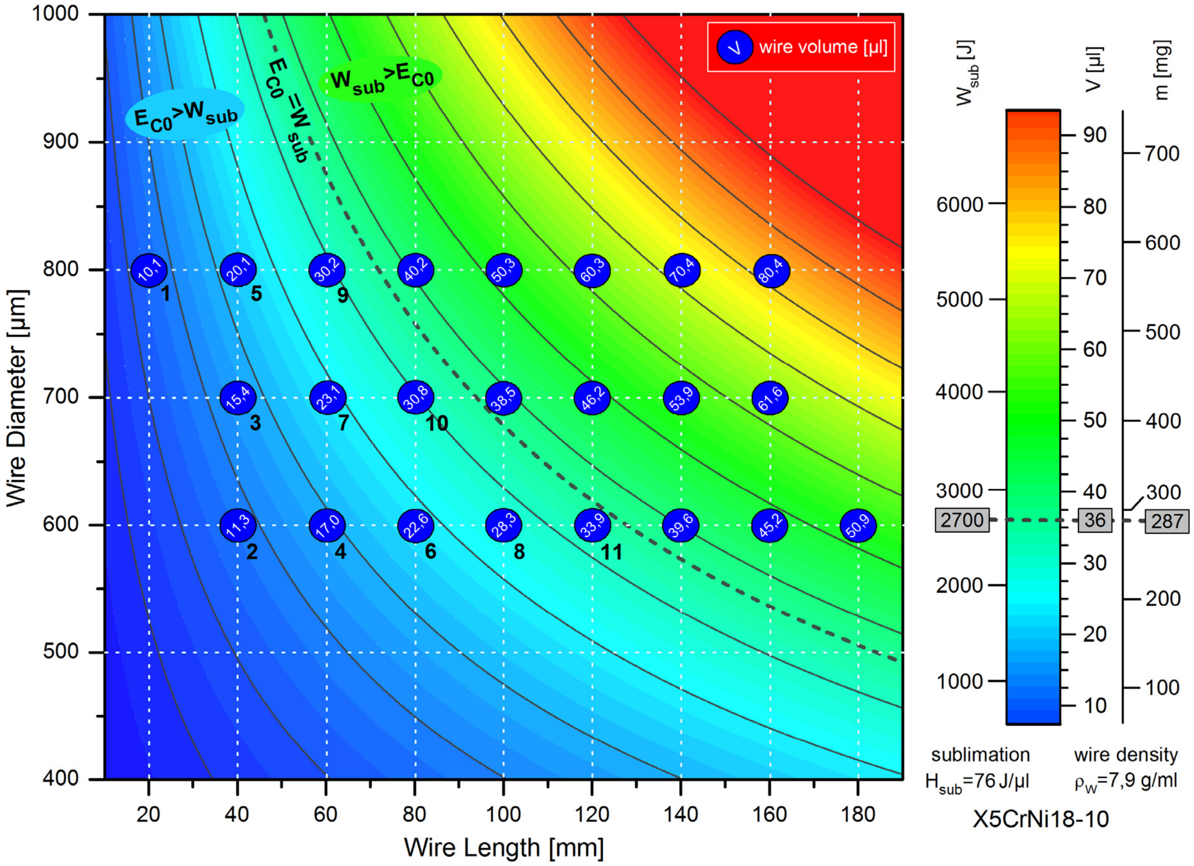

Figure 4.11: Wire volume and mass depending on wire dimensions. The color legend on the right indicates the corresponding wire mass (m) and required energy for sublimation (W_{sub}). The numbers next to the circles indicate the order of the wire volumes (V).

The wire power is shown in Figure 4.13 (a), (c), (e). These curves look similar to the wire voltage curves. After a local maxima peak, they all show a local minima followed by a spike. In general, the power peak values of the first maxima increase when one enlarges the wire diameter. The highest value of wire power may be found with wires of a length equalling 80 mm. This length of wire with a diameter of 700 µm allows one to reach a total power peak of 127,5 MW. By using equation (4.10) one is able to compute the time dependent wire resistance $R_W(t)$. The attained curves are plotted in Figure 4.13 (b), (d), (f). In the beginning the resistance values of the wire $R_W(t{\approx}0\mu s)$ quite perfectly fit to the initial resistance one receives when using equation (4.14). In this case the specific resistance is ρ_W(t=0)≈0,7 µΩm. Up to around 10µs all resistance curves grow in a nearly linear fashion and afterwards reach a plateau. Then all the curves show a characteristic spike, which correlates with the current and wire voltage curves (compare with Figure 4.12). Right after the spikes the wire resistance decreases rapidly due to the plasma discharge which has a low resistance [4].

The absorbed energy within the wire is shown in Figure 4.15 (a), (c), (e). These curves were computed by using equation (4.12) and show a nearly linear growth up to the bends (compare chapter 4.21). Then the curves of the wire energy approach asymptotically towards a specific end value $E_{W\infty}$. In general, longer wires show a steeper curve growth than shorter wires, therefore they also reach higher end values $E_{W\infty}$.

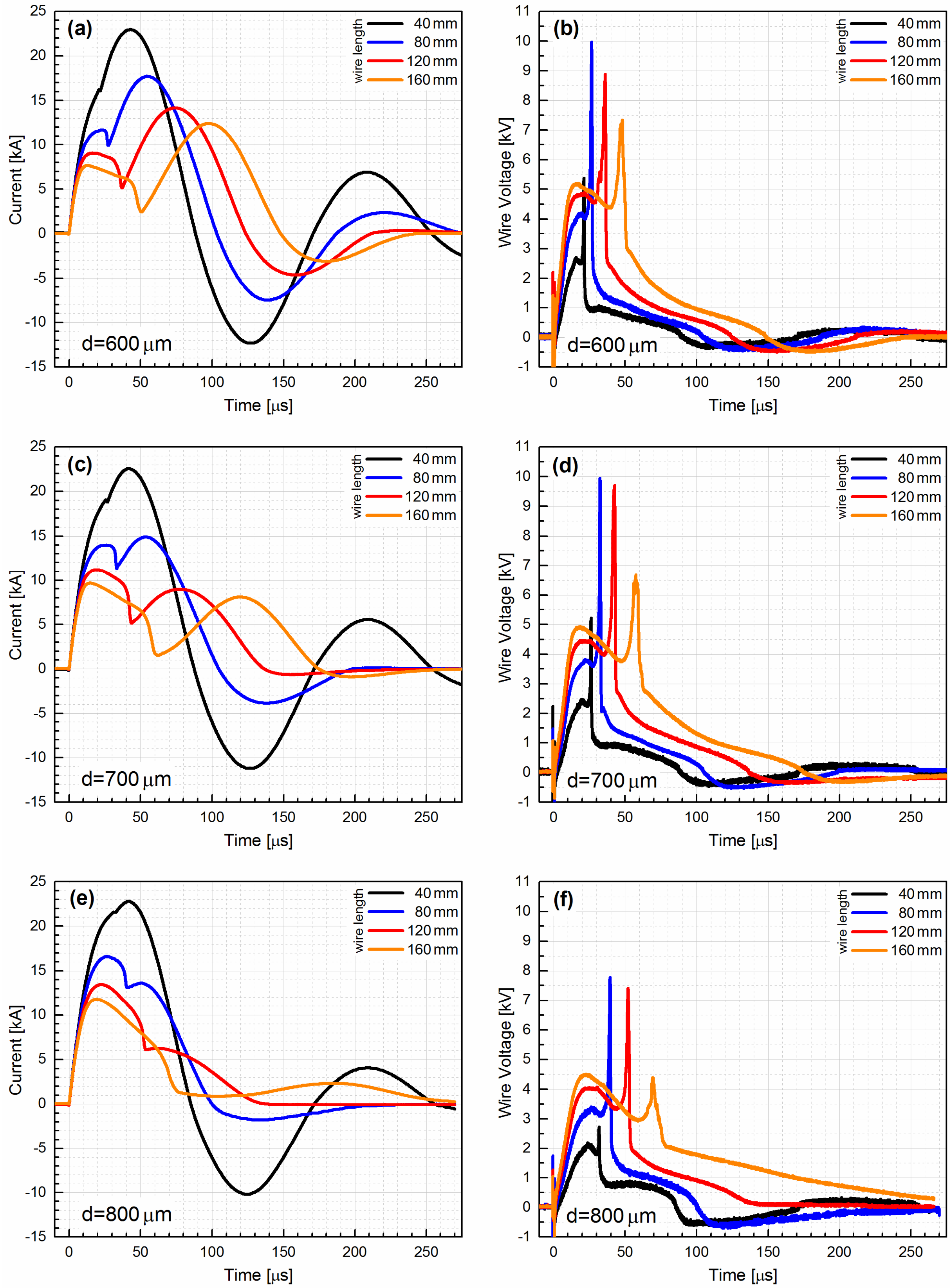

Figure 4.12: Discharge curves for different wire diameters and lengths
(C=150 µF, U_{C0}=6,00 kV, L=4,36 µH, X5CrNi18-10 wire)
wire with 600 µm diameter: (a) current, (b) wire voltage
wire with 700 µm diameter: (c) current, (d) wire voltage
wire with 800 µm diameter: (e) current, (f) wire voltage

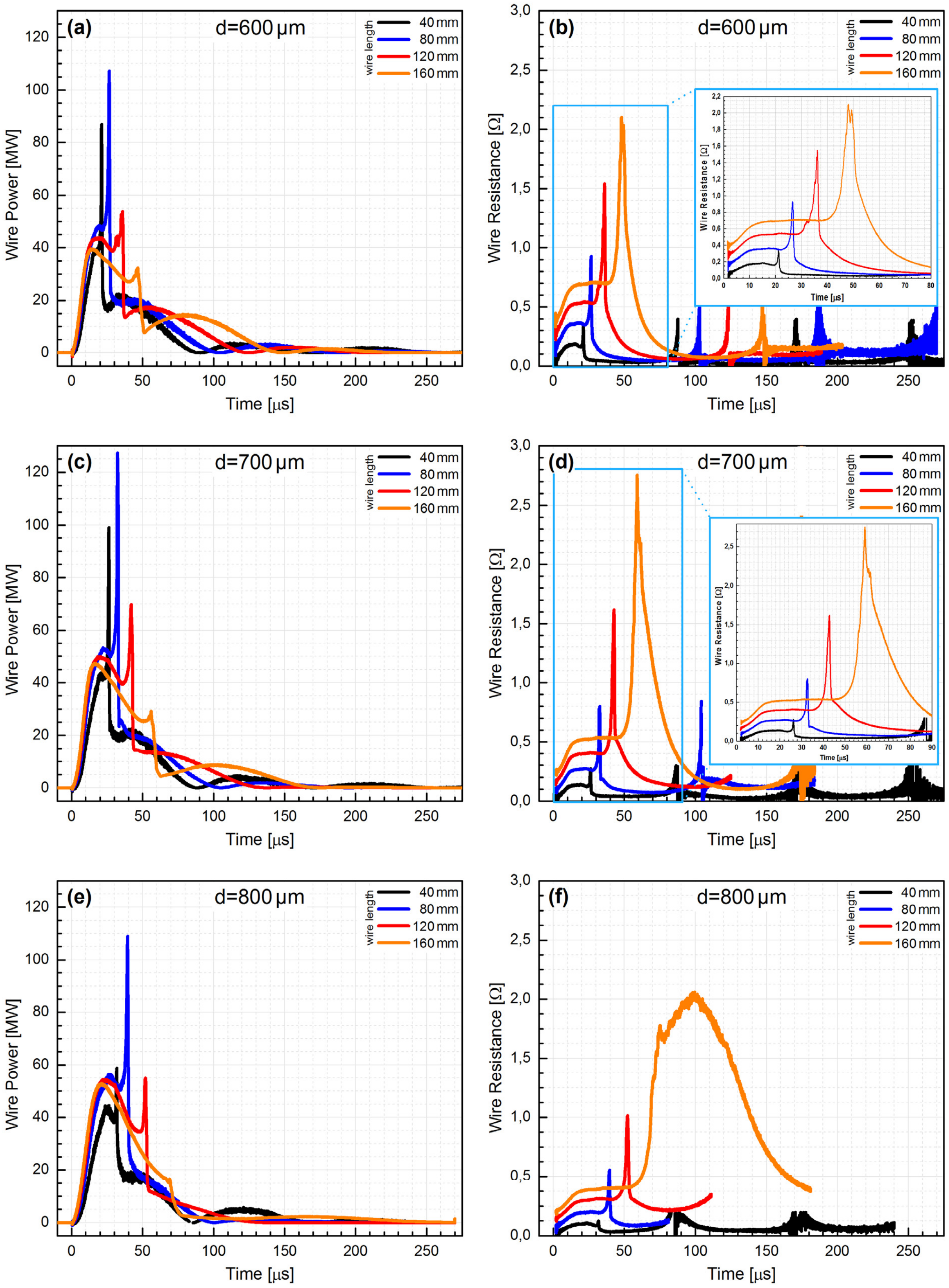

Figure 4.13: Wire Power and Resistance for different wire diameter and lengths
(C=150 µF, U_{C0}=6,00 kV, L=4,36 µH, X5CrNi18-10 wire)
wire with 600 µm diameter: (a) wire power, (b) wire resistance
wire with 700 µm diameter: (c) wire power, (d) wire resistance
wire with 800 µm diameter: (e) wire power, (f) wire resistance

The energy density $e_{V,i}(t)$ within the wire may be computed by using the equation (4.13) combined with the attained energy curves $E_w(t)$. The specific resistance values ρ_w may be gained by using the equation (4.14) together with the time dependent resistance curves $R_w(t)$. However, the values for the specific resistance ρ_w are able to be plotted against the energy density $e_{V,i}$ within the wire. The result offers an analysis of a time independent characteristic.

Figure 4.14 shows a scatter plot of all specific resistance data. Starting with values of $\rho_w \approx 0{,}65\,\mu\Omega\text{m}$ at $e_{V,i}=0\,\text{J}/\mu\text{l}$ the specific resistance begins to grow and finally reaches a value of $\rho_w \approx 1{,}27\,\mu\Omega\text{m}$ at $e_{V,i}=25{,}3\,\text{J}/\mu\text{l}$. In this interval [0; 25,3] J/µl the data may be fitted quite perfectly by the following fit curve:

$$\rho_W(e_{V,i}) = 1{,}27 - 0{,}617 \cdot 0{,}69^{e_{V,i}} \tag{4.29}$$

Only for data points where $25{,}3\,\text{J}/\mu\text{l} < e_{V,i}$ the resulting values of the specific resistance within the wire differ significantly from one to another depending on the used length and diameter of the wire. These specific characteristic curves are presented in Figure 4.15 (b), (d) and (f).

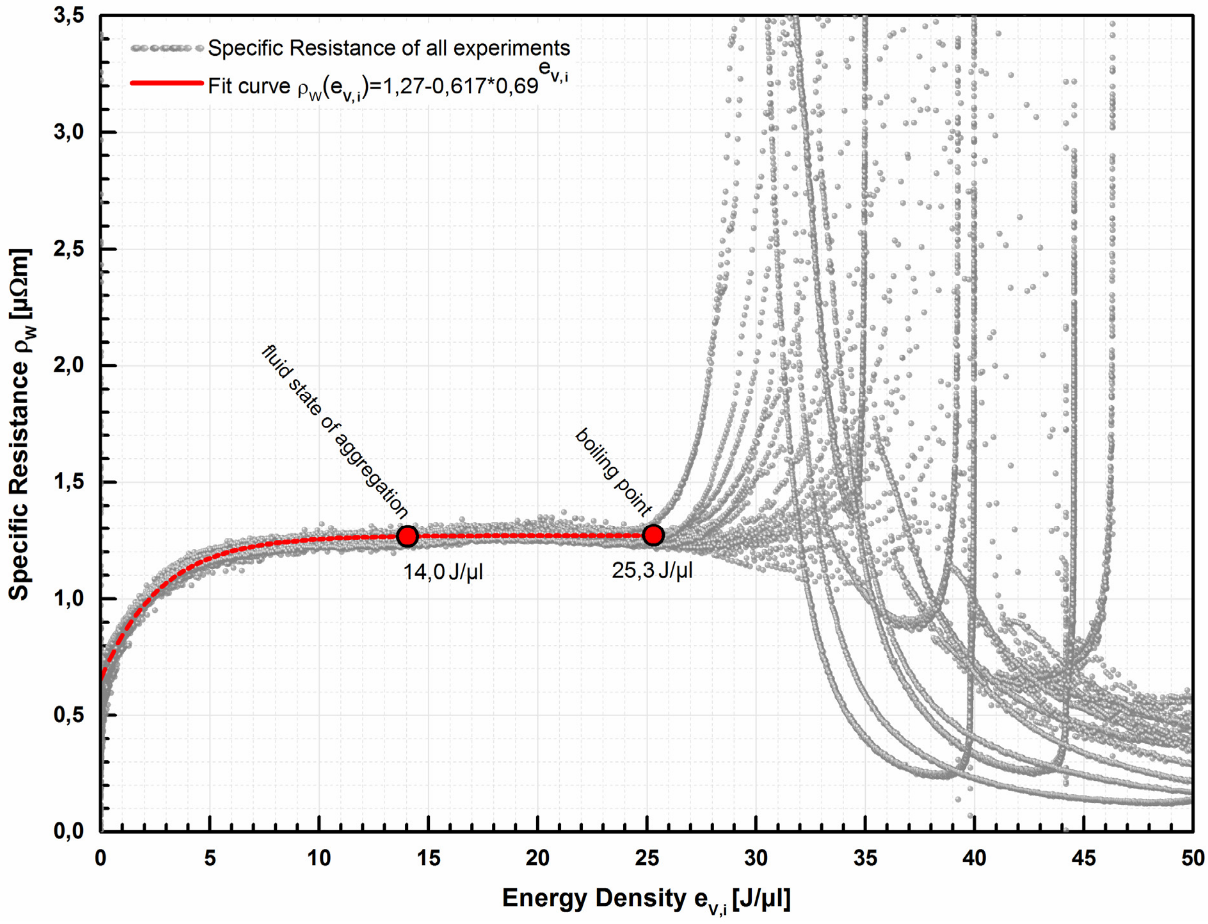

Figure 4.14: Specific Resistance Characteristic for all experiments from chapter 4.2.2. The fluid state of aggregation is reached at an energy density related to the initial volume of $e_{V,i}$=14,0 J/µl, the boiling point at an energy density related to the initial volume of $e_{V,i}$=25,3 J/µl (compare chapter 4.1.1, Fig. 4.1).

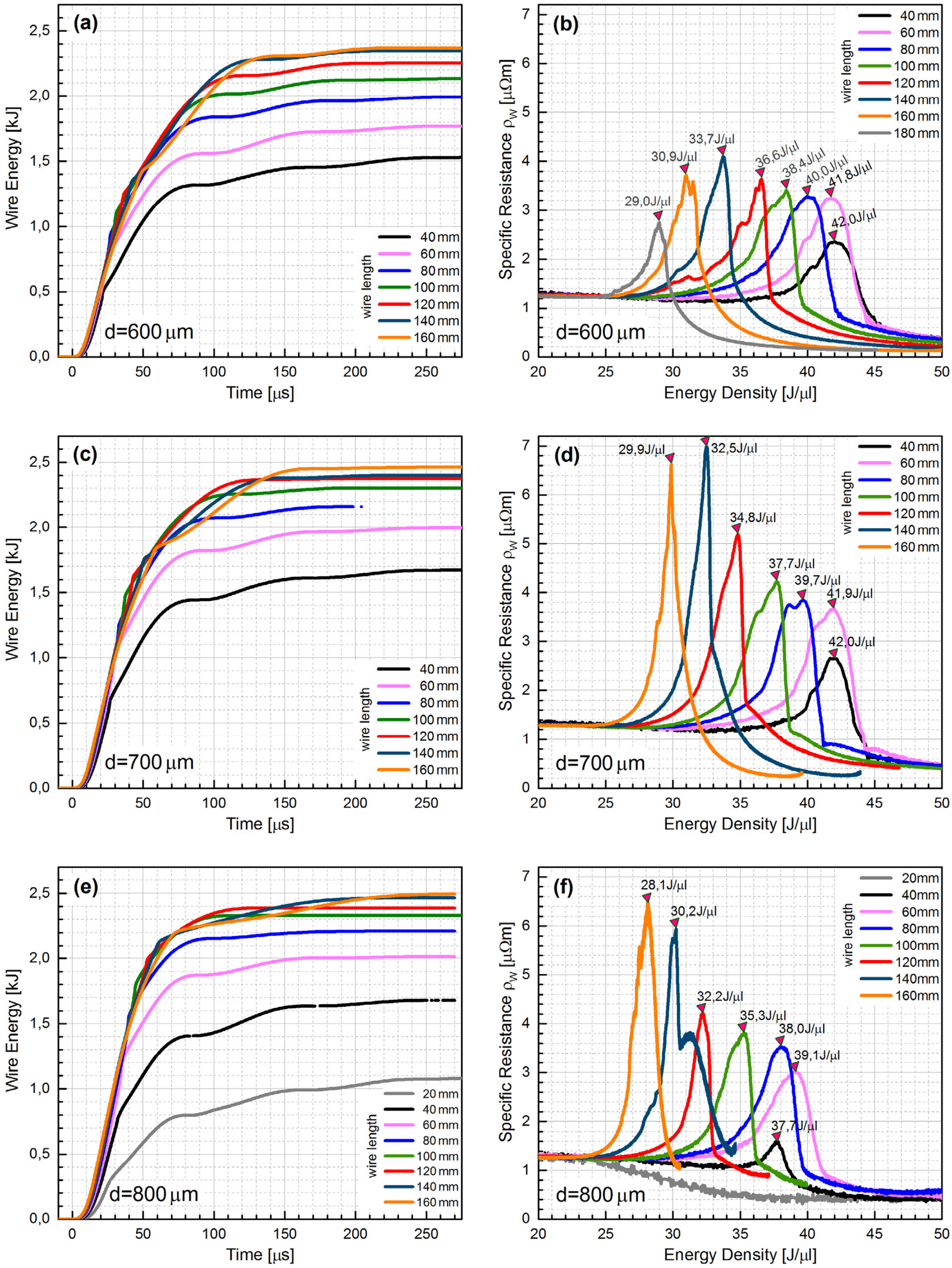

Figure 4.15: Wire Energy and Resistance Characteristic for different wire diameters and lengths
(C=150 µF, U_{C0}=6,00 kV, L=4,36 µH, X5CrNi18-10 wire)
wire with 600 µm diameter: (a) wire energy, (b) resistance characteristic
wire with 700 µm diameter: (c) wire energy, (d) resistance characteristic
wire with 800 µm diameter: (e) wire energy, (f) resistance characteristic

The maximum value of the specific resistance $\rho_w(e_{V,i})$, which is dependent on the used wire length, will be reached within a spectrum range of between $e_{V,i}$ = [28; 42] J/µl. The longer the used wire is, the earlier the specific resistance will reach its peak value. The correlation between energy input, maximum current density and specific resistance was also investigated by Tucker [35]. Reithel and Blackburn [31] explained the resistance anomaly via a "hydrodynamic model, in which it is assumed that the exploding wire is strongly contained by the inertia of its own material so that, as the current density in the wire is increased, the expansion of the wire is hindered in such a way that the electrical resistance of the exploding wire approximates that of a liquid long after an amount of energy capable of evaporating the wire at ambient pressures has been deposited in the wire." However, this explanation is not prooven as a real physical model, but never the less is considered within a newer publication [36], as a basis for numerical modelling.

4.2.2.3 Action Integral and absorbed Wire Energy

For each experiment presented within this chapter, the involved action $A(t)$ was able to be computed with equation (4.16). The final values were determined by the assumption that $A_\infty \approx A(t=250\mu s)$. Figure 4.16 shows the final action A_∞ in dependence of the used wire dimensions. According to chapter 2.2 the action $A_\infty(R)$ increases more highly, the lower the resistance within the *RLC* circuit is. However, this tendency is also noticeable by looking at the magnitude of action values during the performed experiments. The thinner and shorter the used wires are, the higher the final action value A_∞ becomes. Concerning the shortest and thinnest wires (l=40 mm, d=600 µm) their action reaches a value of up to $A_\infty \approx 32\, kA^2s$. In comparison, the action of the longest and thickest wire (l=160 mm, d=800 µm) is only about $6\, kA^2s$.

The energy finally absorbed within the wire respectively wire plasma is discoverable via the assumption $E_{W\infty} \approx E_W(t=250\mu s)$. By taking these values from Figure 4.15 (a), (c), (e) one is able to receive Figure 4.17. Hence the energy fraction which is absorbed within the wire during the heat pulses (*Energy Heat Pulse*, E_{hp}) is shown in red. The energy fraction absorbed during the plasma pulse is shown in blue (*Plasma Energy*, E_{pp}). By comparing the total sum of absorbed energy within the wire respectively wire plasma ($E_{W\infty} = E_{hp} + E_{pp}$), one is able to see that when one lengthens the wire $E_{W\infty}$ increases as well. Furthermore, the fraction $E_{hp}/E_{W\infty}$ also increases when one lengthens the wire, it reaches its highest value of 0,91 at a wire length of l=160 mm and d=800 µm. When comparing wires of the same length, but different diameters, one may see the following dependency:

Thicker wires (e.g. 800 µm) absorb more energy than thinner wires (e.g. 600 µm). At the same time with ticker wires the fraction $E_{hp}/E_{W\infty}$ is also higher compared to thinner wires. However, the described tendencies are correct concerning the investigated wire dimensions but are not necessarily accurate for other wire dimensions. So, for very thick and short wires one may assume that $E_{W\infty}$ will decrease again, because of it´s low resistance, which prevents an energy absorption within the wire. Furthermore the amount of energy absorbed while the heat pulses is exactly stacked in the order of the used wire volumes when $E_{C0} > W_{sub}$ counts (Figure 4.11).

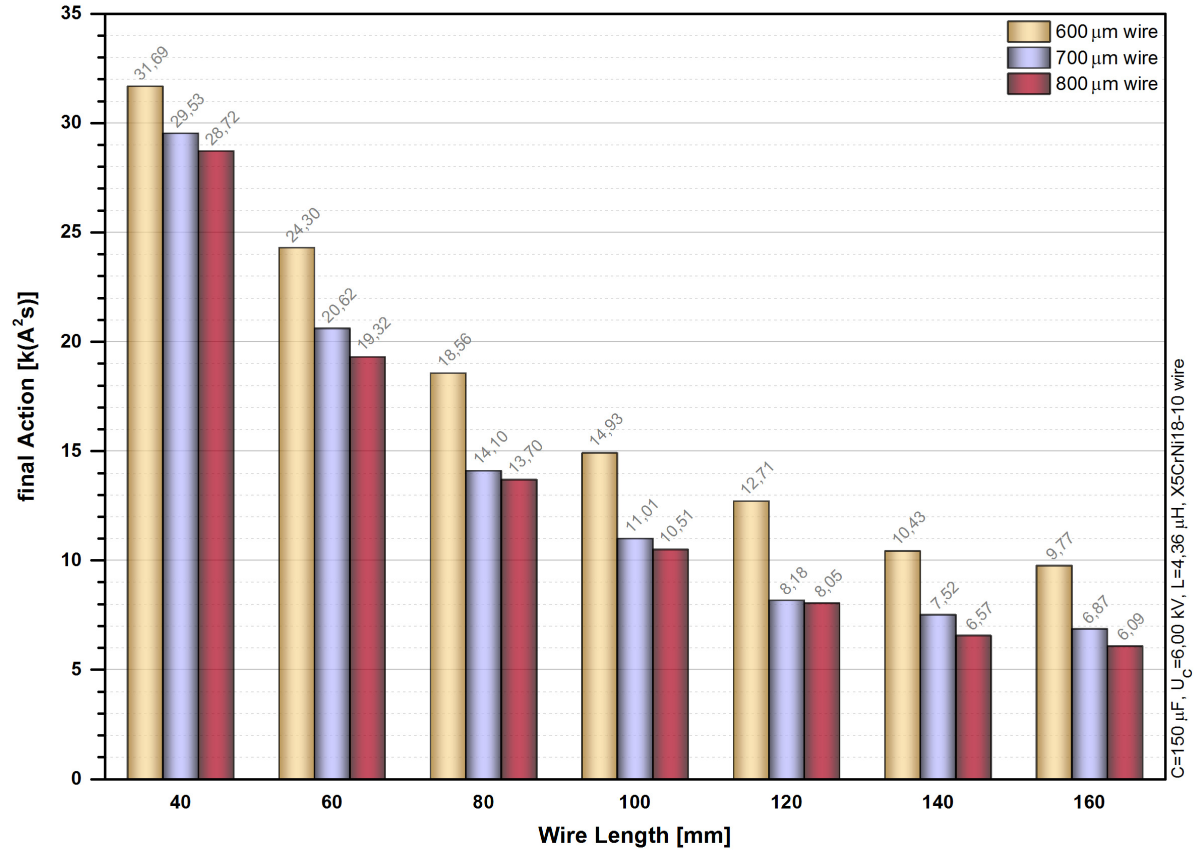

Figure 4.16: Final Action of the Pulsed Discharges (numerically integrated up to 250 µs)

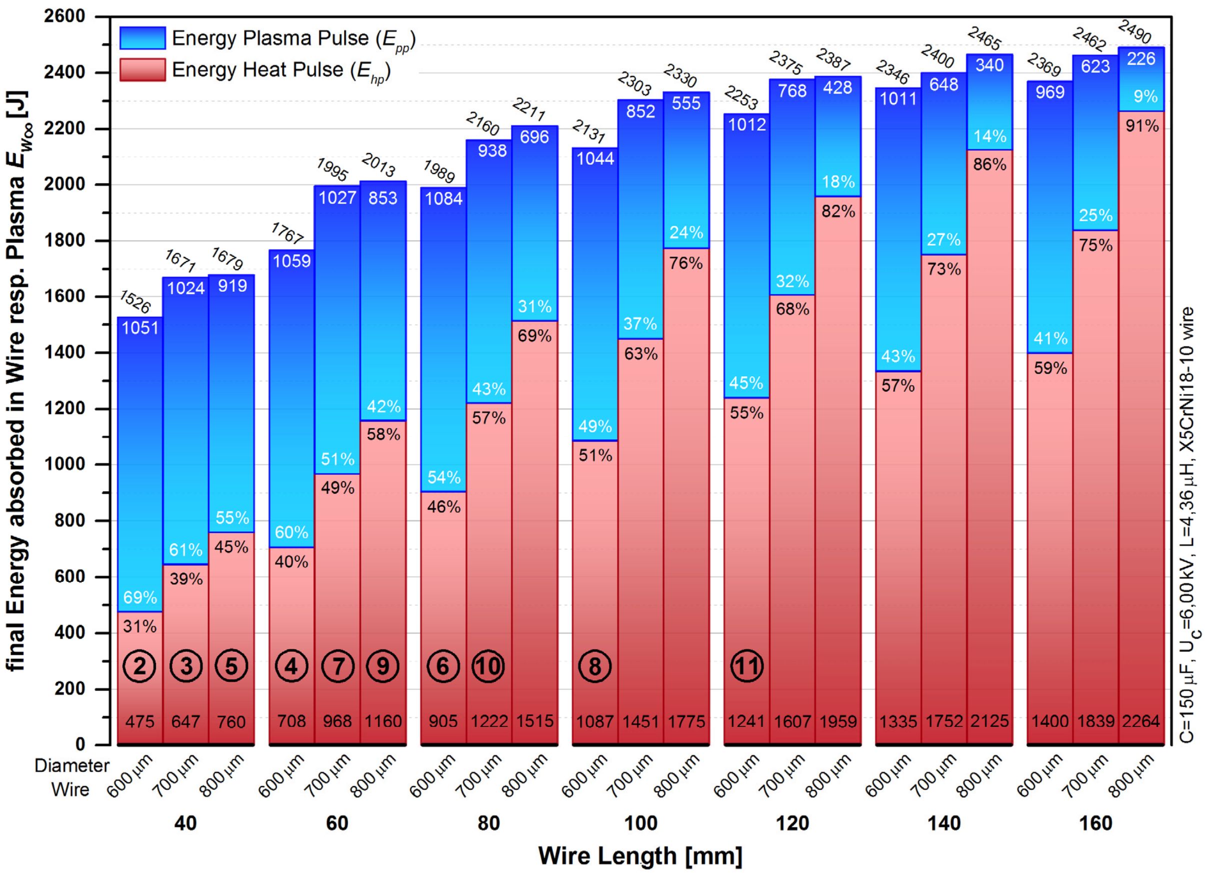

Figure 4.17: Final Energy absorbed in Wire resp. Plasma (numerically integrated up to 250 µs). The circled numbers represent the wire dimensions from Figure 4.11 when E_{C0}>W_{sub}.

4.2.2.4 Averaged Wire Resistance and Circuit Efficiency

The time averaged wire resistance during the experiments is able to be computed with the equation (4.17), when solved for R_i [37], [38]:

$$\overline{R}_W = \frac{E_{W\infty}}{A_\infty} = \frac{\int_0^\infty U_W(t) I(t) dt}{\int_0^\infty I^2(t) dt} \tag{4.30}$$

With the expression $E_{W\infty} = \overline{R}_W A_\infty$ one may further deduce the term for the total energy in the system, which is:

$$E_{sum} = E_{C0} = (\overline{R}_W + \overline{R}_{cir}) A_\infty \tag{4.31}$$

Since the efficiency of an exploding wire experiment is described by the quotient presented in equation (4.26), one is able to eliminate the involved action in order to determine

$$\eta = \frac{E_{W\infty}}{E_{sum}} = \frac{\overline{R}_W}{\overline{R}_W + \overline{R}_{cir}} \ . \tag{4.32}$$

Via numerical computation of equation (4.30), combined with the assumption that $E_{w\infty}$=E_w(t=250 µs) and A_∞=A(t=250 µs) one receives the numerical values for $E_{w\infty}$, A_∞ and $\overline{R}_W$. The results for these values in relation to the performed experiments, are presented in Table 4.2. Since a significant fraction of the total energy is also absorbed within the circuit resistance $\overline{R}_{cir}$, this value should be analysed for each experiment. However, $\overline{R}_{cir}$ is given by:

$$\overline{R}_{cir} = \frac{E_{sum} - E_{W\infty}}{A_\infty} \tag{4.33}$$

When one inputs the initial capacitor energy of E_{C0}=2700 J and the previously found values for $E_{w\infty}$ and A_∞, one receives the averaged circuit resistance $\overline{R}_{cir}$. The description "averaged" is used because of mathematical correctness and should not imply that the circuit resistance during the pulse discharges changes significantly. Due to the fact that the total conductor volume of the used supply lines is rather high (compare chapter 3.1), the circuit resistance should be rather constant throughout time. Even though, one may notice a slight change concerning the computed values $\overline{R}_{cir}$ presented in Table 4.2. However, the mean average of all values $\overline{R}_{cir}$ from Table 4.2 shows the value 36,4 mΩ with a standard deviation of 1,9 mΩ. By putting this value into equation (4.32) one is able to compute the efficiency curve $\eta(\overline{R}_W)$, which is shown in Figure 4.18. In the case of a wire resistance equal to the circuit resistance, $\overline{R}_W$=$\overline{R}_{cir}$=36,4 mΩ, one half of the initially stored energy from the capacitance would be absorbed by the supply lines, while the other half of the energy would be absorbed by the exploding wire (red dot). The coloured triangles in Figure 4.18 exhibit the operation points of the performed experiments, whereby the numbers next to the triangles show the used wire lengths in [mm]. All things considered, the efficiency η grows when one increases the wire length l or diameter d. When remembering the resistance, which would be needed for a critical damping, R_{cd} ≈341 mΩ (chapter 2.2), one may compute the needed wire resistance as: $\overline{R}_W$=R_{cd}- $\overline{R}_{cir}$= 341 mΩ-36,4 mΩ≈305 mΩ. The wire, which is the closest to $\overline{R}_W$=305 mΩ, is the wire with a length of 120 mm at a diameter of 800 µm.

wire diameter [µm]		wire length [mm]						
		40	60	80	100	120	140	160
600	$E_{w\infty}$	1526	1767	1989	2131	2253	2346	2369
	A_∞	31688	24295	18563	14926	12707	10431	9771
	$\overline{R}_W$	48	73	107,1	142,8	177,3	224,9	242,5
	$\overline{R}_{cir}$	37,0	38,4	38,3	38,1	35,2	33,9	33,9
700	$E_{w\infty}$	1671	1995	2160	2303	2375	2400	2462
	A_∞	29530	20619	14103	11005	8179	7522	6868
	$\overline{R}_W$	56,6	96,8	153,2	209,3	290,4	319,1	358,5
	$\overline{R}_{cir}$	34,8	34,2	38,2	36,1	39,7	39,9	34,7
800	$E_{w\infty}$	1679	2013	2211	2330	2387	2465	2490
	A_∞	28725	19316	13699	10508	8052	6571	6090
	$\overline{R}_W$	58,5	104,2	161,4	221,7	296,4	375,1	408,9
	$\overline{R}_{cir}$	35,5	35,6	35,7	35,2	38,9	35,8	34,5

Table 4.2: Tabular data of circuit and wire resistance: Finally absorbed energy within the wire $E_{w\infty}$ [J], final action values A_∞ $[A^2 s]$, averaged wire resistance $\overline{R}_W$[mΩ], averaged circuit resistance $\overline{R}_{cir}$[mΩ]. Assumptions combined with equation (4.30-4.33) are: $E_{w\infty}$=E_w(t=250 µs), A_∞=A(t=250 µs)

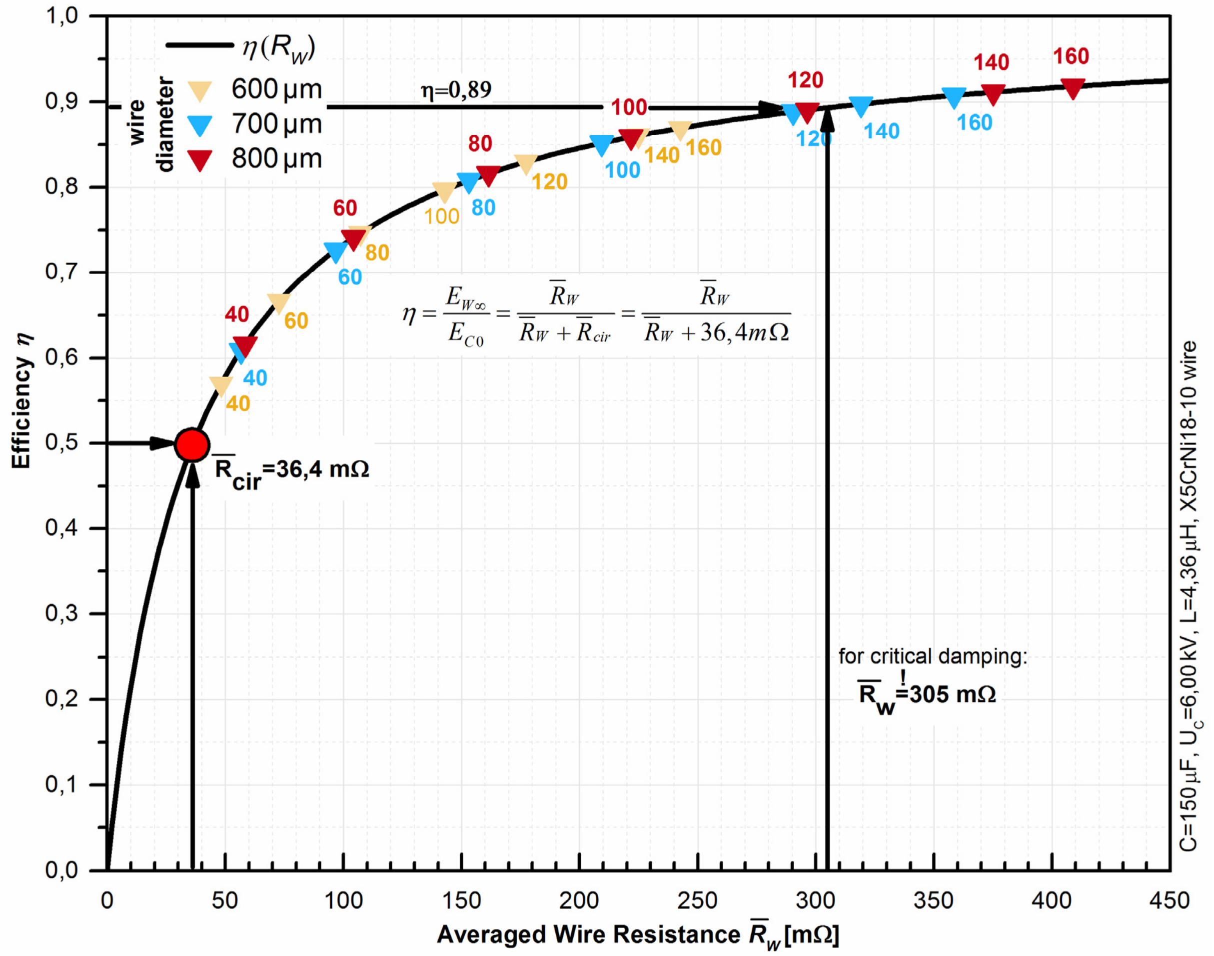

Figure 4.18: Efficiency graph. The triangles represent the wire diameters 600 µm, 700 µm and 800 µm, while the numbers next to the triangles indicate the wire lengths in [mm].

5. Design of a simulation model

5.1 Motivation

Since the performed experiments within this thesis show many correlating quantities (e.g. $I(t)$, $U_W(t)$, $P_W(t)$, $R_W(t)$, $E_W(t)$ etc.), a detailed understanding and interpretation of their interconnections is an exciting challenge. The understanding of the attained resistance characteristic $\rho_W(e_{V,i})$ curves and their correlations with the time dependent quantities $I(t)$, $U_W(t)$, $P_W(t)$, $E_W(t)$ may help to improve further experiments and optimisations. So far almost no effort has been made by researchers in the field of exploding wires in order to show a vivid depiction of the involved quantities. This part of the thesis outlines the development of a usable software tool, which enables the simulation of pulsed wire discharges and its main correlating quantities.

From the outset, the goal was to programme a software with a graphical user interface, which is easy to use. Furthermore, it should allow one to perform fast experiment computations (t<60s) on a laptop with contemporary performance capabilities (Core i5, 8 GB DDR4-RAM). If required, the accuracy of the computations should also be adjustable by changing the solving methods as well as numerical step sizes. In order to compare the results of the simulations with real experiments, one should also be able to import experimental data. As an additional benefit, the software should allow the computation of solutions regarding time dependent resistance curves from the wire $R_W(t)$, which don´t exhibit strong deflections caused by divergence effects (compare spikes in Figure 4.13 (b) for 70 µs<t).

In the past, several approaches were carried out in order to find usable methods which allow the simulation of exploding wire experiments. Tucker and Toth [30] tried to find analytical solutions, which describe the resistance of the wire through exponential functions. The applied methods allowed the computation of experiments, but were restricted by the implemented mathematical approach, which did not enable the definition of a resistance characteristic in various ways. By using the WKB[5] method, Good [39] assumed that the variation of $R_W(t)$ is minor with respect to itself and takes place within a short time period compared to the basic period of oscillation. Some modern publications try to simulate the behaviour of exploding wires via numerical computation of the *magnetohydrodynamic* (MHD) equations [40]. However, these approaches need profound data sets in regard to the material properties (density, heat capacity, resistivity etc.) within a wide spectrum range, which are not known or hard to obtain [40]. Moreover, plasma instabilities complicate the simulations concerning the already very time-consuming computations [41]. Instead of using *Pspice*, as Hogg [42] et al. used for dynamic sparc simulations, within this thesis a semi physical model with direct knowledge of the differential equations should be conceived.

---

[5] The WKB method is a method for finding approximate solutions of the one-dimensional stationary Schrödinger equation. It takes its name from the phycicists Gregor Wentzel, Hendrik Anthony Kramers und Léon Brillouin.

5.2 Model assumptions

According to Lindskog and Ljung [43] a semi physical model is "an application of system identification, where physical insight into the application is used to come up with suitable nonlinear transformations of the raw measurements, so as to allow for a good model structure". Applied to the modelling here, several assumptions had to be made in order to derive a usable system of differential equations, which describes exploding wire circuits:

(1) Capacitance C
First of all, the used capacitors within the experiments had to be approximated as one capacitance *C*. This assumption is possible as long as the inductance of the wires, which interconnects the individual capacitors, is small compared to the total inductance of the circuit. Regarding the experimental setup implemented within this thesis, the assumption of one capacitance *C* was also able to be proven by simulations with *PSpice* (compare chapter 3.1).

(2) Sparc gap resistance
Another assumption is the neglection of the spark gap resistance R_{SG}. By using the *Toeplers spark gap law* [44] one is able to easily determine the involved resistance, which is approximately 18 µΩ[6] concerning the spark gap, which in turn is around 1/2000 of the circuit resistance (R_{cir} ≈36 mΩ).

(3) Circuit resistance
During the experiments the supply lines of the circuit, with a total circuit resistance R_{cir}, are assumed to be constant. This means that no substantial heat will cause a significant increase of R_{cir}, even though up to 43% of the initially stored energy within the capacitors is able to be absorbed in R_{cir} (compare Figure 4.18).

(4) Mechanical deformation of coaxial cables
Since the volume between the inner and outer conductor within a coaxial cable is pretty small, the *Poynting flux* [45] resp. power density of the electromagnetic field (when 10 kA<*I*) is pretty high. The magnetic component is responsible for quite a strong magnetic pressure, which is equal to the energy density of the magnetic field[7]. However, the pressure acts against the other conductor of the coaxial cable and may create a small radial outward movement within the sleeves. This mechanical stress may result in a deformation, which in turn will absorb energy from the experimental circuit. Regarding the dimensions of the used experimental setup in combination with the RG164U coaxial cable, this energy loss should be assumed as negligible.

---

[6] According to [44] Toepler's spark gap law allows to compute the averaged resistance of a spark gap: $\bar{R}_{sg} = kF/Q$, where *k* [ΩC/cm] is the spark constant, *F* the spark gap distance [cm] and *Q* [C] the total charge, which flows through the spark gap. With *k*=0,08· $10^{-3}\Omega\mathrm{C/cm}$, *F*=0,2 cm and *Q*=0,9 C the averaged spark gap resistance becomes approximately 18 µΩ.

[7] $e_m = \frac{\vec{B}^2}{2\mu_0} = p_m$, where e_m is the magnetic energy density [J/m^3], $\vec{B}$ the magnetic flux density vector, μ_0 the vacuum permeability and p_m the magnetic pressure [N/m^2].

(5) Stray capacitances

Stray capacitances between the supply lines are also assumed to be negligible. This is able to be done because of to the low values from the stray capacitances (C<1000 pF), since the capacitance of the capacitor bank (C=150 µF) is more than 150000 times larger. When building a simulation model, the disregard of the stray capacitances has no significant influence.

(6) Specific Resistance and energy density

As described in chapter 4.1.3, the resistance of the wire is a quantity, which may be attained through equation (4.10). Since the curves of the wire resistance $R_W(t)$ do strongly depend on the used wire dimensions (r, l), a more general quantity to describe the material properties is the specific resistance gained by equation (4.14). In real, the dimensions of the wire are not constant during the heating and vaporization process (e.g. wire radius increases). Therefore, within the modeling here, the wire should be viewed as a special material which retains its dimensions during the pulse discharges (Figure 5.1). This *isochoric assumption* furthermore implies, that the energy density within the wire is able to be computed by the equation (4.13). Clearly, one is able to view the expression $e_{V,i}$ as the energy E_W, which is inserted into the initial volume V_i. Bearing this in mind, an expansion of the real volume $V(t)$ is not important. By describing the specific resistance dependent on the inherent energy density within the wire, one receives the expression $\rho_W(e_{V,i})$, which assumes a homogenous distribution of energy density and specific resistance.

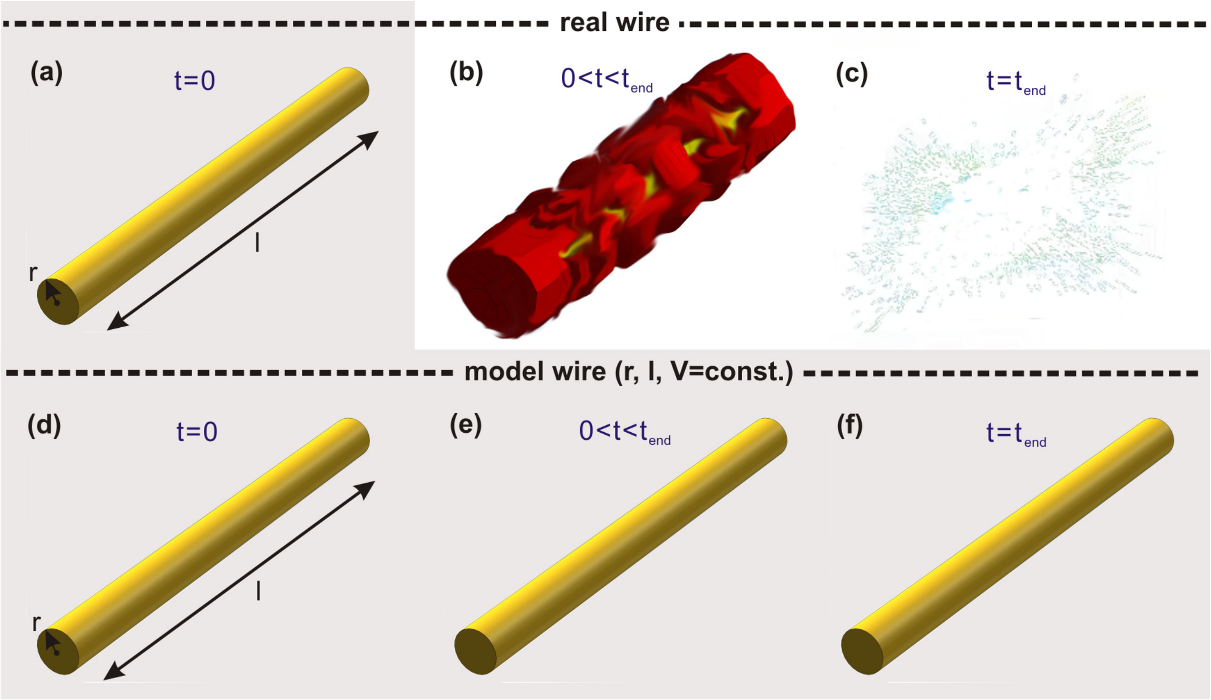

Figure 5.1: Modelling of the specific resistance and energy density regarding the used wire material. **(a)**, **(b)** and **(c)** illustrate the actual heating and vaporisation behaviour, while **(d)**, **(e)** and **(f)** represent the assumption of constant wire dimensions (r, l, V) during the entire range of time. Within this modelling, the energy density $e_{V,i}$ and specific resistance ρ_w are both assumed to be homogenously distributed throughout the fictitious wire material.

5.3 Derivation of a coupled differential equation system

5.3.1 Parameterisation of resistivity depending on energy density

Together with the previous explained assumptions (1-6) one may write the equation of the circuit voltages in Figure 2.5 by using Kirchhoff's second law:

$$U_C(t)+U_L(t)+U_{Rcir}(t)+U_W(t)=0 \tag{5.1}$$

The differential equation for the current then becomes

$$\frac{1}{C}I(t)+L\frac{d^2I(t)}{dt^2}+\frac{dI}{dt}\left(R_{cir}+R_W(t)\right)+I(t)\frac{dR_W(t)}{dt}=0\ . \tag{5.2}$$

When solving for the second differentiation with respect to the time on receives

$$\frac{d^2I(t)}{dt^2}=-\frac{1}{L}\left[\frac{1}{C}I(t)+\frac{dR_W(t)}{dt}I(t)+\left(R_{cir}+R_W(t)\right)\frac{dI}{dt}\right], \tag{5.3}$$

while assumption (6) allows to write the wire resistance as

$$R_W(t)=\rho_W(t)\frac{l}{S}\ . \tag{5.4}$$

Then, then change of the wire resistance with respect to the time becomes:

$$\frac{dR_W(t)}{dt}=\frac{d\rho_W(t)}{dt}\frac{l}{S} \tag{5.5}$$

Since the specific resistance ρ_W of the wire material is a function of its temperature T, one could construct expressions for $\rho_W(T)$. As the temperature is further a function of the involved energy density ($T(e_{V,i})$, one may express ρ_W without T. However, one may assume the specific resistance as a linear function ρ_W depending on of the *energy density* $e_{V,i}$ inside the wire:

$$\rho_W(t)=\rho_W\left(e_{V,i}(t)\right)=\rho_{W0}+me_{V,i}(t) \tag{5.6}$$

Here, ρ_{Wo} represents an initial value of specific resistance, while m is the slope factor of the linear equation. The time deviation of equation (5.6) gives:

$$\frac{d\rho_W(t)}{dt}=m\frac{de_{V,i}(t)}{dt} \tag{5.7}$$

When putting in equation (5.4- 5.7) into equation (5.3), one receives the term

$$\frac{d^2I(t)}{dt^2}=-\frac{1}{L}\left[\frac{1}{C}I(t)+m\frac{de_{V,i}(t)}{dt}\frac{l}{S}I(t)+\left(R_{cir}+\left(\rho_{W0}+me_{V,i}(t)\right)\frac{l}{S}\right)\frac{dI}{dt}\right], \tag{5.8}$$

which includes the *time deviation of the energy density*. Since the time deviation of the energy density is equal to the *volume power density*, one may write:

$$\frac{de_{V,i}(t)}{dt}=\frac{dP_W(t)}{dV}=I^2(t)\rho_W(t)\frac{l}{SV}=I^2(t)\frac{\rho_W(t)}{S^2}=\frac{1}{S^2}\left(\rho_{W0}+me_{V,i}(t)\right)I^2(t) \tag{5.9}$$

By putting this expression into equation (5.8) one finally receives

$$\frac{d^2I(t)}{dt^2}=-\frac{1}{L}\left[\frac{1}{C}I(t)+m\frac{l}{S^3}\left(\rho_{W0}+me_{V,i}(t)\right)I^3(t)+\left(R_{cir}+\left(\rho_{W0}+me_{V,i}(t)\right)\frac{l}{S}\right)\frac{dI}{dt}\right] \tag{5.10}$$

The deviation of the capacitor voltage may be expressed by

$$\frac{dU_C(t)}{dt}=-\frac{I(t)}{C}\ , \tag{5.11}$$

while the deviation of the action integral (compare equation 4.16) may be written as

$$\frac{dA(t)}{dt} = I^2(t) \ . \tag{5.12}$$

If one defines a function $s(t)$ as the time derivative of the current $I(t)$,

$$s(t) = \frac{dI}{dt} \ , \tag{5.13}$$

one may gain a system of ordinary differential equations (ODEs). By defining the boundary conditions as $I(0) = 0$, $\frac{dI(0)}{dt} = \frac{U_C(0)}{L}$, $e_{V,i}(0) = 0$, $U_C(0) = U_{C0}$, $A(0) = 0$, one may write down all the discovered differential equations as a coupled system (Table 5.1).

nr.	boundary cond.	differential equation	solved function
0	$I(0) = 0$	$\frac{dI(t)}{dt} = s(t)$	$I(t)$
1	$\frac{dI(0)}{dt} = \frac{U_C(0)}{L}$	$\frac{ds(t)}{dt} = \frac{d^2I(t)}{dt^2} = -\frac{1}{L}\left[\frac{1}{C}I(t) + \frac{ml}{S^3}\left(\rho_{W0} + me_{V,i}(t)\right)I^3(t) + \left(R_{cir} + (\rho_{W0} + me_{V,i}(t))\frac{l}{S}\right)\frac{dI}{dt}\right]$	$s(t) = \frac{dI(t)}{dt}$
2	$e_{V,i}(0) = 0$	$\frac{de_{V,i}(t)}{dt} = \frac{1}{S^2}\left(\rho_{\mathbf{wo}} + me_{V,i}(t)\right)I^2(t)$	$e_{V,i}(t)$
3	$U_C(0) = U_{\mathbf{C0}}$	$\frac{dU_C(t)}{dt} = -\frac{I(t)}{C}$	$U_C(t)$
4	$A(0) = 0$	$\frac{dA(t)}{dt} = I^2(t)$	$A(t)$

Table 5.1: ODE system for numerical simulation of pulsed wire discharges with a linearized resistance characteristic ($\rho_W(e_{V,i}) = \rho_{W0} + me_{V,i}$)

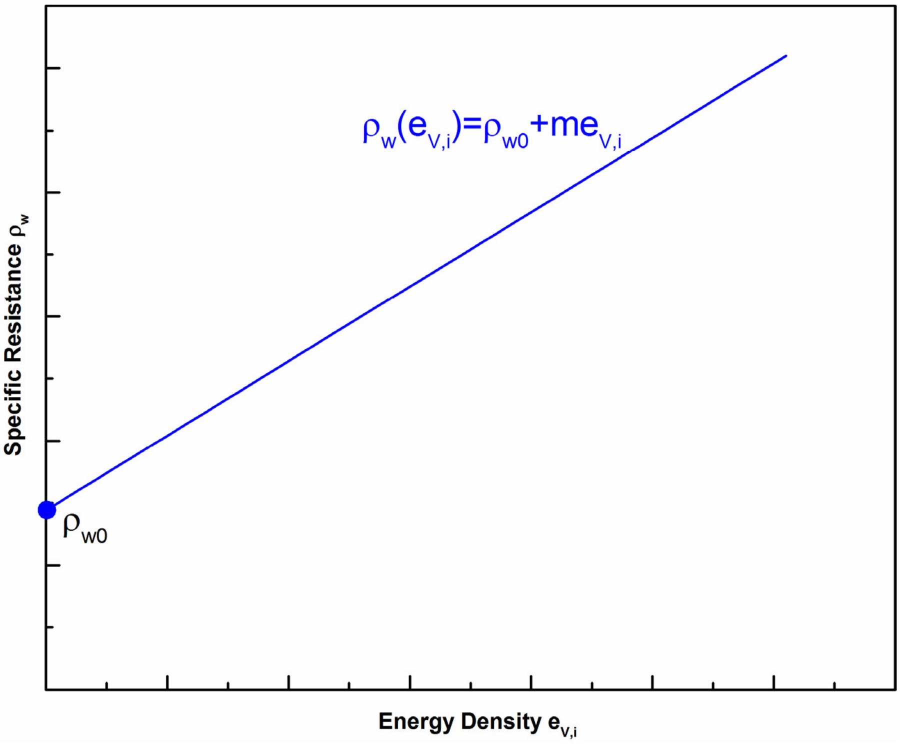

Figure 5.2: Example of a linearized resistance characteristic. The specific resistance is defined as a linear function, it depends on the inherent energy density within the wire ($\rho_W(e_{V,i}) = \rho_{W0} + me_{V,i}$).

5.3.2 Proof of Simulation Accuracy via energy conservation

The differential equation system presented in Table 5.1 may be numerically solved by using the *Runge Kutta Algorithms*. In order to prove the accuracy of the simulated functions, one may use the computed values $I(t)$, $e_{V,i}(t)$, $U_C(t)$, $A(t)$ so as to derive the following energies:

(1) Capacitor energy

The capacitor energy may be easily computed by

$$E_C(t)=\frac{1}{2}CU_C^2(t) \; . \tag{5.14}$$

(2) Magnetic Energy created by circuit inductance

The energy related to the inductance is defined by

$$E_L(t)=\frac{1}{2}LI^2(t) \; , \tag{5.15}$$

which is the value of the total magnetic energy created by the current carrying circuit.

(3) Energy absorbed within the circuit resistance

By multiplication of the action with the circuit resistance, one obtains the lost energy of the circuit:

$$E_{cir} = A(t)R_{cir} \tag{5.16}$$

(4) Energy absorbed in wire

The energy absorbed within the wire may be derived through multiplication of the energy density together with the wire volume (radius r and length l):

$$E_W(t)=e_{V,i}(t)r^2l \tag{5.17}$$

All together the accuracy of the simulations is provable by summation of all 4 involved energies:

$$E_{total}=\frac{1}{2}CU_C^2(t)+\frac{1}{2}LI^2(t)+e(t)r^2\pi l+A(t)R_{cir}\overset{!}{=}const. \tag{5.18}$$

For a precise simulation the total energy should be similar to the initially stored energy in the capacitor E_{C0} over the whole simulation time. The difference of the total energy in the system $E_{total}(t)$ and the initial energy stored in the capacitor E_{C0} may be written as:

$$\Delta E_{sim}(t)=E_{total}(t)-E_{C0} \tag{5.19}$$

The absolute maximum of the curve ($\max|\Delta E_{sim}(t)|$) further allows to quantify the maximum error in relation to the initial energy:

$$energy\,error(\%) = 100 \cdot \frac{\max\left|\Delta E_{sim}(t)\right|}{E_{C0}} \tag{5.20}$$

To get a more precise simulation result with a smaller *energy error* one may reduce the step rate *h*. In addition, one may also use adaptive step size integration algorithms like *Cash Karp* [46] for example, which enables a much better simulation accuracy. However, when increasing the accuracy then the required simulation time also goes up significantly, so that one has to find a compromise between the two.

5.3.3 Stepwise linearisation of resistivity depending on energy density

A stepwise approach was conceived, since the resistance characteristics presented in Figure 4.10 and Figure 4.14 are not linear. By fitting against an experimentally gained resistance characteristic $\rho_W(e_{V,i})$, which includes individual linear functions (control variable *k*) one may write:

$$\rho_{W(k)} = \rho_{W0(k)} + m_{(k)} e_{V,i} \tag{5.21}$$

Hence, at room temperature the start value of the first linear function (*k=0*) is equal to the specific resistance of the wire material (e.g. $\rho_{W0(k=0)}$=0,70μΩm). Up to the boiling point, which is reached at an energy density of $e_{V,i}$ ≈25 J/μl, one may use the experimentally gained fit equation (4.29) to compute the needed values for $\rho_{W0(k)}$ and $m_{(k)}$. Figure 5.3 shows the experimental data (red) together with adapted linear fit functions (dashed in white).

The end values of each individual fit spline are called P_k, and furthermore represent the start value within the subsequent fit function below. However, one may use arbitrary supporting points ($\rho_{W0(k)}$; $e_{V,i(k)}$), which do not have to be necessarily equidistantly related to the energy density $e_{V,i}$.

By using the defined spline equations $\rho_{W(k)}(e_{V,i})$ one may modify the previously gained system of differential equations (Table 5.2). Then the system represents an individual problem for each spline, with specific new parameters. After starting with the first boundary conditions $I_{(k=0)}$ =(0), $s_{(k=0)}$(0)=U_0/L, $e_{V,i(k=0)}$(0)=0, $U_{C(k=0)}$=U_{C0}, $A_{(k=0)}$(0)=0, the next splines are computed with modified differential equations, but now taking the last values of the computed quantities from the previous splines as starting conditions:

$I_{(k)}(t_{start}) = I_{(k-1)}(t_{end})$, $s_{(k)}(t_{start}) = s_{(k-1)}(t_{end})$, $e_{V,i(k)}(t_{start}) = e_{V,i(k-1)}(t_{end})$,
$U_{C(k)}(t_{start}) = U_{C(k-1)}(t_{end})$, $A_{(k)}(t_{start}) = A_{(k-1)}(t_{end})$

The accuracy of the numerically solved differential equation system is able to be proven through the equation (5.18).

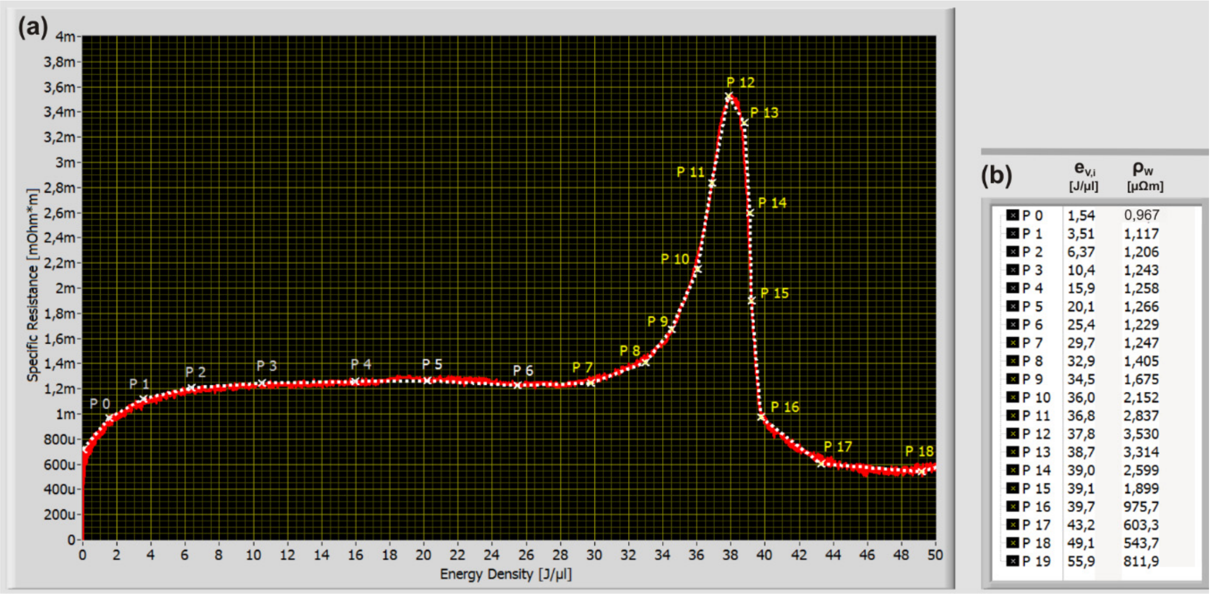

(b)	$e_{V,i}$ [J/µl]	ρ_W [µΩm]
☒ P 0	1,54	0,967
☒ P 1	3,51	1,117
☒ P 2	6,37	1,206
☒ P 3	10,4	1,243
☒ P 4	15,9	1,258
☒ P 5	20,1	1,266
☒ P 6	25,4	1,229
☒ P 7	29,7	1,247
☒ P 8	32,9	1,405
☒ P 9	34,5	1,675
☒ P 10	36,0	2,152
☒ P 11	36,8	2,837
☒ P 12	37,8	3,530
☒ P 13	38,7	3,314
☒ P 14	39,0	2,599
☒ P 15	39,1	1,899
☒ P 16	39,7	975,7
☒ P 17	43,2	603,3
☒ P 18	49,1	543,7
☒ P 19	55,9	811,9

Figure 5.3: Step by step fit of the specific resistance data. (a) experimental data curve (in red) is fitted on manually through linear functions (white dashed lines), **(b)** table of the supporting points P_k.

nr.	boundary condition	differential equation	solved function
0	$I_{(k)}(t_{start}) = I_{(k-1)}(t_{end})$	$\frac{dI_{(k)}(t)}{dt} = s_{(k)}(t)$	$I_{(k)}(t)$
1	$s_{(k)}(t_{start}) = s_{(k-1)}(t_{end})$	$\frac{ds_{(k)}(t)}{dt} = -\frac{1}{L}\left[\frac{1}{C}I_{(k)}(t) + \frac{m_{(k)}l}{S^3}\left(\rho_{w0(k)} + m_{(k)}e_{V,i(k)}(t)\right)I_k^3(t) + \left(R_{cir} + (\rho_{w0(k)} + m_{(k)}e_{V,i(k)}(t))\frac{l}{S}\right)\frac{dI_{(k)}(t)}{dt}\right]$	$s_{(k)}(t)$
2	$e_{V,i(k)}(t_{start}) = e_{V,i(k-1)}(t_{end})$	$\frac{de_{V,i(k)}(t)}{dt} = \frac{1}{S^2}\left(\rho_{w0(k)} + m_{(k)}e_{V,i(k)}(t)\right)I_{(k)}^2(t)$	$e_{V,i(k)}(t)$
3	$U_{C(k)}(t_{start}) = U_{C(k-1)}(t_{end})$	$\frac{dU_{C(k)}(t)}{dt} = -\frac{I_{(k)}(t)}{C}$	$U_{C(k)}(t)$
4	$A_{(k)}(t_{start}) = A_{(k-1)}(t_{end})$	$\frac{dA_{(k)}(t)}{dt} = I_{(k)}^2(t)$	$A_{(k)}(t)$

required initial boundary conditions: $I_{(k=0)}$ =(0), $s_{(k=0)}$(0)=U_{C0}/L, $e_{V,i(k=0)}$(0)=0, $U_{C(k=0)}$=U_{C0}, $A_{(k=0)}$(0)=0

Table 5.2: ODE System for numerical simulation of pulsed wire discharges with *stepwise linearized* resistance characteristic functions $(\rho_{W(k)}(e_{V,i}) = \rho_{W0(k)} + m_{(k)}e_{V,i})$

5.4 Software implementation

5.4.1 General handling

After the mathematical derivation of the semi-physical dependencies and its assumptions, a software with a graphical user interface was built. The differential equation system was implemented within a self-built application inside *Labview* (Figure 5.4).

Hence, the resistance characteristic yield by previous experiments (chapter 4.2) may be uploaded for an individual data fit Ⓐ. After defining the capacitance C, initial capacitor voltage U_{C0}, circuit inductance L, circuit resistance R_{cir} Ⓑ, one should specify the wire dimensions (length l, diameter d) Ⓒ.). Whenever the user found a suitable resistance characteristic, the data of this characteristic may be saved in a library and used afterwards for simulations with other discharge circle parameters (for example different capacitance, voltage, wire dimensions etc.). However the user has to decide, whether he wants to use a resistance characteristic from the library, or to perform an own fit Ⓓ. When one decides to click "*Self-Fitting of Resistance Characteristic*" it´s also possible to create an arbitrary design characteristic $\rho_W(e_{V,i})$. After specifying the number of the fit splines "*Spline Number*" and the start value $\rho_{W0(k=0)}$ Ⓔ, one may fit manually the resistance characteristic with linear splines Ⓖ. By using adaptive step-size integration algorithms such as *Cash Karp* instead of *Runge Kutta,* it is possible to simulate even more accurately the different resistance characteristics. Furthermore, the accuracy and step number are able to be defined and individually adapted Ⓕ. By clicking on the button "*Simulate*", the software will define the individual differential equation system (Table 5.2) with respect to the implied boundary conditions. The status of the numerical computation is displayed in the "*Progress*" bar Ⓗ. Since the operation principle of the software is much more complicated (e.g. many different interpolation methods for data array synchronisation are used), a detailed explanation of all the implemented methods, would go far beyond the scope of this thesis.

Hereafter, the handling of the software should be explained via a concrete example:

Because of the nice double hill shape regarding *I(t)*, the performed experiments in chapter 4.1.4 should be analysed via a precise simulation. Firstly, the resistance characteristic of the wire experiment (d=700 µm, l=120 mm) was loaded and fitted with linear splines Ⓖ. Simulations with this fit data Ⓘ provide a nearly perfect match between the "*simulated current*" (blue) and "*measured current*" (mint green) Ⓙ. The buttons on the upper right-hand side within the chart Ⓙ allow one to show or hide individual curves. By comparing the wire voltage curves concerning "*measured wire voltage*" (yellow) and "*simulated wire voltage*" (black), one recognises an excellent overlap of the given data. This confirms in a very illustrative way the applicability of the used methods, concerning simulated *Pulsed Wire Discharge Experiments*. Furthermore, the curve of the capacitor voltage $U_C(t)$ is also displayed in Ⓙ, which allows the experimenter to predict the quantity of voltage reversal. This is an important factor in order to be able to calculate the lifetime estimation of the used pulse capacitors [47]. The boundary conditions or rather end values of the individual differential equation systems are shown through circles. Their viewability may be also disabled. The accuracy of the simulation may be checked by the chart "*Accuracy- Time*" Ⓚ (compare chapter 5.4.2) on the one hand, or by the "Total Energy in System" chart Ⓛ on the other hand.

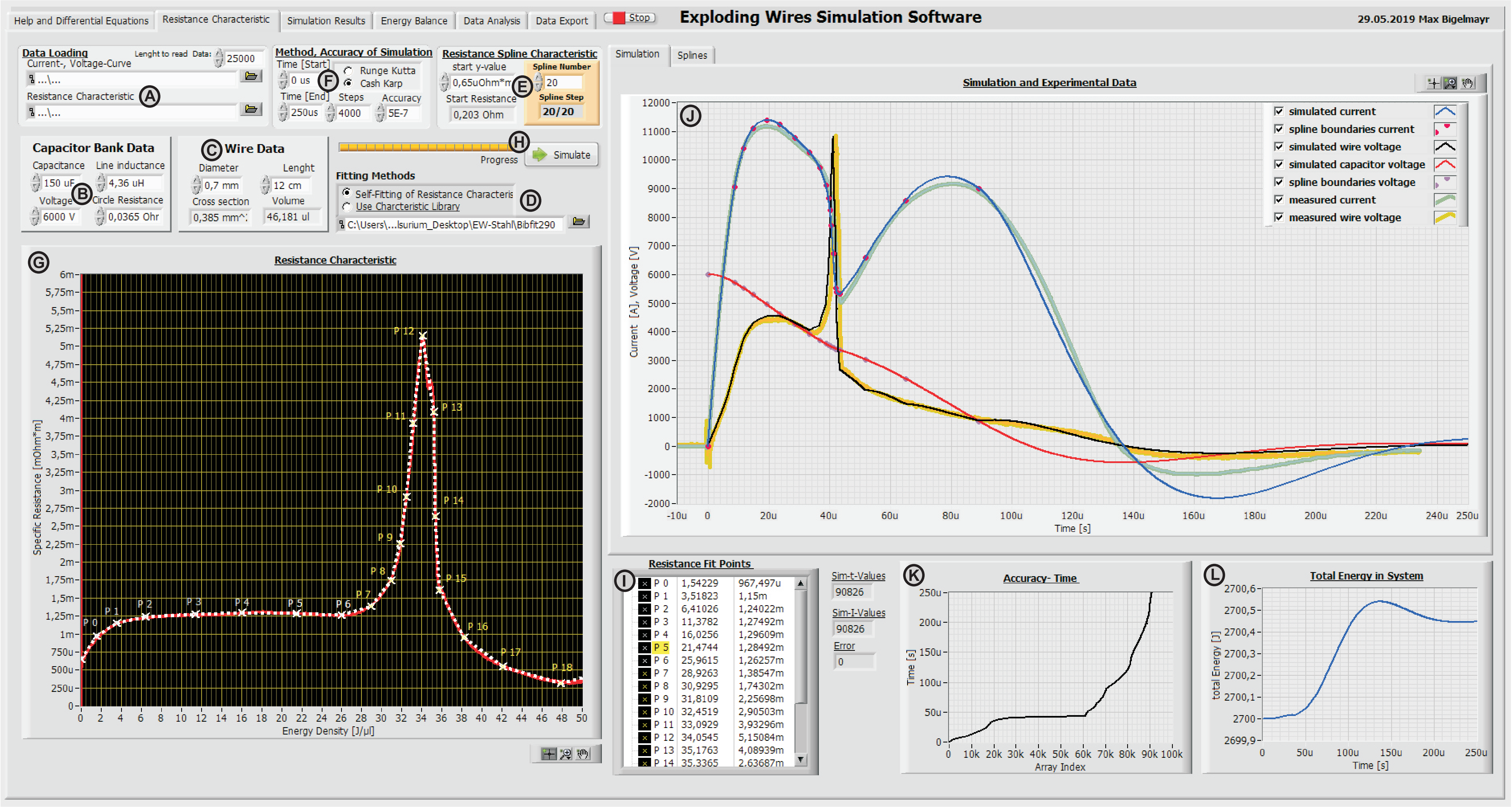

Data Loading

Lenght to read Data: 25000

Current-, Voltage-Curve: ...\...

Resistance Characteristic: ...\...

Method, Accuracy of Simulation

Time [Start]: 0 us

○ Runge Kutta

● Cash Karp

Time [End]: 250us

Steps: 4000

Accuracy: 5E-7

Resistance Spline Characteristic

start y-value: 0,65uOhm*m

Spline Number: 20

Start Resistance: 0,203 Ohm

Spline Step: 20/20

Capacitor Bank Data

Capacitance: 150 uF

Line inductance: 4,36 uH

Voltage: 6000 V

Circle Resistance: 0,0365 Ohm

Wire Data

Diameter: 0,7 mm

Lenght: 12 cm

Cross section: 0,385 mm^2

Volume: 46,181 ul

Fitting Methods

● Self-Fitting of Resistance Characteris

○ Use Charcteristic Library

C:\Users\...lsurium_Desktop\EW-Stahl\Bibfit290

Resistance Fit Points

P 0	1,54229	967,497u
P 1	3,51823	1,15m
P 2	6,41026	1,24022m
P 3	11,3782	1,27492m
P 4	16,0256	1,29609m
P 5	21,4744	1,28492m
P 6	25,9615	1,26257m
P 7	28,9263	1,38547m
P 8	30,9295	1,74302m
P 9	31,8109	2,25698m
P 10	32,4519	2,90503m
P 11	33,0929	3,93296m
P 12	34,0545	5,15084m
P 13	35,1763	4,08939m
P 14	35,3365	2,63687m

Sim-t-Values: 90826

Sim-I-Values: 90826

Error: 0

Figure 5.4: Screenshot of simulation software (main frontpanel), (C=150 µF, U_{C0}=6,00 kV, R_{cir}=36,5 mΩ, L=4,36 µH, X5CrNi18-10 wire, l=120 mm, d=700 µm)

Ⓐ Experimentally gained data concerning current, voltage and resistance characteristic may be uploaded here as a txt. file.

Ⓑ Data input for capacitance, capacitor voltage, circuit inductance and circuit resistance.

Ⓒ Wire data input (diameter, length) gives as a result the cross section [mm^2] and wire volume [µl]

Ⓓ Selection of a fitting method (manual or by library fit)

Ⓔ Input of a fit spline number n; k in (k/n) displays the actual computation progress

Ⓕ Selection of a solver method, end time, step number (only for Runge Kutta) and step accuracy

Ⓖ Chart uploaded as a resistance characteristic (red); manual fit (white dashed lines) of the experimental data

Ⓗ Button to start simulation; progress bar of the computations

Ⓘ Display and data input of the supporting points ($\rho_{W0(k)}$; $e_{V,i(k)}$); written on the right is the total number of simulation values (array length)

Ⓙ Chart which shows the simulated current, capacitor voltage, wire voltage; The points indicate the boundary conditions of the ΩDE systems.

Ⓚ Chart which indicates points in time related to the array indices. Simulations performed with *Runge Kutta* would show a linear curve.

Ⓛ Total system energy (this curve represents the accuracy of the simulation results)

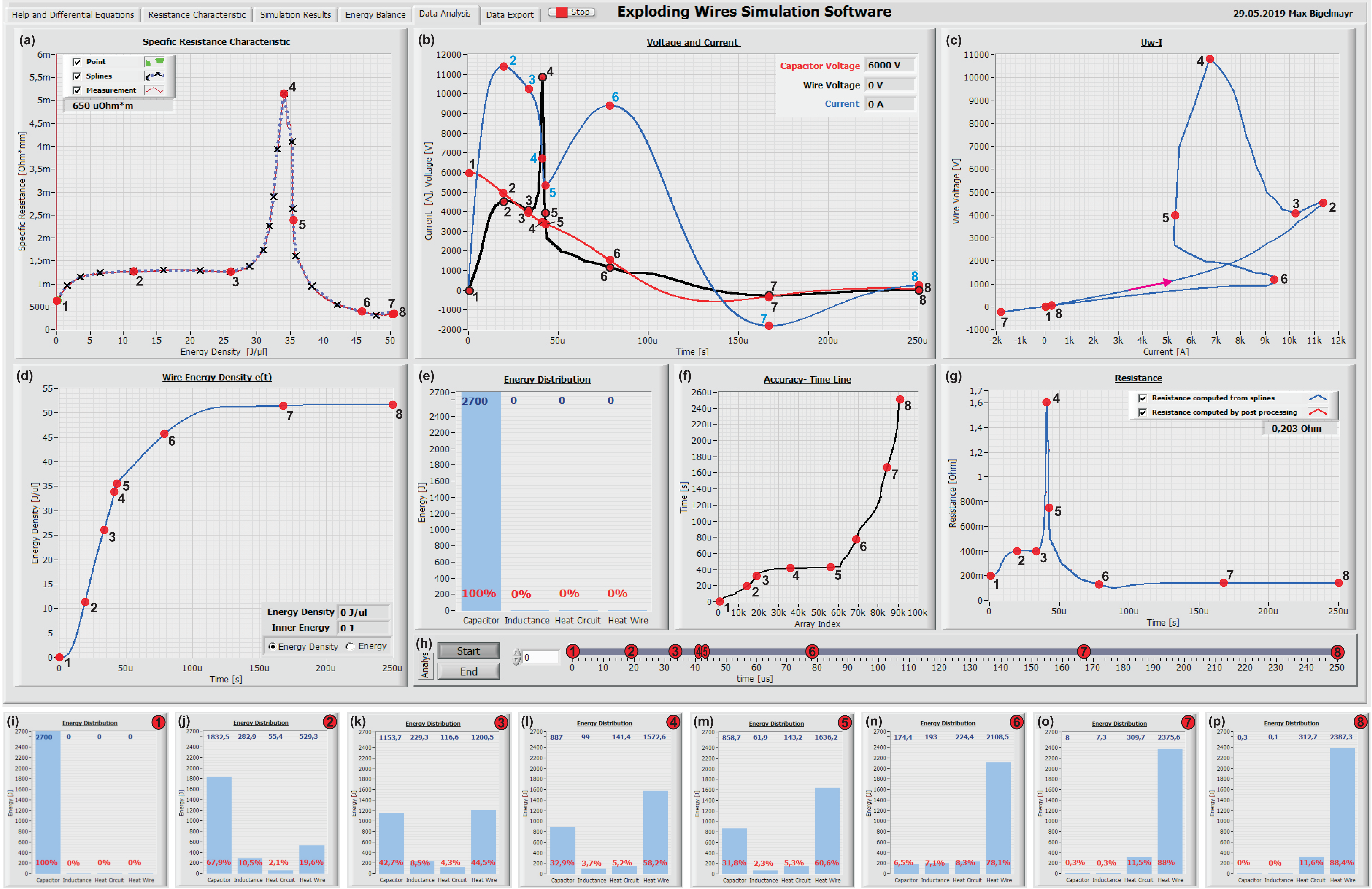

☑ Point
☑ Splines
☑ Measurement
650 uOhm*m

Capacitor Voltage 6000 V
Wire Voltage 0 V
Current 0 A

Energy Density 0 J/ul
Inner Energy 0 J
● Energy Density ○ Energy

☑ Resistance computed from splines
☑ Resistance computed by post processing
0,203 Ohm

Figure 5.5: Screenshot of simulation software (data analysis frontpanel), (C=150 µF, U_{C0}=6,00 kV, R_{ci}=36,5 mΩ, L=4,36 µH, X5CrNi18-10 wire, l=120 mm, d=700 µm)
(i-p) are not part of the simulation software, but represent the results from (e)

5.4.2 Simulation Results and Data Analysis

After the simulations, the simulated data may be analysed in greater detail. To be more precise, all the quantities mainly involved, are able to be analysed regarding their values within time (Figure 5.5). The pointer slide enables a precise definition of the point in time, that the user is interested in. While sliding along the timeline (Figure 5.5 h), a red dot travels along all the curves and indicates the correlating quantities. So, one is able to compare for example at which specific resistance ρ_W (Figure 5.5 a) the current reaches a certain value (Figure 5.5 b). Furthermore, the wire voltage and capacitor voltage are not only represented by a red dot but are also displayed by their specific values (right upper inset in Figure 5.5 b). Figure 5.5 (c) shows the path of the simulated experiment as an $U_w(I)$-chart. The absorbed energy density within the wire $e_{V,i}$(t) is shown in Figure 5.5 (d), which is also able to be switched on, in order to display the absorbed energy within the wire $E_W(t)$. This is possible by selecting the button on the bottom right hand side. The inherent energies, computed by equation (5.14- 5.18), are displayed as a dynamic bar chart (Figure 5.5 e), while at the same time showing the absolute quantities $E_C(t)$, $E_L(t)$, $E_{cir}(t)$ as well as $E_w(t)$ together with their percentage portions. Depending on the previously choosen solver method (Figure 5.4 Ⓕ), the "Accuracy-Time line" chart in Figure 5.5 (f) represents a linear (*Runge Kutta*) or a nonlinear fashion (*Cash Karp*). Figure 5.5 (g) represents the resistance of the wire $R_w(t)$. Since the movement of the timeline cursor in Figure 5.5 (h) is not able to be shown dynamically within this thesis, the following specific points in time should be investigated in more detail:

Number	①	②	③	④	⑤	⑥	⑦	⑧
Time [µs]	0	19,40	33,40	41,18	42,60	78,60	167,00	250,00

Table 5.3: Specified points in time in order to be able to perform a detailed system analysis

One may receive the energy distributions shown in Figure 5.5 (i-p), through analysis of the energy distribution (Figure 5.5 e), which is related to the specified time values. However, in the following sections, the mechanisms presented in Figure 5.5 should be briefly discussed:

At the beginning ① all the involved system energy (E_{total}=E_C=2700 J) is stored within the capacitor (Figure 5.5 i). As the start resistivity was set to 0,65 µΩm (Figure 5.4Ⓔ), the chart in Figure 5.5 (a) represents this value precisely at ①, while the wire resistance in Figure 5.5 (g) starts at 203 mΩ. After 19,40 µs ② the current curve in Figure 5.5 (b) reaches its peak value (11,4 kA), while the energy density increases in a roughly linear fashion. When regarding the wire voltage in Figure 5.5 (b), one is able to notice a local minima ③ at 33,40 µs. The point ③ represents the beginning of a rapid rise concerning the specific resistance in Figure 5.5 (a), as well as the beginning of a rapid rise regarding the wire resistance $R_w(t)$, shown in Figure 5.5 (g). The peak value of the specific resistance ④ is reached at 41,18 µs (Figure 5.5 a). Hereby one may notice, that the computational effort in-between ③ and ⑤ is very high, since the time slope within Figure 5.5 (f) is relatively low. Furthermore, point ④ represents the peak value within Figure 5.5 (c) and Figure 5.5 (g). Interestingly as widely assumed, point ④ in Figure 5.5 (a) does not represent the beginning of the plasma pulse, because the current curve still drops drastically at this exact moment in time (Figure 5.5 b).

However, the actual beginning of the plasma pulse is represented by the pointes ⑤. This is clearly identified by the local minimum of the current curve (Figure 5.5 b), as well as with the bend in Figure 5.5 (d). By comparing the bar charts concerning the energy distributions at ④ (Figure 5.5 l) and ⑤ (Figure 5.5 m), a significant difference in regards to the wire energy E_w is noticeable: Hereby E_w≈1573 J at ④, while E_w≈1636 J at ⑤. This difference of approximately 3,9%, may have a significant influence, when one does not precisely define the term *plasma pulse*. The second local maximum of the current curve in Figure 5.5 (b) is indicated by point ⑥. Hereby the specific resistance indicates a value of ρ_w≈0,400 µΩm (Figure 5.5 a). Concerning point ⑥ in Figure 5.5 (c), from this moment onwards, one is able to notice the beginning of a nearly constant resistance behaviour (compare also Figure 5.5 g). The minimum of the current curve ⑦ presented in Figure 5.5 b is reached at 167,00 µs. Even though the current reaches a value of I≈-1,8 kA, the magnetic energy of the circuit inductance lies at only 7,3 J, that is only around 0,3% of the total system energy (Figure 5.5 o). Finally, the end value of the simulation is reached at 250 µs, which is indicated by point ⑧. At this moment in time all the curves in Figure 5.5 (b) represent values, which are less than 1,7% of their peak values over the entire simulation. According to Figure 5.5 (p) the capacitor and inductance energies are only E_c=0,3 J and E_L=0,1 J. So, the energy finally absorbed within the wire is E_w≈2387,3 J (88,4% of E_{total}), while the lost energy within the circuit (*Heat Circuit*) is E_{cir}≈312,7 J (11,6% of E_{total}).

As described earlier in chapter 5.3.2, the total system energy $E_{total}(t)$ should be proven. Within the presented simulation, Figure 5.6 (a) shows the total energy $E_{total}(t)$, where the *Cash Karp Algorithm* of the 5th order was implemented. In contrast to this occurrence, Figure 5.6 (b) shows $E_{total}(t)$ concerning a simulation, which was performed by using the 4th order of *Runge Kutta*. In this case the maximum energy deviation, regarding the Cash Karp Algorithm is only: max|ΔE_{sim}|≈0,54 J (0,002% of E_{C0}). In contrast, the maximum energy deviation for the Runge Kutta Algorithm is reached at max|ΔE_{sim}|≈94 J (3,48% of E_{C0}).

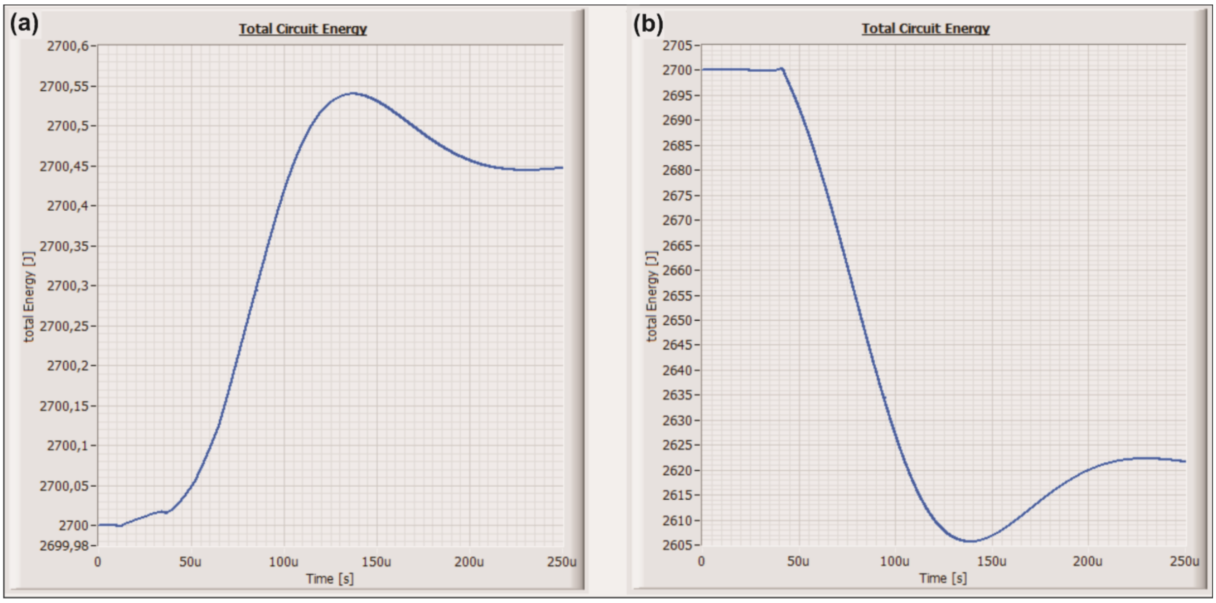

Figure 5.6: (a) total Energy $E_{total}(t)$ of simulations performed with *Cash Karp Algorithm 5th* order
(b) total Energy $E_{total}(t)$ of simulations performed with *Runge Kutta Algorithm 4th* order

6. Summary and conclusion

6.1 Summary

Starting with the theoretical principles of the *exploding wire phenomenon* (EWP), the different types of discharge behaviour were discussed at the beginning of this thesis. By introducing the Chace and Levin schema, it was possible to explain that "exploding wires", do not all behave in the same way. Through the explanation of MHD instabilities, the importance of time scale was able to be elucidated, what subsequently allows the classification into "*slow*" and "*fast explosions*".

Since the energy transformation during wire explosions is quite similar to the discharge behaviour of *RLC* circuits, the discharge current for the different kinds of damping behaviour were discussed. Hereby special emphasis was given to the energy absorption and critical damping behaviour of *RLC* circuits. Due to the fact that the wire resistance is not constant during exploding wire experiments, the description of an *RLC* circuit with variable resistance *R(t)* was introduced in chapter 2 and further elaborated in chapter 5.

The experimental setup used for the presented investigations was explained in sufficient detail, so as to be able to comprehend the procedure of the performed experiments. Since the capacitor bank includes a network of 23 capacitors and many cable connections, which act as inductances, an equivalent circuit diagram (*RLC*) was derived. However, the experimental setup may be described by a circuit resistance (without wire) of R_{cir}=36,4 mΩ, a capacitance of *C*=150 µF and a circuit inductance of *L*=4,36 µH. During the experiments the discharge current was measured with a Rogowski coil (CWT 300LFB- 0,1 mV/A). At the same time the wire voltage U_w was measured with a high voltage probe from Tektronix (P6015A), which itself is placed within a shielded construction. Together both the curves of wire voltage and current were able to be captured by a battery driven digital oscilloscope (Owon DS6062).

In the experimental part, the choice of wire material (*X5CrNi18*-10) was reasoned by its high specific resistance ($\rho \approx 0{,}73\,\Omega\,\mathrm{mm}^2/\mathrm{m}$ at 20°C [20]), as compared to pure metal elements. This enables one to reach the ideal resistance R_{cd}, which is required in order to reach a critical damping behaviour with much less wire volume, in comparison to pure metal elements. The use of this alloy is particularly interesting, since no systematic study, with the alloy *X5CrNi18*-10 as a wire material in pulsed wire discharge experiments has been done so far. Through a broad literature review, one was able to compute with sufficient accuracy the sublimation enthalpy of the alloy *X5CrNi18*-10. This in turn allowed the approximation of the needed wire dimensions in order to perform the experiments. Hereby the sublimation enthalpy of the steel alloy was determined as ΔH_{sub}=9618 J/g, which is equal to an energy density in relation to the initial volume of $e_{V,i}$(sub)=76 J/µl.

The description of the data analysis involves a personally conceived operation algorithm, which allows data filtering, voltage correction and computation of many important quantities. Then, the experimental data stored by the oscilloscope is able to be post processed, in order to receive the curves for wire voltage U_w, wire resistance R_w, absorbed energy within the wire E_w, energy density within the wire $e_{V,i}$, specific resistance of the wire $\rho_W(t)$ and action *A(t)* etc. Finally, the curve which is given through the specific resistance of the wire, in dependence of the energy density $\rho_W(e_{V,i})$, is able to be computed for each individual experiment.

The usefulness of separate experiments for a systematic evaluation could be substantiated by performing repetitive experiments with identical circuit parameters (C=150 µF, U_{C0}=6,00 kV, L=4,36 µH, X5CrNi18-10 wire, l=120 mm, d=800 µm). Hereby, an excellent repeatability of the experiments (at least for this parameter combination) could be shown.

The results of the experiments, in which the effect of capacitor charging voltage was investigated, may be summarised as follows: When one fixes the circuit parameters (C=150 µF, L=4,36 µH, X5CrNi18-10 wire, l=120 mm, d=800 µm) and enlarges the wire voltage U_{C0}=[4,42; 6,00] kV,

the peak values of the current *I(t)* increase: I_{max} =[8,86; 11,17] kA
the peak values of the wire voltage U_w increase: $U_{w\,max}$ =[3,30; 10,80] kV
the final energy absorbed within the wire E_w increases: $E_{W\infty}$ =[1306; 2366] J
the efficiency $\eta = E_{W\infty}/E_{C0}$ decreases: η=[0,85; 0,61]
the peak values of the specific resistance, dependent on the energy density $\rho_W(e_{V,i})$, are shifted towards higher energy densities: $e_{V,i}$[max(ρ_W)]=[25,7; 34] J/µl

The results of the experiments, where the effect of wire length and diameter were investigated, may be summarised as follows: When one fixes the circuit parameters (C=150 µF, U_{C0}=6,00 kV, L=4,36 µH, X5CrNi18-10 wire) and modifies the wire dimension (l= [40; 160] mm) by enlarging the wire diameter d=[600; 800] µm),

the peak values *I(t)* of *heat pulses* increase: [8]I_{max}=[11,68; 16,59] kA
the peak values *I(t)* of *plasma pulses* decrease: [8]I_{max}=[17,72; 13,59] kA
the finally reached action value A_∞ decreases: [8]A_∞=[18,56; 13,70] kA^2s
the finally absorbed energy within the wire $E_{w\infty}$ increases: [8]$E_{W\infty}$ =[1989; 2211] J
the ratio E_{hp}: E_{pp} increases: [8]E_{hp}: E_{pp}=[46%:54%; 69%:31%]
the efficiency η increases: [8]η=[0,74; 0,82]

When holding on to the circuit parameters (C=150 µF, U_{C0}=6,00 kV, L=4,36 µH, X5CrNi18-10 wire) and modifying the wire dimensions (d=[600; 800] µm) by enlarging the wire length (l= [40; 160] mm),

the total peak values of the current *I(t)* decrease: [9]I_{max} =[22,56; 9,67] kA
the peak values of the first local peak from $U_w(t)$ decrease: [9]I_{max} =[19,07; 9,67] kA
the peak values of the specific resistance $\rho_W(e_{V,i})$,
are shifted to lower energy densities: [9]$e_{V,i}$[max(ρ_W)]=[42,0; 29,9] J/µl
the finally reached action value A_∞ decreases: [9]A_∞=[29,53; 6,87] kA^2s
the finally absorbed energy within the wire $E_{w\infty}$ increases: [9]$E_{w\infty}$=[1671; 2462] J
the E_{hp}: E_{pp} decreases: [9]E_{hp}:E_{pp}=[39%:61%; 75%:25%]
the efficiency η increases: [9]η=[0,62; 0,91]

---

[8] results with a wire length of l=80 mm

[9] results with a wire diameter of d=700 µm

Up to $e_{V,i}$=25,3 J/µl, the specific resistance depending on the energy density $\rho_W(e_{V,i})$ may be fitted quite perfectly by the function:

$$\rho_W(e_{V,i}) = 1{,}27 - 0{,}617 \cdot 0{,}69^{e_{V,i}}$$

Only for data points where 25,3 J/µl $<e_{V,i}$ the resulting values of the specific resistance within the wire differ significantly from one to another depending on the used length and diameter of the wire.

In the modelling part of the thesis the motivation for creating a simulation software was explained. From start, the goal was to develop an easy to use software with a graphical user interface. By using suitable model assumptions (single capacitance C, constant circuit resistance R_{cir}, no mechanical deformation of cables, neglection of stray capacitances, isochoric behavior of the wire) a system of ordinary differential equations (ODEs) could be derived. This system was implemented in a software tool with graphical user interface in Labview. By linearising stepwise the resistivity depending on energy density $\rho_W(e_{V,i})$, the system may be solved by using Runge Kutta algorithms. However, the user has to decide, whether he wants to use a resistance characteristic from a library included in the software, or to perform an own fit with arbitrary supporting points. Since the resistance charcteristics $\rho_W(e_{V,i})$ are independent from the wire dimensions for $e_{V,i}$<25,3 J/µl (Figure 4.14), therefore the simulation software is highly suitable for computations of at least the boiling point concerning the alloy X5CrNi18-10. Only higher temperatures resp. energy densities cannot be predicted by the software, regarding the discharge behaviour at later points in time. Nevertheless, for a given resistance characteristics, the accuracy of the numerically solved differential equation system, can be validated through the total energy $E_{sum}(t)$ of the simulated model.

For a first investigation on the software performance, the experimental results of an exploding wire experiment (C=150 µF, U_{C0}=6,00 kV, L=4,36 µH, X5CrNi18-10 wire, l=120 mm, d=700 µm) were reproduced numerically. By using the Cash Karp algorithm 5th order, the energy deviation from the initial energy was extremely low: max(ΔE_{sim})≈0,54 J (0,002% of E_{C0}). This allowed a precise analysis of the main time dependent quantities involved: $I(t)$, $U_C(t)$, $U_W(t)$, $R_W(t)$, $E_W(t)$. By comparing the simulated current $I_{sim}(t)$ with the experimentally measured current $I(t)$ a very good accordance could be found. Comparing the simulated wire voltage $U_{wsim}(t)$ with the measured wire voltage $U_w(t)$ the accordance found was even better. Altogether the software appears to be an excellent tool to plan and analyse exploding wire experiments. Furthermore, a very interesting outcome could be found:

The peak value of the specific resistance characteristic $max[\rho_W(e_{V,i})]$ does not correlate in time with the local minima of the current $min_1[\rho_W(e_{V,i})]$. Actually, the point in time, where the plasma pulse starts, correlates with the bend of the absorbed energy in the wire $E_w(t)$. At this point in time the specific resistance $\rho_W(e_{V,i})$ is situated in the falling edge already.

6.2 Discussion

All the experiments performed for this thesis were done with a constant capacitance C=150 µF and circuit inductance L_{cir}=4,36 µH. The experiments performed in chapter 4.2 investigated the effect of capacitor charging voltage within the spectrum of U_{C0}=[4,42; 6,00] kV. The analysis of the resistance characteristic $\rho_W(e_{V,i})$ shows a strong dependency towards the location max($\rho_W(e_{V,i})$) related to U_{C0}. This effect, together with the dependency of wire length towards $\rho_W(e_{V,i})$, was figured out in chapter 4.2.2. Even though one is able to interpret this effect [31], the real physical mechanism is nowadays still not fully understood. In general, the physical understanding of a wire's resistance behaviour, be it in a solid, liquid and plasma phase, could help to find further rules and conditions, as to how the resistance characteristic $\rho_W(e_{V,i})$ must be modified. This could possibly be achieved via the correlations between field strength dependencies ε, current I or power dependencies P_W, which might be valid for all experiments. However, the suggestion from Yin et al. [36] to use an additional condition, be it in the form of a linearisation of the specific action, which reaches a certain resistivity and the involved maximum current density, seems not to be an ideal approach, because the measurement data scatters a lot in comparison to the fitting line (compare Fig. 9 in [36]). Instead of this correlation other correlations may be found, which allow one to adjust the resistance characteristic in a recursive pattern within simulations up until the point that they are able to reach the identified condition. Finally, a researcher interested in this field, has to make their own decision whether such semi-physical approaches are helpful, in order to improve simulation algorithms, or is it more promising to take the approach of using the MHD equations. The numerical approach of solving the MHD equations, could be verified with experimental data, which may be attained in further experiments.

Future experiments could involve high speed photography, combined with X-ray flash photography. With such photography, triggered by suitable time delays, one would be able to analyse the density and homogeneity of the wire, during the explosion phases. This could help to understand the beginning of the plasma phase. Furthermore, one would be able to identify restrike regions [11], which could be the reason for anomalies in the resistance characteristic [31].

The presented experiments could be repeated under water *(UEWE*s), for practical applications like *sheet metal forming.* Hence one would be able to analyse the created pressure waves, combined with spectroscopic methods, which together allow one to measure the propagation speed, of the pressure waves. Such research, combined with *sheet metal forming* experiments, could help to facilitate future industrial applications [7].

7. Bibliography

[1] Nairne, Edward (1774), *Electrical experiments by Mr. Edward Nairne*. In *Philosophical Transactions of the Royal Society of London* (64), pp. 79–89.

[2] Toepler, M. (1898), *Beobachtung von Metalldampfschichtung bei electrischer Drahtzerstäubung*. In *Annalen der Physik* 301 (8), pp. 873–876.

[3] McGrath, J. R. (1966), *Exploding Wire Research 1774-1963*. NRL Memorandum Report 1698, U.S. Naval Research Laboratory.

[4] Chace, W. G.; Moore, H. K. (1959), *Exploding Wires.* Based on Conference on the Exploding Wire Phenomenon. New York: Plenum Press, INC. (1).

[5] Chace, W. G.; Moore, H. K. (1962), *Exploding Wires.* Proceedings of the Second Conference on the Exploding Wire Phenomenon. New York: Plenum Press (2).

[6] Früngel, F. (Ed.) (1965), *High Speed Pulse Technology*. New York: Academic Press (1).

[7] Lange, Kurt; Liewald, Mathias (2013), *Umformtechnik: Handbuch für Industrie und Wissenschaft*: Springer-Verlag (4).

[8] *High energy density capacitors for pulsed power applications* (2009), 2009 IEEE Pulsed Power Conference

[9] Wilhem Tiemann (1968), *Über die gasdynamischen Vorgänge während der Dunkelpause von Drahtexplosionen und ihre Bedeutung für die Wiederzündung*. *Z. Naturforsch.* 1952-1960 (23a).

[10] Chace, William G.; Levine, Morton A. (1960), *Classification of wire explosions*. In *Journal of Applied Physics* 31 (7), p. 1298.

[11] Sinton, Rowan; van Herel, Ryan; Enright, Wade; Bodger, Pat (2010), *Observations of the long distance exploding wire restrike mechanism*. In *Journal of Applied Physics* 108 (5), p. 53304.

[12] Romanova, V. M.; Ivanenkov, G. V.; Mingaleev, A. R.; Ter-Oganesyan, A. E.; Shelkovenko, T. A.; Pikuz, S. A. (2015), *Electric explosion of fine wires: Three groups of materials*. In *Plasma Physics Reports* 41 (8), pp. 617–636.

[13] Philippow, Eugen (1992), *Grundlagen der Elektrotechnik*: Verlag Technik.

[14] Grenfell P. Boicourt, *Electrical Characteristics of Coaxial Cable*, University of California, Los Alamos Scientific Laboratoy.

[15] Jackson, J. D. (2002), *Classical Electrodynamics*. 3rd ed.: de Gruyter.

[16] Rosa, Edward Bennett; Grover, Frederick Warren (1911), *Formulas and tables for the calculation of mutual and self-induction*: US Government Printing Office.

[17] Power Electronic Measurements Ltd (2002), *APPLICATION NOTES*. Available online at http://www.pemuk.com/Userfiles/CWT/CWT%20-%20Technical%20notes%20-%20001.PDF, checked on 6/10/2019.

[18] Vlastós, Antonios E., *Restrike Mechanisms of Exploding Wire Discharges*. In *Journal of Applied Physics* 1968 (39).

[19] Lázár K.; Varga, L. K.; Kis, V. K.; Fekete, T.; Klencsár, Z.; Stichleutner, S. et al. (2018), *Electric explosion of steel wires for production of nanoparticles: Reactions with the liquid media*. In *Journal of Alloys and Compounds* 763, pp. 759–770.

[20] THYSSENKRUPP MATERIALS EUROPE GMBH (2006), *X5CrNi18-10, Nichtrostender Autenitischer Stahl*,

[21] *Ullmanns Enzyklopädie der technischen Chemie* (1965). 3rd ed. München-Berlin: Urban & Schwarzenberg (16).

[22] Hust, J. G.; Lankford, A. B. (1984), *Update of Thermal Conductivity and Electrical Resistivity of Electrolytic Iron, Tungsten, and Stainless Steel*, National Engineering Laboratory, National Bureau of Standards, Center for Chemical Engineering.

[23] *ASM Handbook.* Thermophysical Properties (2008). With assistance of Juan J. Valencia, Peter N. Quested (15 Casting).

[24] Kopp, Hermann (1865), *Investigations of the specific heat of solid bodies*. In *Philosophical Transactions of the Royal Society of London* (155), pp. 71–202.

[25] Holleman, Wiberg (1995), *Lehrbuch der Anorganischen Chemie*. 101st ed. Berlin New York: de Gruyter.

[26] Kugel, Roger W. (1998), *Raoult's Law: Binary Liquid-Vapor Phase Diagrams: A Simple Physical Chemistry Experiment*. In *Journal of Chemical Education* (Vol. 75 No. 9).

[27] Stöcker (1998), *Taschenbuch der Physik*. 3rd ed.: Harri Deutsch.

[28] Savitzky, A.; Golay, M. J. E. (1964), *Analytical Chemistry.* Smoothing and Differentiation of Data by Simplified Least Squares Procedures. 36 volumes (8).

[29] G.W. Anderson and F.W. Neilson, *Use of the "Action Integral" in Exploding Wire Studies*. In : Exploding Wires, vol. 1, pp. 97–103.

[30] Tucker, T. J.; Toth, R. P. (1975), *A computer code for the prediction of the behavior of electrical circuits containing exploding wire elements*, Sandia National Laboratories.

[31] Reithel, R. J.; Blackburn, J. H. (1962), *A hydrodynamic explanation for the anomalous resistance of exploding wires*. In : Exploding Wires, vol. 2: Springer, pp. 21–31.

[32] Webb, F. H.; Hilton, H. H., *The Electrical and Optical Properties of Rapidly Exploded Wires*. In : Exploding Wires -Proceedings of the Second Conference, vol. 2, pp. 37–75.

[33] Winkler, Rudolf (1973), *Hochgeschwindigkeitsbearbeitung: Grundlagen und technische Anwendung elektrisch erzeugter Schockwellen und Impulsmagnetfelder*. 1st ed.: VEB Verlag Technik.

[34] Cnare, E. C.; Neilson, F. W. (1959), *Large exploding wires-correlation to small wires and pause time versus length dependency*: New York: Plenum Press.

[35] Tucker, T. J. (1961), *Behavior of exploding gold wires*. In *Journal of Applied Physics* 32 (10), pp. 1894–1900.

[36] Yin, Guofeng; Li, Xingwen; Jia, Shenli (2018), *Electrical characteristics of microsecond electrical explosion of Cu wires in air under various parameters*. In *IEEE Transactions on PlasmaScience* 46 (4), pp. 972–981.

[37] Bennett, F. D. (1958), *Energy partition in the exploding wire phenomena*. In *The Physics of Fluids* 1 (6), pp. 515–522.

[38] Bennett, F. D.; Burden, H. S.; Shear, D. D. (1961), *Correlated Electrical and Optical Measurements of Exploding Wires*, Aberdeen Proving Ground, Maryland, Ballistic Research Laboratories.

[39] Good, R. C. (1964), *Resistance Variation of Exploding Wires*, General Electric, Space Science Laboratory.

[40] R. L. Doney, G. B. Vunni, J. H. Niederhaus (2010), *Experiments and Simulations of Exploding Aluminum Wires: Validation of ALEGRA-MHD*, Sandia National Laboratories, Army Research Laboratory.

[41] Abramova, K. B.; Zlatin, N. A.; Peregud, B. P. (1975), *Magnetohydrodynamic instability of liquid and solid conductors. Destruction of conductors by an electric current*. In *Zh. Eksp. Teor. Fiz* 69 (6), pp. 2007–2022.

[42] Hogg, M.; Timoshkin I., MacGregor S., Given M., Wilson M., Wang T., *Simulation of spark dynamic plasma resistance and inductance using PSpice*, Department of Electronic and Electrical Engineering University of Strathclyde, Glasgow.

[43] P. Lindskog; L. Ljung (1994), *Tools for Semi-Physical Modeling*, Linkoping University, Copenhagen, Department of Electrical Engineering.

[44] Früngel, F. (1960), *Impulstechnik–Erzeugung und Anwendung von Kondensatorentladungen*, Leipzig. Akademische Verlagsgesellschaft Geest&Portig KG.

[45] Feynman, Richard Phillips; Leighton, Robert B.; Sands, Matthew (1979), *The Feynman lectures on physics, vol. 2: Mainly electromagnetism and matter*: Addison-Wesley,

[46] Cash, Jeff R.; Karp, Alan H. (1990), *A variable order Runge-Kutta method for initial value problems with rapidly varying right-hand sides*. In *ACM Transactions on Mathematical Software (TOMS)* 16 (3), pp. 201–222.

[47] General Atomics (Ed.) (2003), *The Effect on Reversal on Capacitor Life.* Capacitor Engineering Bulletin 96-004, Sorento Electronics; In

Danksagung

Zunächst möchte ich mich ganz herzlich bei Anton Mangold (iQ-mobil solutions GmbH) für die großartige Unterstützung bedanken, mein Berufsleben für einige Zeit zu unterbrechen, um noch einmal zu studieren. Die Entscheidung von Bayern in den hohen Norden nach Rostock zu gehen, habe ich nie bereut. Ich habe eine neue Kultur erlebt und vieles gelernt.

Im Laufe des Studiums ist mir ein Professor besonders aufgefallen. So habe ich mit Begeisterung die Vorlesung von Prof. Dr. rer. nat. Dirk Uhrlandt besucht. Motiviert durch zahlreiche Gespräche nach den Vorlesungen, schlug ich ihm ein Masterarbeitsthema vor, das mich schon lange interessiert. Nach einem Kurzvortrag über meine Ideen ermöglichte mir Prof. Uhrlandt schließlich, die Masterarbeit über *gepulste Drahtentladungen* zu schreiben. Begeistert von seiner Offenheit, fing ich an alles zu planen. Die vielen Gespräche mit ihm über meine *Reports* halfen mir stets weiter, neue Details zu untersuchen. Darüber hinaus nahm er sich immer Zeit all meine Fragen zu beantworten und mir weiterzuhelfen. Gerade in der letzten Phase meiner Masterarbeit hat mich Prof. Uhrlandt sehr unterstützt und mich durch seine ungewöhnliche menschliche Art aufgemuntert. Hierfür möchte ich mich ganz herzlich bedanken und freue mich auf eine weitere Zusammenarbeit!

Während meiner Masterarbeit wurde ich von N. Dipl. B.Tech. Petrus Pieterse, dem Leiter des Hochspannungs-Labors der Uni Rostock, betreut. Vielen Dank für die Unterstützung! Die Anfertigungen der Kupferröhrchen konnten an der Universität Rostock von Schlossermeister Müller und Laboringenieur Steffen Sänger umgesetzt werden. Herzlichen Dank!

Ein ganz besonderer Dank gilt dem Metallbauer Stefan Kauf, sowie allen anderen beteiligten vom „Freihalder Stuhlkreis". Ob es die Schweißarbeiten (30 mm Stahl!) bis spät in die Nacht, das Lackieren der *Plasmakammer* am Samstagabend, oder „mal schnell was mit dem Stapler holen" ist: Ihr seid einfach genial!
Ein besonderer Dank gilt vor allem meinen Fachkollegen und Freunden Stefan Kluge, Rainer Szalata und Markus Petermann, die mich durch ihre außergewöhnlichen Vorschläge und Denkansätze stets inspiriert haben.
Dank an Frederic Chapman für seine „English-Native-Speaker-Kompetenz" und Benjamin Regler für seine fachkundigen redaktionellen Tipps. Elena Catti, Sonja Berger, Franz Heimerl und Christine Kastner haben mir oft nur durch einfaches Zuhören beim Darlegen meiner Ideen sehr weitergeholfen: Vielen Dank für eure Geduld!
In meiner ersten Woche in Rostock habe ich Heike Loeffler und Frank Rusch vom *Musikwohnzimmer* kennengelernt. Danke für die Möglichkeit jederzeit während der „Forschungspausen" im Musikwohnzimmer Klavier spielen zu können.
Dank auch an meine großartige Familie. Die emotionale Unterstützung in allen Lebenslagen, sowie unser Zusammenhalt in schwierigen Zeiten ist einfach unvergleichbar. Ich möchte mich daher ganz herzlich bei meiner Mutter Barbara und meinem Vater Hermann bedanken, wie sie mich stets in allem unterstützen; bei meiner Schwester Rebekka: Danke, dass es dich gibt!

Eidesstattliche Erklärung

Ich versichere eidesstattlich durch eigenhändige Unterschrift, dass ich die Arbeit selbstständig und ohne Benutzung anderer als der angegebenen Hilfsmittel angefertigt habe. Alle Stellen, die wörtlich oder sinngemäß aus Veröffentlichungen entnommen sind, habe ich als solche kenntlich gemacht.

Rostock, den 24. Juni 2019

Maximilian Felix Bigelmayr